Anticatalytic Strategies to Suppress Water Electrolysis in Aqueous Batteries

Yiming Sui, Xiulei Ji*

Department of Chemistry, Oregon State University, Corvallis, OR, 97331-4003 USA

*Corresponding authors: david.ji@oregonstate.edu

Abstract

Aqueous electrolytes are the protagonist to meet the surging demand for safe and low-cost storage batteries. Aqueous electrolytes facilitate more sustainable battery technologies due to the attributes of being nonflammable, environmentally benign, and of low cost. Yet, water's narrow electrochemical stability window remains the primal bottleneck for the development of high-energy aqueous batteries with long cycle life and infallible safety. Water's electrolysis leads to either hydrogen evolution reaction (HER) or oxygen evolution reaction (OER), which causes a series of dicey consequences, including poor Coulombic efficiency, short device longevity, and safety issues. These are often showstoppers of a new aqueous battery technology besides the low energy density. Prolific progress has been made in the understanding of HER and OER from both the catalysis and the battery fields. Unfortunately, there lacks a systematic review on these advances from a battery chemistry standpoint. This review provides in-depth discussions on the mechanisms of water electrolysis on electrodes, where we summarize the critical influencing factors applicable for a broad spectrum of aqueous battery systems. Recent progress and existing challenges on suppressing water electrolysis are discussed, and our perspectives on the future development of this field are provided.

Keywords: aqueous electrolytes, rechargeable batteries, water electrolysis, high voltage, overpotential

Contents

1. Introduction:	2
2. Thermodynamic Stability of Aqueous Electrolytes:	4
3. Overpotentials: Kinetically Controlled Water Electrolysis	7
3.1 Electrochemical Overpotential of HER:	9
3.1.1 Mechanisms of HER in Acid Electrolytes:	9
3.1.2 Mechanisms of HER in Alkaline/Neutral Electrolytes:	15
3.2 Electrochemical Overpotential of OER:	17
3.3 Ohmic and Concentration Overpotential:	23
4. Strategies of HER/OER Suppression in Aqueous Batteries:	24
4.1 Competition Mechanisms and Influencing Factors:	25
4.1.1 HER on Anode:	25
4.1.2 OER on Cathode:	27
4.2 HER/OER Suppression Strategies: A Thermodynamics Perspective	28
4.2.1 Strengthening O—H bonds in Water:	28
4.2.2 Decoupling Anolytes and Catholytes:	34
4.3 HER/OER Suppression Strategies: A Kinetics Perspective	35
4.3.1 Water Electrolysis Anticatalysts:	35
4.3.2 Reduction of Active Sites:	51
5. Challenges and Outlooks:	60
5.1 Considerations to tackle water's electrolysis:	60
5.1.1 About thermodynamic solutions:	60
5.1.2 About kinetic solutions:	61
5.1.3 Insights from Other Areas:	62
5.2 Characterization of Water Electrolysis on Electrodes:	63
5.3 Theoretical Simulation Methods:	66
5.4 Conclusions:	67
Poforoncos	60

1. Introduction:

The electrolyte plays a pivotal role in battery chemistries and imposes direct impacts on cell performance. Common electrolytes in rechargeable batteries can be classified into several groups: organic, aqueous, ionic liquid, and solid-state electrolytes. Among them, aqueous electrolytes embody many shining advantages. First, water (H_2O) is the most abundant solvent on this planet, and purification of water can be done at a low cost. In contrast, the manufacturing of ionic liquids or organic solvents often relies on petroleum products and consumes much energy. Second, unlike organic solvents, water itself is nontoxic, bringing no harm to the environment; its electrolysis products are hydrogen and oxygen gases, not poisonous. The non-flammable nature of water undergirds the overall safety of batteries. More importantly, water is a potent solvent for salts, featured by its high dielectric constant, large dipole moment, and excellent acceptor/donor numbers. Thus, aqueous electrolytes usually exhibit superior ionic conductivity, often much higher than that of organic electrolytes and solid–state electrolytes. $^{1-3}$

Unfortunately, aqueous electrolytes suffer a fatal disadvantage of the narrow voltage window of water, thermodynamically between 0-1.23 V vs. standard hydrogen electrode (SHE) at pH = 0, at 25 °C and 101.32 kPa, hereafter. At low potentials, water can be reduced, releasing H_2 gas in hydrogen evolution reaction (HER); at high potentials, water is oxidized, setting free O_2 gas in oxygen evolution reaction (OER). Differing from organic electrolytes, the solid–electrolyte interphase (SEI) does not readily form on the surface of electrodes in aqueous electrolytes. The continuous gas evolution of water during battery cycling or idling not only lowers the Coulombic efficiency (CE) but also causes serious safety concerns over explosion. Of note, the gas evolved by an aqueous battery is a mixture of hydrogen and oxygen, which would be flammable no matter whether the mixture is hydrogen lean or rich. Since most rechargeable batteries are closed systems, even a small amount of gas may cause mechanical disintegration of electrodes with increased internal impedance. In addition, water electrolysis can transform the chemical environment near the electrode surfaces, *e.g.*, the pH values, which profoundly affects the redox reactions of electrode materials.

To avoid gas evolution and promote cycling stability, the output voltages of aqueous batteries have to be kept low, which limits energy density and the usage of highly reducing and highly oxidizing electrodes. For instance, the HER and OER would theoretically take place at $^{\sim}$ 2.63 V and 3.86 V vs. Li † /Li, respectively, in neutral electrolytes (pH=7), while the redox potentials of most intensely-studied electrode materials for Li-ion batteries (LIBs), including anodes: Li metal at 0.0 V, graphite at 0.10 V, silicon at 0.30 V and cathodes: LiMn₂O₄ at 4.10 V, LiNi_{1/3}Mn_{1/3}Co_{1/3}O₂ at 4.20 V, and LiNi_{0.5}Mn_{1.5}O₄ at 4.60 V, are beyond the stability ranges of water. 1,5,6

The HER process takes place on the surface anode (or negative electrode) materials, where two electrons are transferred from the electrode to surface-adsorbed H_2O molecules or protons, where this multi-step reaction produces hydrogen gas; the OER process occurs on the surface cathode (or positive electrode) materials, during which the four-electron-transfer reactions covert H_2O molecule/OH⁻ ions adsorbed on the electrode's surface to oxygen gas. To design

feasible anticatalytic strategies, attention should be devoted to suppressing the elementary steps of HER and OER reactions.

A rational approach to inhibit water electrolysis is to expand the thermodynamic stability window of water. In aqueous electrolytes, the water molecules typically either solvate the cations and anions or roam as free ones (non-coordinated). The interactions between water molecules via hydrogen bonding or between ions and water molecules affect the strength of O–H covalent bond in the water molecules. Hence, it is critical to design the coordination environments of water molecules to improve their stability. For instance, the concentrated aqueous electrolytes, also known as water-in-salt electrolytes (WiSE) or aqueous deep eutectic solvents (DES), have recently been investigated for high-voltage aqueous batteries partially due to their solvation structures. Specifically, the number of free water molecules with higher reactivity is minimized in the concentrated electrolytes; thus, most water molecules are in the inner solvation shell of cations. Likewise, a similar stability-enhancing effect was observed in a so-called molecular crowding electrolyte, where the H₂O molecules are diluted by poly(ethylene glycol) (PEG). 11

From the perspective of kinetics, the anticatalytic strategies pertain to promoting the overpotentials for HER and OER reactions. The principles, albeit not well delineated, are the opposite of those for designing HER/OER electrocatalysts. Therefore, the electrode materials with inherently high overpotentials towards HER/OER can be defined as anticatalysts or negative catalysts. Specifically, the anticatalysts devise the uphill routes of water electrolysis with much higher activation energies than HER/OER electrocatalysts. For instance, lead–acid batteries exhibit a high voltage of 2 V in H₂SO₄ electrolytes because Pb metal anode and PbO₂ cathode exhibit high overpotentials towards HER and OER, respectively. Other electrode materials that have high HER/OER overpotentials have been sporadically identified during the recent renaissance of studies on aqueous batteries, such as hydroxylated Mn₅O₈. Furthermore, the anticatalysts could be introduced as a coating layer on electrodes, where the electrode active mass does not get to "see" the aqueous electrolyte. Also, electrolyte additives could efficaciously enhance the HER/OER overpotentials by blocking the active sites on electrodes; thus these substances are defined as electrolysis inhibitors.

This review aims to offer a comprehensive introduction of the anticatalytic strategies that either thermodynamically or kinetically inhibit water electrolysis on electrodes. We hope to provide a purview of considerations for mitigating HER/OER, where researchers in the field can form a systemic understanding of the current arts (Figure 1). Complementary to the published reviews on aqueous batteries^{2,15-20}, this review is expected to fill the gap of articulating the fundamentals of correlations between water electrolysis and energy storage in aqueous-battery systems.

This review has an emphasis on the thermodynamic stability of aqueous electrolytes and the kinetics-pertinent overpotentials of HER and OER, where there exists rich knowledge from fields of catalysis, batteries, and corrosion. We start with discussing the factors on the thermodynamic stability of aqueous electrolytes and related characterization methods; then we introduce

different types of kinetics-pertinent overpotentials, including electrochemical overpotential, Ohmic overpotential, and concentration overpotential, the specific mechanisms of OER/HER, and the relationships between overpotentials and electrolysis processes. We expect to scrutinize the strategies of catalysis on promoting HER/OER, where we hope to extrapolate the trend to the opposite direction to delineate the principles for enlarging HER/OER overpotentials. In the subsequent section, we will summarize the strategies to enhance the overpotentials to impede gas evolution in battery systems with theories and examples. We will address 1) the optimization of O–H bond strengths in water molecules, 2) decoupling the alkaline anolyte and the acidic catholyte, 3) the high selectivity of electrodes of promising anticatalysts, and 4) the reduction of surface-active sites of electrodes. Lastly, we provide our perspectives on pressing problems of the field and the promising routes for further development.

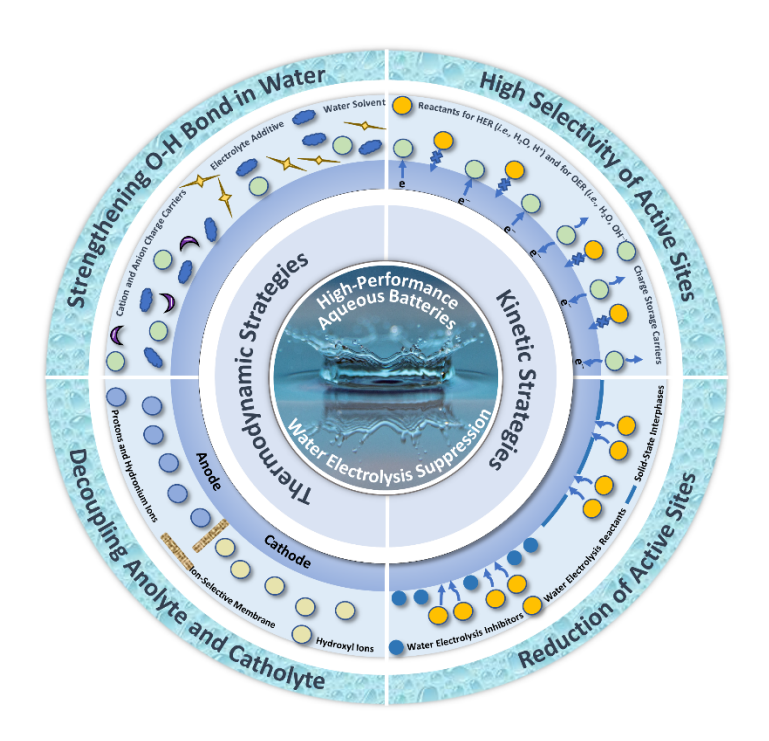


Figure 1. Schematic illustration of strategies towards widening the operating potential ranges of aqueous electrolytes by suppression of HER/OER processes over electrode surfaces (Inset water drop image is obtained from http://pexels.com/photo/water-droplet-in-shallow-photo-45229/).

2. Thermodynamic Stability of Aqueous Electrolytes:

The general reaction for water electrolysis is:

$$H_2O(l) \xrightarrow{electrical\ energy} H_2(g) + \frac{1}{2}O_2(g)$$
 Equation 1

The Gibbs free energy of the reaction can be calculated based on several assumptions: 1) H_2 and O_2 are ideal gases, 2) water is an incompressible fluid, and 3) the gas and liquid phases are thoroughly separated. Under standard conditions (25 °C and 101.32 kPa), the Gibbs free energy is approximately 237 kJ mol⁻¹; furthermore, the reversible electrolysis voltage is derived as ~1.23 V. In fact, the value is temperature and pressure dependent, with a lower splitting voltage at elevated temperatures and reduced pressures, *e.g.*, ~1.184 V at 80 °C and 101.32 kPa and ~1.295 V at 25 °C and 3 MPa. $^{22-24}$

Of note, the thermodynamic stability of water is mainly dependent on the strength of the O-H covalent bond in H_2O molecules, which is profoundly affected by the solvation structures in the aqueous electrolytes. Figure $2a_1$ depicts the hydration structure of a Li^+ ion in conventional dilute electrolytes. Therein, there are largely three environments of water molecules, in the primary solvation sheath, in the second solvation sheath, and as free water molecules. The chemical interactions, as influenced by the salt concentration and salt types, have strong impacts on the O-H bond strength in H_2O molecules, thus determining the thermodynamic stability of the electrolytes. The electrolytes.

As known, the hydrogen bond between water molecules reduces the strength of O-H bond in water molecules. Recent results suggest that by reducing the density of hydrogen bonds between water molecules with high salt concentrations, the thermodynamic stability of electrolytes was enhanced (Figure 2a₂).^{26,27} For example, a saturated NaClO₄ aqueous electrolyte (17 m) presents a wide electrochemical stability window of 3.2 V at the scan rate of 200 mV s⁻¹, measured with glassy carbon as the working electrode.²⁷ The trend of O-H bond strength as a function of salt concentration can be observed through some spectroscopic techniques, such as nuclear magnetic resonance (NMR)^{27,28}, Fourier-transform infrared spectroscopy (FTIR)^{28,29}, and Raman spectroscopy²⁹.

Specifically, the ¹H NMR results reveal that the concentrated LiTFSI (20 m) aqueous electrolyte presents a lower chemical shift (3.4 ppm vs. 4.7 ppm) and a narrower line width at the half height than that of pure water (Figure 2b₁).²⁸ The downshift originates from the shielding of protons from the water molecules due to an increase of their surrounding electronic density²⁸, while the narrower line-width is due to the weaker dipole-dipole coupling between neighboring spin in hydrogen bonds^{27,30}. In the same vein, the FTIR absorption spectra display a gradual blueshift of O-H bond stretch modes at ~3300 cm⁻¹ upon progressively increasing concentrations of LiTFSI in the electrolytes (Figure 2b₂). In Raman spectra, O-H bond stretch vibrations of pure water exhibit two peaks at ~3230 and 3420 cm⁻¹, representing two types of O-H environments: more H-bonded and less H-bonded, respectively (Figure 2b₃).²⁹ In contrast, the 30 m ZnCl₂ WiSE only exhibits the bluer peak at ~3454 cm⁻¹ in femtosecond stimulated Raman spectroscopy (FSRS), revealing the nearly eliminated H-bonding between free water molecules in the electrolyte. FSRS could offer significantly higher signal intensity than conventional Raman spectroscopy due to the ultrafast and wavelength-tunable laser pulses, thus more precisely reflecting the molecular vibrational motions and chemical bond variances.²⁹ Besides, salt concentrations in electrolytes also affect

the interfacial properties of anode materials in aqueous batteries, which is introduced in detail in Section 4.2.2.3.³¹

In addition to the concentration, the types of cations and anions are also critical to the electrochemical stability window of electrolytes, where the choices of ions influence the O-H bonding strength. For instance, alkaline metal cations (Li⁺, Na⁺, K⁺) are strongly solvated by water molecules in aqueous media; both the radii of the solvated complex ions and the Lewis acidity follow the trend of Li⁺ > Na⁺ > K⁺. 32,33 Bulky solvent–ion complexes may hinder the diffusion of the charges, thus inhibiting the water electrolysis. 16,32,34,35 However, the stronger Lewis acidity of Li⁺ results in poorer capability of proton shielding in water molecules than that of K⁺, which is suggested by the higher chemical shift of 1 m LiTFSI than that in 1 m KTFSI in 1 H NMR spectra (Figure 2c₁). 28

In concentrated electrolytes, anions also contribute to the electrochemical stability of electrolytes. As shown in Figure 2c₂, saturated LiNO₃ (~11 m) and LiCl (~18 m) electrolytes exhibit different bonding characteristics from that of concentrated LiTFSI electrolytes; specifically, the O-H bond stretch mode shows weak dependence on the salt concentration in LiNO₃ and LiCl electrolytes, which differs from the pattern of the LiTFSI electrolytes (Figure 2b₃).²⁸ The ¹H NMR further confirms that the lower chemical shifts in 20 m LiTFSI electrolytes (Figure 2b₁) when compared with the saturated LiNO₃ and LiCl electrolytes (Figure 2c₃), demonstrate a higher proton shielding performance of TFSI anion and stronger O-H bond strength of water molecules in TFSI anion-based WiSE.²⁸

The research on investigating the correlations between water's thermodynamic stability and the residing chemical environment start catching attention from the battery community. The research in this area will see further progress in the understanding of solvation structures of different electrolytes, particularly concentrated ones such as WiSE and DES.

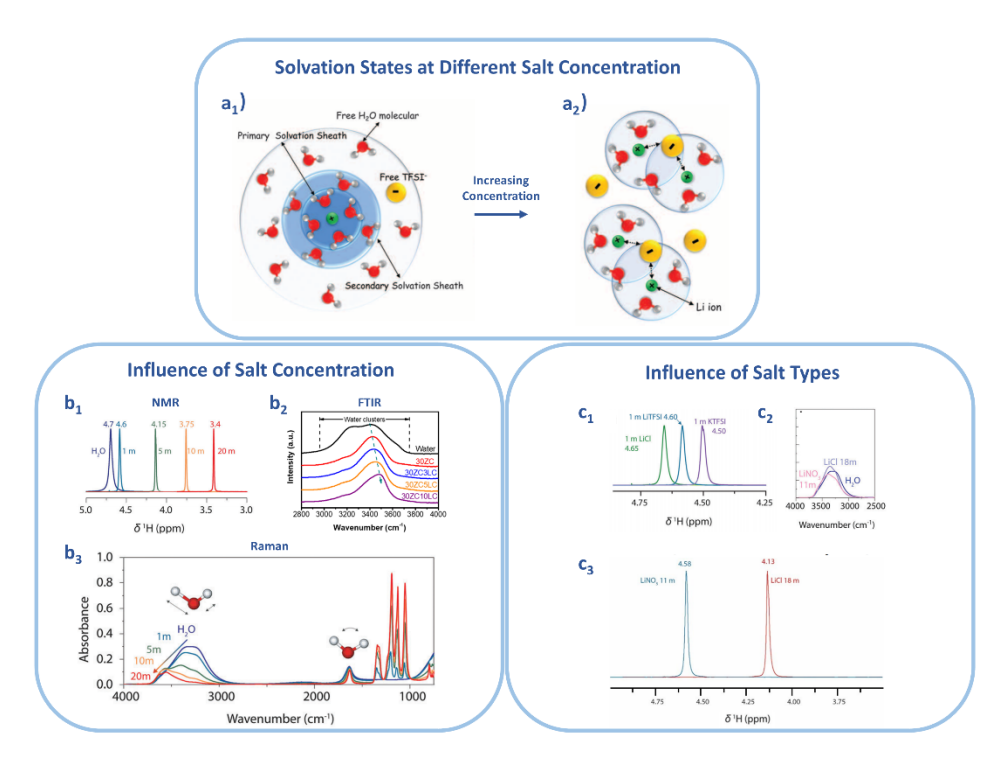


Figure 2. Schematic illustration of solvation structures of Li⁺ in a₁) salt-in-water electrolytes and a₂) water-in-salt electrolytes. Reproduced with permission from ref 10. Copyright 2015 AAAS. The influence of the salt concentration on the O-H bonding strength as suggested by b₁) ¹H NMR spectra in LiTFSI aqueous electrolytes of different concentrations (pure water: dark blue, 1 m: light blue, 5 m: green, 10 m: orange, and 20 m: red) (Reproduced with permission from ref 28. Copyright 2018 Royal Society of Chemistry.), b₂) Raman spectra in 30 m ZnCl₂, 30 m ZnCl₂+3 m LiCl, 30 m ZnCl₂+5 m LiCl, and 30 m ZnCl₂+10 m LiCl, which are abbreviated as 30 ZC, 30ZC3LC, 30ZC5LC, and 30ZC10LC, respectively (Reproduced with permission from ref 29. Copyright 2020 Wiley-VCH), and b₃) FTIR spectra in LiTFSI aqueous electrolytes of different concentrations (pure water: dark blue, 1 m: light blue, 5 m: green, 10 m: orange, and 20 m: red) (Reproduced with permission from ref 28. Copyright 2018 Royal Society of Chemistry.). Influence of cation types on the O-H bonding strength as characterized by c_1) ¹H NMR, and the influence of anion types on the O-H bonding strength as demonstrated by c₂) FTIR spectra of 11 m LiNO₃ (pink line) and 18 m LiCl (purple line) solutions, and c₃) ¹H NMR spectra of LiCl (green), LiTFSI (blue) and KTFSI (purple) with a concentration of 1 m. (Reproduced with permission from ref 28. Copyright 2018 Royal Society of Chemistry.)

3. Overpotentials: Kinetically Controlled Water Electrolysis

Water electrolysis involves two half-reactions: its reduction of HER at low potentials and its oxidation of OER at high potentials. The potentials of both reactions are the functions of the pH value, as displayed in the Pourbaix diagram under standard conditions (Figure 3). The blue line marks the critical potentials of the OER process with the Nernst expression shown in Equation 2,

above which OER can occur. The orange line represents the HER critical values below which HER can take place, where the Equation 3 shows its Nernst expression.²¹ Note that the difference between OER and HER thermodynamic equilibrium potentials is constant at ~1.23 V no matter the pH values.

$$E_0 = 1.228 V - 0.0591 VpH$$
 Equation 2

$$E_0 = 0.000 V - 0.0591 VpH$$
 Equation 3

Nevertheless, it usually requires a higher voltage than 1.23 V to split water in real situations. The difference between the actual voltage and 1.23 V comes from the addition of the kinetically controlled overpotentials (η) for both HER and OER. This means that it takes a higher potential to oxidize water for OER, and it needs a lower potential to reduce water for HER. There are three primary sources of overpotentials (see Equation 4), including 1) electrochemical overpotential (or called activation overpotential) (η_E), which relates to the reactant and product states in reactions, 2) Ohmic overpotential (η_R), which is affected by the electrode intrinsic electric impedance/resistance, and 3) concentration overpotential (η_c), which is a function of the concentration distribution near the electrode surface.³⁶ The specific factors that influence the three types of overpotentials and the associated mechanisms will be summarized and discussed in the following sections.

$$\eta_{overall} = \eta_E + \eta_R + \eta_C$$
 Equation 4

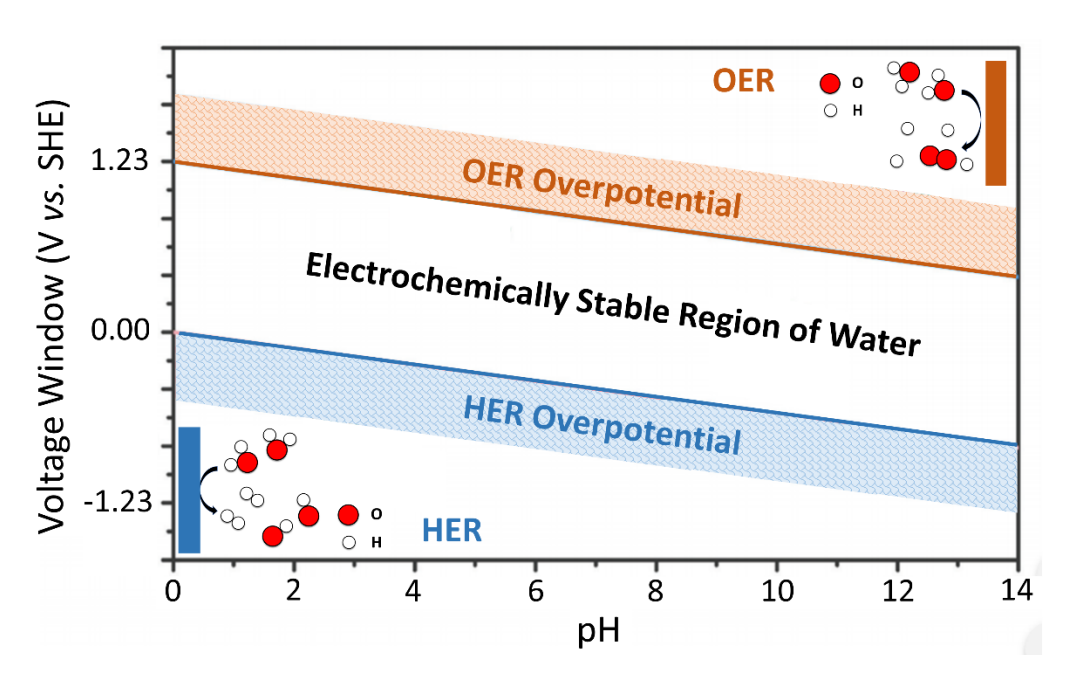


Figure 3. Pourbaix diagram of water with the y-axis of potentials (V vs. SHE) and the x-axis of pH values of aqueous electrolytes. The green line and orange line indicate the upper and lower

thermodynamically-stable-potentials as the function of pH values, where the green and red areas represent the overpotentials towards water oxidation (OER) and water reduction (HER), respectively.

It is accepted that overpotentials originate from kinetic constraints in individual steps of electrolysis. In brief, water's electrolysis processes involve the adsorption of water and ion species on the electrode surface, the formation of the intermediates via electron transfer, and finally, the release of oxygen/hydrogen gas.³⁷ Fundamental understanding of the sources of overpotentials is instrumental to kinetically mitigate HER/OER for the applications of high-voltage aqueous batteries. Herein, we summarize and discuss the influencing factors for the three types of overpotentials for HER and OER processes, respectively.

3.1 Electrochemical Overpotential of HER:

The electrochemical overpotential correlates to the intermediate formation energies in gas evolution reactions. As for HER in acid electrolytes, the binding energy between the intermediate of H* derived from H⁺ in the electrolytes and the electrode surface is the most important indicator for the overpotential. In the base/neutral electrolytes, HER is associated with relatively more complexed mechanisms due to the electrode surface's impacts on the H⁺ generation efficiency from water, which has a significant impact on the overpotential value. Herein, we will discuss the HER mechanisms and the influencing factors on the electrochemical overpotential in acid electrolytes and in base/neutral electrolytes, separately.

3.1.1 Mechanisms of HER in Acid Electrolytes:

Generally, HER follows a two–step reaction in acid electrolytes, during which two protons (H^+) or hydronium ions (H_3O^+) combine to form one H_2 (Figure 4). In the first step called the Volmer reaction, a proton receives one electron from the electrode, thus becoming adhered to the electrode surface as an intermediate hydrogen atom (H^+) (see Equation 5). 38,39

$$M + H^+ + e^- \rightarrow MH_{ads}$$
 Equation 5

Then there are two parallel routes for the hydrogen intermediate to form and desorb a H_2 molecule, depending on the intermediate coverage over the electrode surface. Specifically, when the H^* coverage on the surface is low, a H^* will more likely combine with a proton from the electrolyte and one more electron from the electrode to produce H_2 . The process is referred to as the Heyrovsky reaction (see Equation 6). If the H^* coverage is sufficiently high, two adjacent H^* will likely combine with each other to form a H_2 molecule, which is known as the Tafel reaction (see Equation 7).

$$MH_{ads} + H^+ + e^- \rightarrow M + H_2 \uparrow$$
 Equation 6
 $2MH_{ads} \rightarrow 2M + H_2 \uparrow$ Equation 7

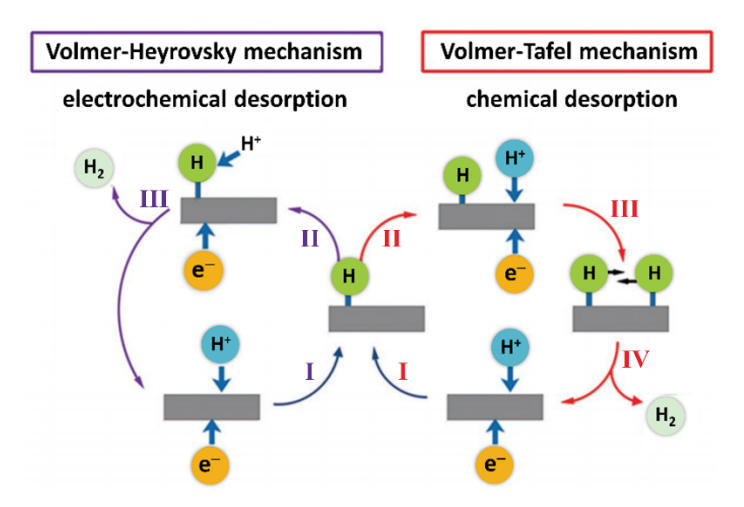


Figure 4. Two HER mechanisms in acid electrolytes, including the Volmer–Heyrovsky mechanism (left) and the Volmer–Tafel mechanism (right). Reproduced with permission from ref 39. Copyright 2014 Royal Society of Chemistry. The purple and red Roman numbers marked the reaction coordinates of the Volmer–Heyrovsky mechanism and the Volmer–Tafel mechanism, respectively.

Figure 5a and b depict the origins of HER's overpotentials in acids from the perspective of thermodynamics, where the Gibbs free energy of the reaction varies as a function of the applied potential (e.g., E₁, E₂, and E₃).⁴⁰ At the thermodynamic equilibrium potential (E₂), for a facile HER, the intermediates locate at the same free energy level with the reactants and the products (orange line). This fits the Sabatier principle that an ideal electrocatalyst should neither bind too strongly nor too weakly with reaction intermediates.⁴¹ Nevertheless, the Gibbs free energy of the intermediate in a real scenario (blue line) deviates from the ideal value, influenced by the binding energy between the electrode and the intermediates. Then it requires a lower potential, *i.e.*, a more reducing electrode to activate the HER process, where the difference between the real potential and the thermodynamic equilibrium potential is the reaction's overpotential.⁴⁰

Furthermore, the electrochemical overpotential is associated with the two steps of HER: the adsorption of the H* intermediate on the electrode and the desorption of H₂ gas, both of which relate to the intermediates' binding energy with the electrode surface. Therefore, the binding energy is the descriptor to evaluate the electrocatalytic or HER-inertness performances of the electrode materials. The electrochemical overpotential and the exchange current density (j₀) follow a volcano pattern as a function of the hydrogen binding energy (ΔG_{H*}) (Figure 5c) and the bond strength (E_{H*}) (Figure 5d), respectively. Specifically, the adsorption step limits the overall kinetics and determines the electrochemical overpotential at a weak binding strength ($\Delta G_{H*} > 0$), while the overpotential from the desorption step dominates at a lower binding energy ($\Delta G_{H*} < 0$). 34,40

Of note, this volcano trend is broadly applied to categorize and evaluate HER catalysts in acid electrolytes.⁴³ For instance, the Pt metal is considered the optimal HER catalyst in acid electrolytes due to the quintessential binding energy with hydrogen intermediates, while the Ag and Mo metal may help inhibit HER due to the relatively weak and strong bond, respectively. Of note, differing from the transition metals, sp main-group metals barely form M-H bonds, indicating their strong ability to suppress HER.⁴⁴

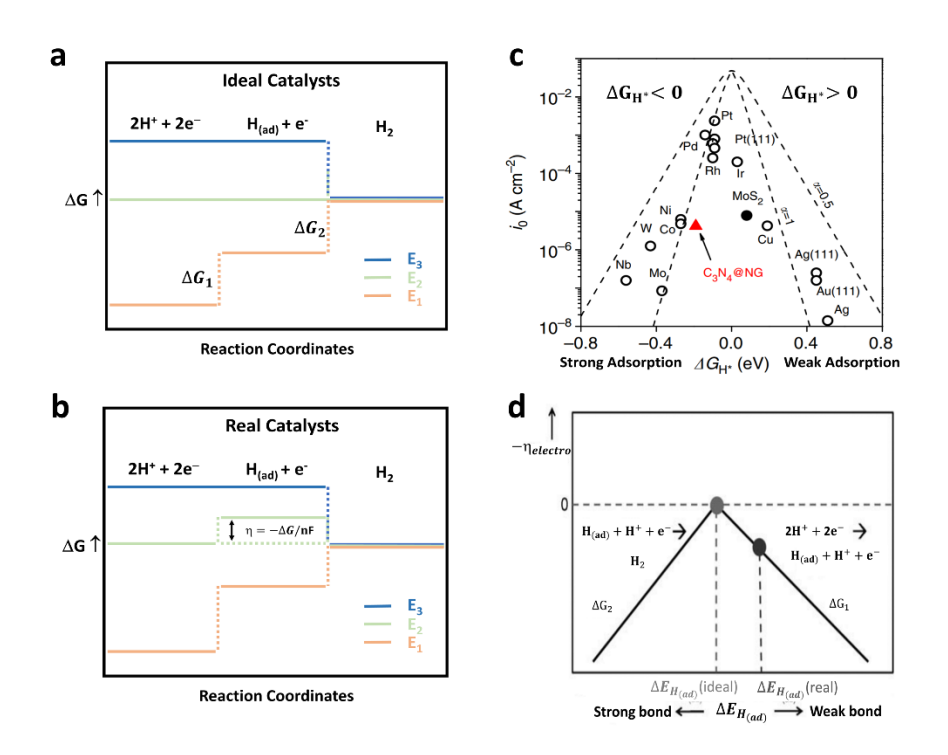


Figure 5. Schematic HER process under acidic conditions on a) ideal catalysts and b) real catalysts, where orange, green, and blue lines refer to Gibbs free energy variances at different electrode potentials (E₁>E₂>E₃), respectively; ΔG_1 and ΔG_2 denote the free reaction energies of the two HER elementary steps. At the thermodynamic equilibrium potential (E₂), the ideal reaction pathway is free of an overpotential; the real reaction pathway (blue line) has to overcome an overpotential (η) at the intermediate state. Reproduced with permission from ref 40. Copyright 2010 Wiley-VCH. Volcano plots for HER catalysts of different formats: c) The relationship between the reaction exchange current density (j_0) and adsorption energy of H* intermediates on the electrode surface (ΔG_{H^*}) with specific examples of metals, alloys, and non-metal compounds (Reproduced with permission from ref 43. Copyright 2014 Springer Nature.), and d) The relationship between the overall electrochemical overpotential of the HER process ($\eta_{electro}$) and the hydrogen chemisorption energy ($\Delta E_{H_{(ad)}}$): too strong or too weak bonds lead to high electrochemical overpotentials; ΔG_1 and ΔG_2 denote the free reaction energy of the two HER elementary reaction steps. Reproduced with permission from ref 40. Copyright 2010 Wiley-VCH.

Although the volcano plot is a powerful tool to categorize the catalysts, there are nuances about the metal surface properties and the resulted catalytic properties. The correlation between the electronic structures of catalysts and intermediate-adsorption energies (e.g., the d-band structures for elemental metals and their derivatives) has received much attention in the past decades. The formation of M-H* bonds creates fully-filled bonding molecular orbitals and partially filled anti-bonding molecular orbitals.³⁴ The disparity of the catalytic performance between metals largely lies in the different filling situations of the anti-bonding orbitals, where their increased filling destabilizes the metal-intermediate bonding, thus leading to the weaker bonding strength. 34,45 For example, Au displays the highest filling of the anti-bonding and the deepest location of the H 1s-d anti-bonding among four metals of Au, Ni, Pt, and Cu, as shown in Figure 6a.46 Hence, it exhibits the weakest M-H* bonding, followed by Cu. In comparison, Pt possesses the optimum bonding strength with hydrogen intermediates, which results from the moderate filling of H 1s-d anti-bonding. Ni has the strongest bonding strength due to the lowest filling of the anti–bonding orbitals and the highest location of H 1s–d anti–bonding. 46 Figure 6b depicts the hydrogen binding energies as a function of the d-band center (ε_d) values for some metals.^{34,47} Based on the trend, it could be derived that the Zn, Cd, and Hg would have weak M-H* bonding because of the deeper ε_d locations of the metals, which renders them promising HER anticatlysts.

Furthermore, the d–band structure or the d–band center referenced to the Fermi level could be changed by alloying/compositing with another metal, which offers the routes to design materials for catalysis or anticatalysts for batteries. Firstly, ε_d depends on the distances of atoms on the surface of metals (Figure 6c). For instance, when Pd atoms are deposited on another metal (e.g., Au) with a larger atomic distance, the tensile strength would lead to a narrower d band and a higher ε_d . Support as a wider d band and a lower ε_d would be induced by the compressive strength when Pt atoms are plated over a metal with a smaller atomic distance (e.g., Ru, Ir). In addition, the decorating metals may also have chemical bonding with the substrate metals. For instance, some transition metals, e.g., Ni, Co, Fe, Ag, Zn, could devote their electrons to the Pt/Pd substrate, thus causing the downshift of the d–band center of Pt/Pd relative to the Fermi energy.

Overall, designing promising metallic HER anticatalysts should firstly consider the d-band electronic structures of the materials, particularly ϵ_d , which directly determines the M–H* bonding strength and further the HER activity. An ideal HER anticatalyst should either exhibit a high ϵ_d location (strong M–H*) or a deep ϵ_d location (weak M–H*). Generally, the metals that have completely filled d-orbitals, including Zn, Cd, Hg, Bi, Pb, etc, display high HER overpotential because of their low ϵ_d locations. As for the HER inhibition on certain active metal materials (e.g., Ni, Co, Fe), alloying/compositing with other materials are feasible strategies, but whether the compressing/tensile stress or downshift/upshift of ϵ_d benefits cannot be clearly defined; instead it should depend on the specific properties of the protected materials.

For carbonaceous materials, their HER catalytic performances are also closely correlated to their electronic structures.⁵⁵ When H* intermediates bond with the electrode surface, the hybridized levels will split into the bonding states that locate below the Fermi energy and anti-bonding states that are situated above the Fermi energy (Figure 6d). Like transition metals, the latter states determine the bonding strength between the electrodes and the H* intermediates. 56 Specifically, a reduced occupation of the anti-bonding states results in stronger bonds between the adsorbates and the electrodes. Accordingly, a linear relationship can be constructed between the density of states (DOS) of active sites and the intermediate-electrode bonding strength for carbonaceous materials (Figure 6e). 56 To change the HER activity of carbonaceous materials, a common strategy is to introduce heteroatom dopants into the structure. Generally, the heteroatomic dopants (Figure 6f) could be categorized into two groups: electron donors that have lower electronegativity than carbon (e.g., S, P) and electron acceptors with higher electronegativity than carbon (e.g., N, O, F). 57 The addition of the former type of dopants would enrich electrons to the surrounding carbon atoms, while the later ones lead to the electron deficiency of the adjacent carbon atoms. ^{57,58} The electron transfer has direct impacts on the electronic structures of the materials, consequently affecting their HER activity.

To sum up, graphitic sp² carbon displays the best HER resistance, while other carboneceous materials with doping of heteroatoms (*i.e.*, S, N, O) exhibit higher HER activity. In fact, it is inevitable to introduce defects or functional groups during the production of common carbonaceous materials, thus promoting the hydrogen production rates. In this case, two general methods are practical to inhibit HER, including 1) removing/passivating the defects/functional groups through post-treaments, and 2) introducing other functional groups/doping to compensate for the side effects of the existed ones. Moer detailed discussion will be given in Section 4.2.1.1-(3).

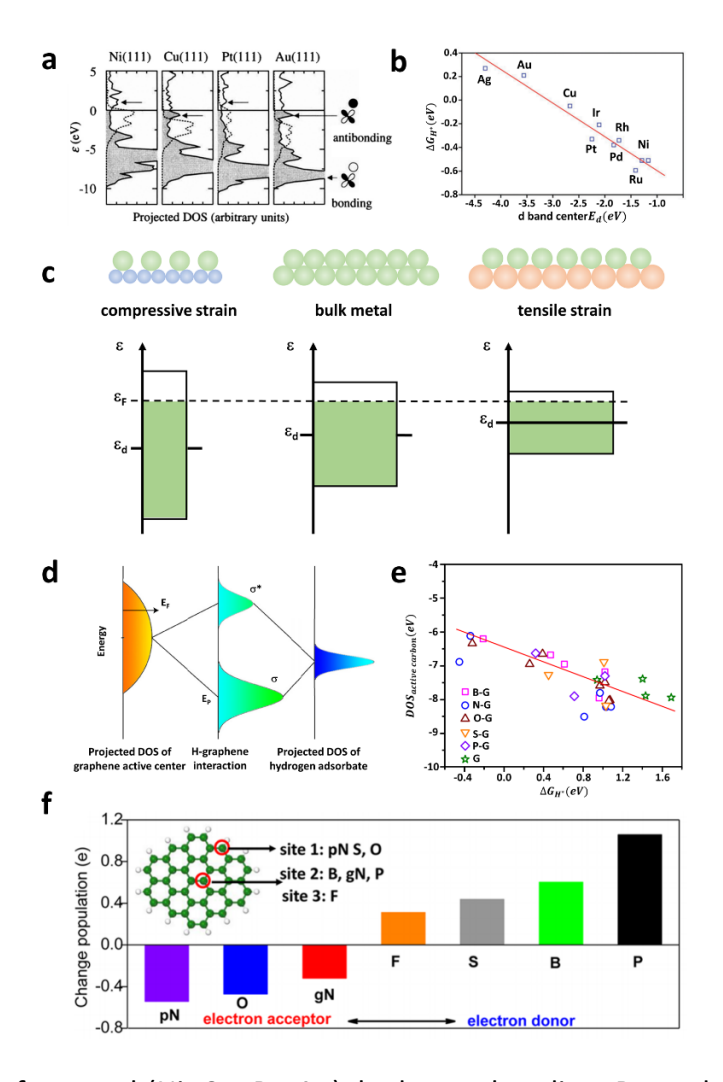


Figure 6. a) Scheme for metal (Ni, Cu, Pt, Au)–hydrogen bonding. Reproduced with permission from ref 46. Copyright 2020 Springer Nature. b) Linear relationship between metals' d–band center positions and the hydrogen–binding strength. Reproduced with permission from ref 34. Copyright 2015 Royal Society of Chemistry. c) Relationship between the surface atomic distance and the d–band center position. Reproduced with permission from ref 48. Copyright 2005 Wiley-VCH. d) Energy level diagram displaying orbital hybridization of active sites and hydrogen adsorbate, where E_F stands for the host's Fermi energy level, E_P represents the energy level of highest peak of active center's DOS with hydrogen adsorption, σ and σ* respectively denote the bonding and anti–bonding states. Reproduced with permission from ref 56. Copyright 2016 Springer Nature. e) Relationship between the adsorption energy of H* intermediates on the electrode surface (ΔG_{H^*}) and the highest peak position of active carbon's DOS. Reproduced with permission from ref 56. Copyright 2016 Springer Nature. f) NBO population analysis of several heteroatoms in a graphene matrix, including pyridinic N (pN), graphitic N (gN), O, F, S, B, and P. Reproduced with permission from ref 57. Copyright 2014 American Chemical Society.

3.1.2 Mechanisms of HER in Alkaline/Neutral Electrolytes:

In alkaline/neutral electrolytes, the HER also undergoes the formation of H* first, which proceeds with two possible routes (the Heyrovsky reaction or the Tafel reaction) to release hydrogen gas as it does in the acidic electrolytes. Nevertheless, compared to the behavior in acid electrolytes, the HER electrocatalysts in alkaline electrolytes typically deliver the activity two orders of magnitude lower (reflected by the exchange current density j_0) along with much higher overpotentials.^{53,59} The foremost reason is the difference in the initial Volmer process, where in the acidic electrolytes, free H⁺ or H₃O⁺ ions are directly involved in forming the intermediates, whereas H₂O is the reactant in alkaline/neutral electrolytes and has to dissociate and be reduced before H^{*} intermediate is formed (Equation 8).

$$M + H_2O + e^- \rightarrow MH_{ad} + OH^-$$
 Equation 8

The additional water dissociation step brings an extra energy barrier (0.76 eV) in bulk water, calculated from the first-principles molecular dynamics. ^{60,47} In addition to the dissociation barrier, the binding energy of water to the electrode surface is often inherently inferior to that of hydronium ions, which further enhances the barrier on the generation of M-H* intermediates in the alkaline electrolytes. Besides, as distinct from the acid electrolytes, the adsorption of oxygen-based intermediates (e.g., HO*) may poison the HER kinetics by blocking the active sites and altering the adsorption energy of H* intermediates over the catalyst. ⁴⁷ This phenomenon increases the reaction overpotential and hampers the HER activity in alkaline electrolytes. It was further elucidated that the charge transfer takes place more swiftly through the electrical double layer on the electrode's surface in acid electrolytes than in alkaline counterparts due to the more facile reconstruction of the interfacial water network, which will be discussed in detail below. ⁶¹

Overall, the mechanism of HER in alkaline electrolytes is more complexed than that in acid electrolytes, where more indicators should be considered in evaluating the HER under the alkaline conditions, including the hydrogen bonding energy, hydroxyl adsorption energy, water dissociation kinetics, and the surface double layer structure. For the binding energy with hydrogen, basic routes and mechanisms are not influenced by the pH value and have been introduced in Section 3.1.1; therefore, it is not discussed in detail here. And the exchange current density also follows a volcano–shaped pattern with the electrode–hydrogen bonding strength (Figure 7a). 62,63 It should be noted that volcano plots may not work for some metals on the right side (weak leg of binding) of the hill under alkaline conditions such as Mo, Ti, and W, since their surface will be passivated by *in situ* formed oxide layers. 62 When omitting these metals, an approximately linear correlation could be derived. 64

Water dissociation is considered one major barrier for the suppressed HER in alkaline electrolytes; therefore, materials' capability on dissociating water becomes one key indicator to evaluate their HER performance besides the binding energy with intermediates. ^{47,65} For instance, Ru with higher water dissociation capability (less positive water dissociation free energy (ΔG_B)) results in more severe HER than Pt in alkaline electrolytes despite of its stronger H* adsorption (more negative

H* adsorption free energy (ΔG_{H^*})) (Figure 7b). ⁶⁵ The water dissociation kinetics relates to the energy difference (ΔE) between the reactants (E(H₂O)) and products (E(H*) and E(HO*)), as shown in Equation 9. According to the Brønsted–Evans–Polanyi (BEP) principle, $E_a = E_0 + \alpha \Delta H$ ($0 \le \alpha \le 1$), the activation energy of a process is linearly related to the enthalpy of the step. Correspondingly, strong adsorption of H* and HO* would lower the activation energy of the water dissociation. ^{66,67} Therefore, a high water dissociation barrier to inhibit HER requires a weak adsorption of H*/OH* intermediates on the electrode surface. The water dissociation capability of several metals is calculated, as displayed in Figure 7c, where Ru should exhibit the highest activation energy barrier for water's dissociation. ⁶⁸ On the other hand, adsorption of HO* poisons the surface active sites and helps reduce the HER activity. ⁴⁷ The binding energies between metal surfaces and H*, OH*, H₂O, and O* are summarized in Figure 7d, and Ru seems to be the most poisoned among these HER catalysts in alkaline electrolytes due to the overly strong binding energy towards oxygen–contained intermediates. ⁶⁸

The double layer structure of electrode materials is typically featured with the potential of zero free charge (pzfc), which determines the interfacial electrical field and the solvation environment. Specifically, when the applied potential is much lower or much higher than the pzfc, the electrode's surface will be charged, resulting in large interfacial electric fields. Consequently, the assembly of water molecules is more rigid, and it needs to overcome a higher energy barrier for water molecules to reorganize themselves in the double layer at these potentials, which hinders the transfer of charges (H⁺ in acid electrolytes and OH⁻ in alkaline electrolytes). Therefore, the double layer is affected by both the pH value of electrolytes and electrode materials. The pzfc of Pt (111), for example, is closer to the potential of H* adsorption under acid conditions than in alkaline electrolytes, which allows the facile reorganization of water and rapid diffusion of charges, via the Grotthuss mechanism, thus benefiting the overall HER activity. At the same time, the deposited Ni(OH)₂ on the Pt (111) electrode surface can also move the pzfc closer to the potential of H* adsorption, thus accelerating the charge transfer through the interfacial double layer.⁶¹

$$\Delta E = E(H_2O) - E(H^*) - E(OH^*)$$
 Equation 9

To sum up, the mechanisms that lead to electrochemical overpotentials in HER can serve as useful references to design high–HER–overpotential anodes in high–voltage aqueous batteries. Remarkable progress has been made in the catalysis field about how to mitigate the electrochemical overpotential; yet the opposite direction of promoting this potential remains to be carefully explored. To date, most of the materials studied about HER's overpotential are still the catalysts such as transition metals. To inhibit HER in aqueous batteries, efforts should be devoted to exploring anode materials that have their redox reactions below 0 V vs. SHE.

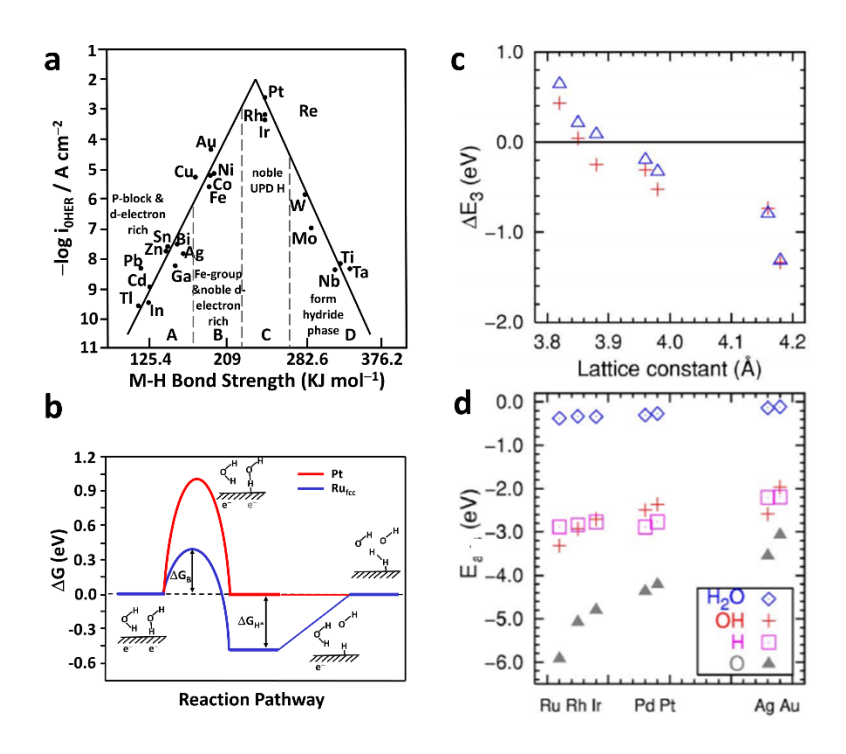


Figure 7. a) Volcano plots for some metal HER catalysts. Reproduced with permission from ref 63. Copyright 2000 Elsevier. b) The Gibbs free energy diagram of the HER process in alkaline media in the sequence of reactant initial state, water dissociation state, intermediate state, and product state. Reproduced with permission from ref 65. Copyright 2016 American Chemical Society. c) The water dissociation capability of various metal catalysts, where the y-axis is defined as the energy balance for water dissociation (ΔE), which is derived as the energy difference between the reactants ($E(H_2O)$) and products ($E(H^*)$) and $E(HO^*)$) (Equation 8), and d) The adsorption energies of reactant (H_2O) and reaction intermediates (H^* , HO^* , and O^*) over various metal catalysts. Reproduced with permission from ref 68. Copyright 2006 American Physical Society.

3.2 Electrochemical Overpotential of OER:

In water splitting⁶⁹⁻⁷¹, OER is usually the rate-determining process, which exhibits a higher overpotential than that of HER due to two primary factors: 1) the four-electron reaction to produce oxygen gas in comparison to the two-electron reaction to generate hydrogen gas, and 2) the intrinsic sluggish kinetics to break the O-H covalent bonds in water molecules and the construction of O-O bond in oxygen gas.⁷²

The specific mechanisms of the electrocatalytic OER process have minor differences in alkaline solutions and in acid/neutral solutions. The OER in alkaline electrolytes constantly consumes OH^- and releases water, and conversely, in acid/neutral electrolytes, H_2O is consumed as reactants, and the products are protons. Besides, the OER overpotential does not closely correlate with the electrolyte pH values, being different from HER; hence, the OER mechanisms in both acidic and alkaline electrolytes are discussed together here, as shown in Figure 8a and Table 1. 37,73

Specifically, Equation 10 (Equation 16) and Equations 11–15 (Equation 17–21) demonstrate the overall and elementary step reactions for OER in alkaline electrolytes (acid/neutral electrolytes), where the E stands for electrodes.

Table 1

Alkaline Electrolytes		Acid and Neutral Electrolytes	
$40H^- \rightarrow 2H_2O + 4e^- + O_2 \uparrow$	Equation 10	$2H_2O \to 4H^+ + 4e^- + O_2 \uparrow$	Equation 16
$OH^- \rightarrow E - HO^* + e^-$	Equation 11	$H_2O \rightarrow HO^* + H^+ + e^-$	Equation 17
$HO^* + OH^- \to O^* + H_2O + e^-$	Equation 12	$OH \rightarrow O^* + H^+ + e^-$	Equation 18
$20^* \rightarrow \mathcal{O}_2 \uparrow$	Equation 13	$20^* \rightarrow O_2 \uparrow$	Equation 19
or $0^* + 0H^- \to H00^* + e^-$	Equation 14	or $0^* + H_2 0 \to H 0 0^* + H^+ + e^-$	Equation 20
$HOO^* + OH^- \rightarrow H_2O + O_2 \uparrow + e^-$	Equation 15	$HOO^* \rightarrow O_2 \uparrow + H^+ + e^-$	Equation 21

The oxygen–production process involves more intermediates (e.g., HO*, O*, and HOO*) than the HER process; thus, the theoretical analysis on OER should take more factors into consideration. From the perspective of thermodynamics, the change of Gibbs free energy in the reactions strongly influences the reaction activity. Ideally, the Gibbs free energy change (ΔG) for each reaction step is an equal value of 1.23 eV. When setting the initial reactant water as the reference of energy point (0 eV), the Gibbs free energies of the intermediates HO*, O*, and HOO* and the reaction product of oxygen gas are ideally the 1.23 eV, 2.46 eV, 3.69 eV, and 4.92 eV separately (Figure 8b). In a practical situation, the Gibbs free energy for each step deviates from the theoretical value as strongly influenced by the binding energy between the corresponding intermediate and the electrode surface; accordingly, the step with the largest Gibbs energy deviation is defined as the rate–determining step and contributes the most to the overall OER electrochemical overpotential. 40,72

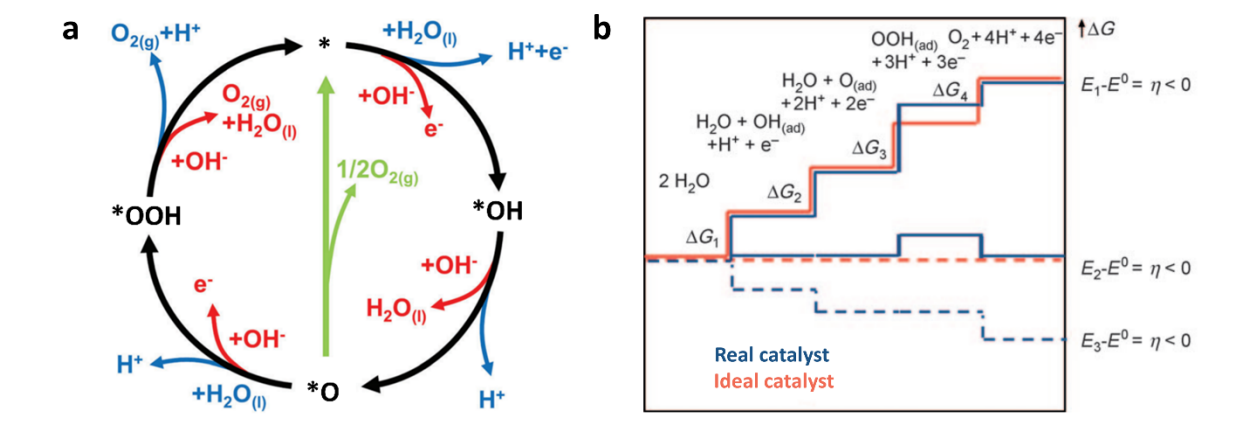


Figure 8. a) Schematic illustration of OER mechanisms in acid/neutral electrolytes (blue lines) and in alkaline electrolytes (red lines), where the * represents the electrode surface's active site. Reproduced with permission from ref 37. Copyright 2017 Royal Society of Chemistry. b) Gibbs free energy transitions from water to intermediates and to oxygen gas in the OER process, in which the blue lines and red lines stand for the energetics of a catalyst in real and ideal situation, respectively, at three different applied potential (E₁, E₂, and E₃). Reproduced with permission from ref 72. Copyright 2019 Royal Society of Chemistry.

Despite the various intermediates, the key parameter of the OER process is the bonding between the oxygen atom and the electrode surface. The intermediates bind with the electrode surface typically via the oxygen atom, where each intermediate contains at least one oxygen. A high binding energy of electrodes towards oxygen atom increases the barrier for the HOO* formation; on the other hand, the HO* intermediates cannot be formed readily at a low binding energy, which means the OER process would not be even initiated. Notably, altogether, two different routes are susceptible to form oxygen molecules from O* intermediates, where one is via HOO* in the following step, and the other is via the direct combination of the O* intermediates. The first mechanism is so far supported by only a few materials (e.g., β -MnO₂), which may relate to the similar formation energies for HOO* and HO* intermediates on the materials. The latter mechanism can explain the behaviors of most OER electrocatalysts.

Of note, the Gibbs energy difference between HO* and HOO* intermediates is a constant value of 3.2 eV for metal and oxide electrocatalysts, no matter of the external conditions (Figure 9a). 36,74,76 On the right slope of the volcano plots, when the bond strength between the catalysts and oxygen is weak, the oxidation of the HO* intermediate is the rate-determining step. On the left side of the volcano plots, the bond to O* is strong, and consequently the formation of HOO* intermediates becomes the limiting step for the OER process. Thus, value of $(\Delta G_{O^*} - \Delta G_{HO^*})$ is a descriptor to evaluate the electrocatalysts in the volcano plots (Figure 9b). And the approximation of the electrochemical overpotential for OER would be derived based on the Equation 22, where E^0 is the thermodynamically calculated OER occurrence potential.

$$\eta_E = \frac{\max[\Delta G_2, 3.2 - \Delta G_2]}{e} - E^0$$
 Equation 22

Therefore, those materials with $(\Delta G_{O^*} - \Delta G_{OH^*})$ half of 3.2 V are capable OER catalyst with minimal overpotentials. On the other hand, battery chemists should look for materials at the foot of the volcano plots, where either the formation of O* or the formation of HOO* constitutes a high overpotential.

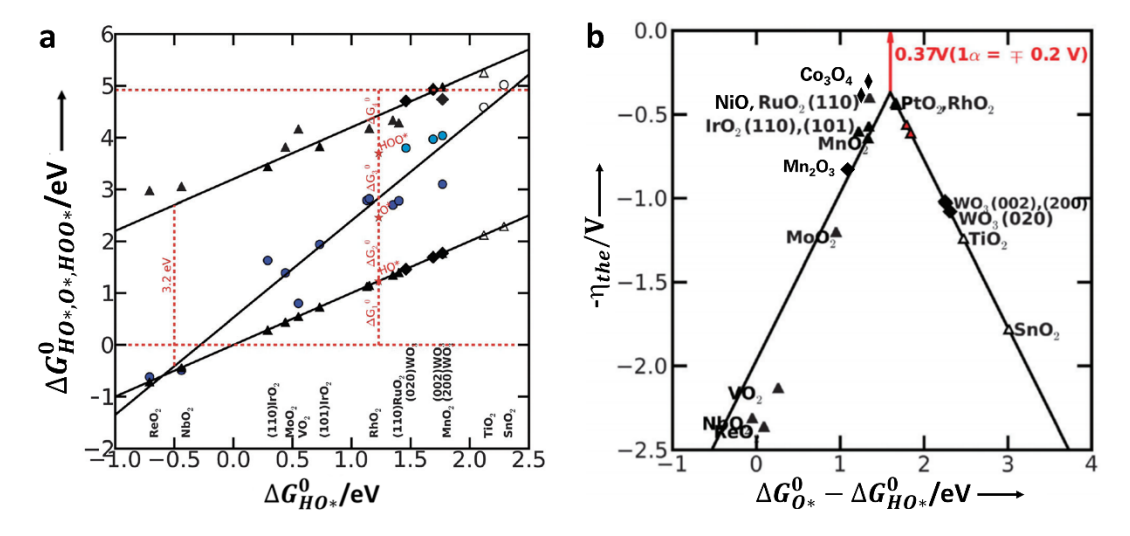


Figure 9. a) HOO*, O*, HO* binding free energies on metal oxides, where the filled symbols stand for the adsorption energies on the electrode with a high coverage of oxygen, the hollow symbols denote adsorption energies on the clean electrode surfaces with no nearest neighbors, the triangles are for HOO* and HO* species, and the circles are for O* species. It could be observed that the $\Delta G_{HOO*} - \Delta G_{HO*}$ exhibits a constant value of 3.2eV.⁷⁴ b) Volcano plots of OER catalysts with the Y-axis of electrochemical overpotential and X-axis of the Gibbs free energy change ($\Delta G_{O*} - \Delta G_{HO*}$). Reproduced with permission from ref 74. Copyright 2012 Royal Society of Chemistry.

The adsorption energy towards the intermediates is correlated to an electrode's electronic structure. For metals, the d–band theory discussed in the HER section is applicable for the OER scenarios. Note that metal materials themselves are typically not employed as the cathode in batteries unless in halide batteries that use halide ions as charge carriers; however, metals are still relevant to serve as current collectors in aqueous batteries. In brief, the state of partly filled anti–bonding orbitals formed by the oxygen–metal bonding, which is influenced by the metal d–band position (or ϵ_d), is correlated to the metal–adsorbate interaction strength (Figure 10a). 34,78,79

For metal oxides, particularly the 3d–transition-metal ones, it is reported that the filling of the metal's 3d e_g and t_{2g} orbitals correlates with the adsorption energy of oxygen intermediates, as supported by the DFT simulation (Figure 10b). ^{80,81} The interactions between the metal 3d–band states and the O 2p band produce the bonding and anti–bonding bands. The bonding strength depends on the extent of band filling (Figure 10c). ^{34,82,83} Specifically, the strongest bond is associated with fully–filled bonding states and an empty O anti–bonding states. ⁸¹ Furthermore, it was exemplified by some double perovskites that the OER catalysis activities would be enhanced when the O p–band center is close to the Fermi energy of the metal oxide. ⁸² To mitigate OER, it would therefore be necessary to identify electrodes of metal oxides with the O p–band center far from the oxides' Fermi level, which will also enhance the structural stability. Of note, the d–band energy could also be affected by the metal's valence states, the dopants, the

coordination environment of metals, which offers opportunities to reduce electrode's OER activity for high-voltage aqueous batteries. 75,84-88

OER can be a challenge for carbonaceous positive electrodes in electrical double-layer capacitors (EDLCs), also known as supercapacitors⁸⁹, and the cathode in aqueous dual ion batteries (DIBs)⁹⁰. the analysis of OER for carbon-based electrode materials is via the "natural bond order (NBO)" method, similar to the "d-band" theories for transition metal catalysts.^{91,92} And the difference between the highest energy of the valence band and lowest energy in the conduction band, *i.e.*, E_{diff} , represents the indicator to evaluate the binding energy with oxygen-intermediates. After hybridizing with orbitals of the oxygen-intermediates, a fully filled bonding (v- σ) and a partially filled anti-bonding (v- σ *) will be formed at lower and higher energy levels, respectively. A higher filling of antibonding weakens the bond between the intermediates and carbonaceous surface while a lower filling of antibonding enhances the bonding strength (Figure 10d).⁹¹

Besides the intrinsic electronic properties of the carbon materials, their surface hydrophobicity also has impacts on the HO* binding energy. Decorating OER catalyst's surface with hydrophobic polymers (e.g., polytetrafluoroethylene (PTFE)) could significantly improve the selectivity of hydrogen peroxide production relative to OER. The hydrophobic surface, together with the trapped O_2 gas bubbles near electrodes, interrupt the formation of the H-bonds between HO* intermediates on electrodes and O_2 0 molecules in electrolytes, which destabilizes the absorption of HO* on the electrode. When the binding energy of HO* is at an intermediate level, OER can be controlled to be 2-electron oxidation in forming O_2 1.

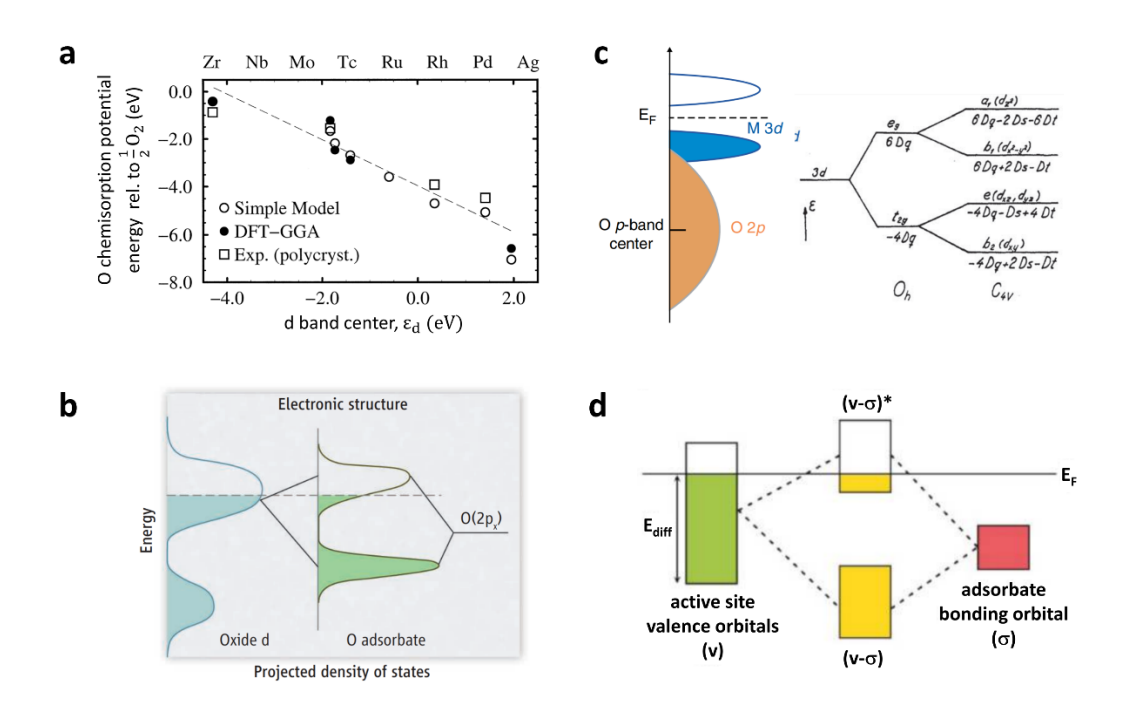


Figure 10. a) Relationship between the d-band center position in the electronic structure and the oxygen chemisorption energy for metal catalysts. Reproduced with permission from ref 79. Copyright 2000 Elsevier. b) Schematic illustration of orbital-filling states in transition metal oxide catalysts before and after binding with oxygen adsorbents. Reproduced with permission from ref 81. Copyright 2011 AAAS. c) Schematic illustration of orbitals splitting in transition metal oxide catalysts after forming the oxide—oxygen bonding. Reproduced with permission from ref 34. Copyright 2015 Royal Society of Chemistry. d) Schematic illustration of the graphene—oxygen bonding process. Reproduced with permission from ref 91. Copyright 2014 American Chemical Society.

In addition to the material's intrinsic properties, the working conditions e.g., pH and potential, may also influence the OER activity through changing their surface compositions.³⁴ The Pourbaix diagram of manganese oxides (MnO_x) reveals the transition of stable phases at various applied potentials and the pH of surrounding environment (Figure 11).⁷⁵ Specifically, the bulk of MnO_x would undergo the phase transition from Mn₂O₃ to MnO₂ (110) between 1.01 V and 1.21 V vs. RHE and the dominant adsorbate on its surface is HO*. When the applied potential increases above 1.21 V, the surface would be further oxidized while the surface adsorbate is gradually replaced by O*. Hence, at the OER theoretical onset potential, the dominant composition of MnO_x surface is O* covered MnO₂, which is irrelevant to the initial composition of the material. Similarly, metals such as Ru also tend to be corroded at high anodic potential and catalyze OER through the surface oxide film.⁹⁴

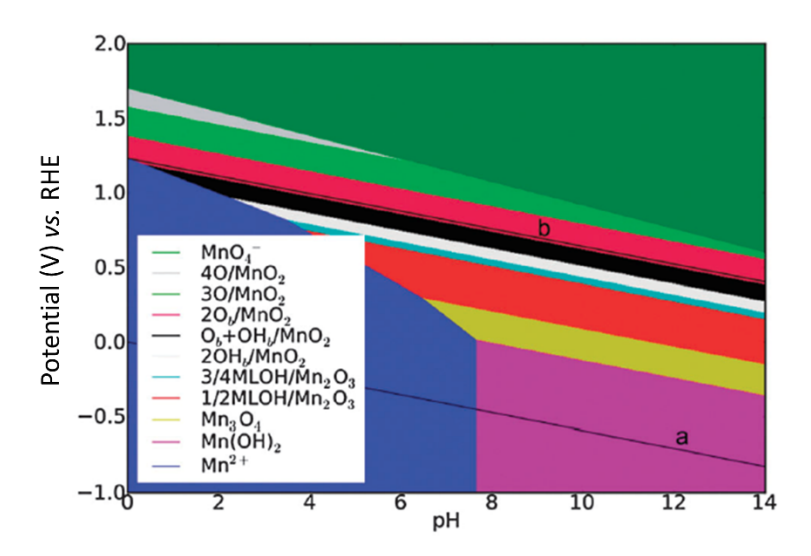


Figure 11. Surface Pourbaix diagram of MnO_x electrodes, where lines a and b stand for the RHE line and the O_2/H_2O equilibrium line, respectively. Reproduced with permission from ref 75. Copyright 2012 Royal Society of Chemistry.

Overall, the fundamental issues of OER—the reaction mechanism, the origins of electrochemical overpotentials, the criteria to evaluate and predict cathodes' performances—are the critical knowledge base and the references to guide the design for high-performance cathodes in aqueous batteries. Like the HER, the fundamental correlation between OER-catalytic performance and the electronic structure of electrodes is still lacking, which remains the bottleneck for the field.

3.3 Ohmic and Concentration Overpotential:

The electrochemical overpotential involves the finesse of mechanisms for water electrolysis. By contrast, the origins of Ohmic and concentration overpotentials are more straightforward; these overpotentials are influenced by the physical properties of electrodes, *e.g.*, surface electrical conductivity, morphology, surface area, and electrolytes, *e.g.*, pH, salt concentration, and ionic conductivity. For the Ohmic overpotential, it derives from the internal impedance of the cells (*e.g.*, electrodes, electrolytes). Among the factors, the electrode materials' electrical conductivity (σ) is strongly correlated to materials' band structure, *e.g.*, the width of band gap.

The concentration overpotential originates from the depletion of reactants relative to the product near the electrode's active surface. More specifically, the electrode active surface refers to the sites that exhibit electrocatalytic ability, including the exposed active sites and hidden active sites. The supply shortage of the reactants to the surface limits the reaction kinetics. Hence, the primary factor on influencing the concentration overpotential is the amount of exposed active sites on surface, which involves factors such as electrode surface area and microstructure. A large concentration polarization on water electrolysis will be produced if the active sites are hidden. For example, increasing the preparation temperatures has been proven a feasible strategy to reduce metal oxide's OER activity. A critical factor is the enlarged crystallite size followed by the shrinkage of surface area, thus reducing the active sites on electrodes.

The other influencing factors relate to the electrolyte nature. H⁺ and OH⁻ are the preferred reactants for HER and OER, respectively. In particular, HER is very sensitive to the pH of electrolytes and suffers from distinctly high overpotentials in alkaline electrolytes due to several factors (see Section 3.1.2 for details), among which poisoning of active sites by HO* intermediates should be categorized to the concentration overpotential.

An exception to the trend of the HER activity as a function of the pH values was reported for a Pt/C electrode, which exhibits a lower activity in the 0.01 M KOH electrolyte than that in the 1 M KOH electrolyte. ⁹⁸ Another exception is that neutral electrolytes are more advantageous in inhibiting HER and OER. In neutral electrolytes, the HER and OER follow the Equation 8 and Equation 16 to occur on anode and cathode surfaces, respectively The locally generated OH⁻ and H⁺ alter the local pH values dramatically near the electrodes, which shifts the local gas evolution potentials according to the Pourbaix diagram (Figure 3). ^{2,99} Another minor factor is that neutral electrolytes

possess higher resistance, resulting in greater Ohmic overpotentials. 100,101 Consequently, HER and OER typically exhibit high overpotentials in neutral media, e.g., >460 mV at 10 mA cm⁻² for OER and >200 mV at 10 mA cm⁻² for HER; this phenomenon bestows neutral aqueous electrolytes wide operation potential windows. Therefore, when evaluating the electrochemical stability of electrolytes, the local pH near the electrodes is a more reliable indicator over that of bulk electrolyte.

4. Strategies of HER/OER Suppression in Aqueous Batteries:

Water electrolysis can take place during the charging, discharging, and idling processes of batteries. In practical applications, an idling battery can be at any of its state of charge (SOC). If this battery is deeply discharged, the potential of its cathode should be below the OER onset potential; therefore, OER is not a concern for a discharged battery. However, on the anode side, if there exists an excess of active mass, *e.g.*, Zn metal, the anode can still react with the aqueous electrolytes in reduction, resulting in HER, which resembles the electroless metal corrosion under aqueous or humid environments. On the other hand, if a battery starts idling after charging, where it contains a significant amount of energy stored and the cathode and anode are at their oxidized and reduced format, respectively. In this case, both HER and OER may take place. During the idling of batteries, either HER or OER is a primary contributor to the battery self-discharge. Regarding water's electrolysis, charging is more complexed than that in idling state cells, where both electrodes involve two competing processes: hosting charges for energy storage and serving as the conducting surface for water electrolysis.

The electrochemical stability of aqueous electrolytes is co-influenced by the thermodynamic stability of electrolytes and the kinetic overpotentials of the water electrolysis processes. The thermodynamic stability is the intrinsic property of the water solvents, which is independent of the cell states. As mentioned in Section 2, it is closely related to the O–H bond strength inside the water molecules and the pH of electrolytes. In order to enlarge the operating voltage of aqueous electrolytes, one strategy is to promote the thermodynamic stability of water; another is to enhance the HER and OER overpotentials for anodes and cathodes, respectively.

Water electrolysis is a surface–controlled reaction, whereas the charge storage involves not only a surface-controlled process (i.e., the electrical double layer capacitance) but also processes where ions diffuse beneath the surface of solids. However, on the electrode surface, the charge storage process competes with the parasitic HER/OER for the surface–active sites to complete the charge transfer, where the charge-storage reactions may affect the overpotentials of water electrolysis.

Accordingly, strategies have been developed to widen the electrolytes' electrochemical stability window by suppressing the water-splitting reactions for high-voltage aqueous batteries. This section will firstly introduce the mechanisms and influencing factors on the competition between water splitting and charge storage process at both charging and idling states of cells. The

strategies to suppress water electrolysis from both perspectives of thermodynamics and kinetics will be summarized and discussed in combination with the associated mechanisms and the recent advances in the fields.

4.1 Competition Mechanisms and Influencing Factors:

4.1.1 HER on Anode:

In aqueous batteries, the HER process can occur on the anode surface during the charging process. Generally, the relationship of potentials (Equation 23) should be met to be HER free, where the $E_{negative}$ stands for the thermodynamic oxidation potential of the anode, the $\eta_{negative}$ is the overpotential of anode's oxidation reaction, the E_{HER} represents the ideal HER potential at the pH value, and the η_{HER} is the overpotential of HER reaction.

$$E_{negative} - \eta_{negative} > E_{HER} - \eta_{HER}$$
 Equation 23

To achieve the ultimate goal of high-voltage aqueous batteries, the anode is expected to exhibit a low redox potential with fast reaction kinetics (low $\eta_{negative}$) and a high HER overpotential.

Figure 12 schematically depicts the competition between the HER and the charge storage during the charging process. With the potential decreasing, the hydrated cations that involve in charge storage and hydronium/water that participates in the HER process diffuse/migrate towards the anode surface. In the diffusion step, the characteristics of electrolytes such as ionic conductivity, pH, salt concentrations have strong impacts on the concentration overpotential. Besides, the Helmholtz double layer formed on the electrode surface sets a diffusion barrier for charge carriers (e.g., H₃O⁺) through affecting the local arrangement of ions and water molecules. 102 Afterwards, the charge carriers get adsorbed on the electrode surface and compete for the electrochemical-active sites, during which the amount of free water molecules in electrolytes, hydrophilicity/hydrophobicity of electrode surface, and the density of electrochemical-active sites on the electrode surface are the determining factors on the concentration overpotential of HER. Notably, the density of electrochemical-active sites on the electrode surface is closely correlated to active materials' surface morphology, the adsorption preference on charge carriers, and the additives in electrolytes. Meanwhile, the adsorbed protons or water molecules will compete for electrons against the adsorbed/inserted charge carriers of the energy storage process, in which the intrinsic adsorption energy of H* intermediates on electrodes, energy storage chemistries, surface electrical conductivity, and water dissociation capability specifically in alkaline electrolytes play important roles. The proposed competition routes between HER and charge storage are expected to be applicable for most charge storage mechanisms, e.g., intercalation, conversion, plating, and pseudo-capacitance. 103

During the idling state of batteries, the HER-caused corrosion replaces the electrocatalytic reaction, playing the dominant role. The spontaneous corrosion reaction results from the anode's oxidation potential being lower than the reduction potential of water. Unlike the electrocatalytic HER, the corrosion consumes active mass of electrodes, thus causing self-discharge, decreasing

the CE, and shortening the cycle life of cells. During charging, reduction takes place on anode at a potential lower than its potential of zero charge (PZC); thus, the electrode surface is negatively charged. However, during idling, the anode surface is in contact with aqueous electrolytes, where depending on its PZC, the anode surface can be either positively charged or largely neutral. For example, for pure Zn metal, its PZC is lower than the potential corresponding to the lowest unoccupied molecular orbital (LUMO) of water at all pH values, there would be electron over spilled from Zn to the interface with the aqueous electrolytes, thus causing the Zn surface positively charged. An important consequence is that it would be the oxygen end of water that is oriented toward the electrode surface, which is the opposite compared to the scenario during plating of Zn. Thus, it can be posited that HER may be more severe during plating with protons pointed to Zn metal surface compared to idling. On the other hand, the PZC of pure iron's surface is higher than the potential corresponding to the LUMO of water at basic pH values; therefore, the surface of iron may not be heavily charged. As for corrosion, the thermodynamic factors on HER activity include the thermodynamic stability of water and the electrode's equilibrium electrode potential; the kinetic factors include the intrinsic adsorption energy of H* intermediates on electrodes, the wetting of electrodes by the electrolytes, and the surface electrical conductivity.

Overall, inhibiting HER in aqueous batteries can be achieved by strategies, including enhancing the thermodynamic stability of electrolytes, applying anodes with high selectivity towards the charge storage process, and reducing surface active sites that bind hydrogen. We will discuss these strategies in the following sections.

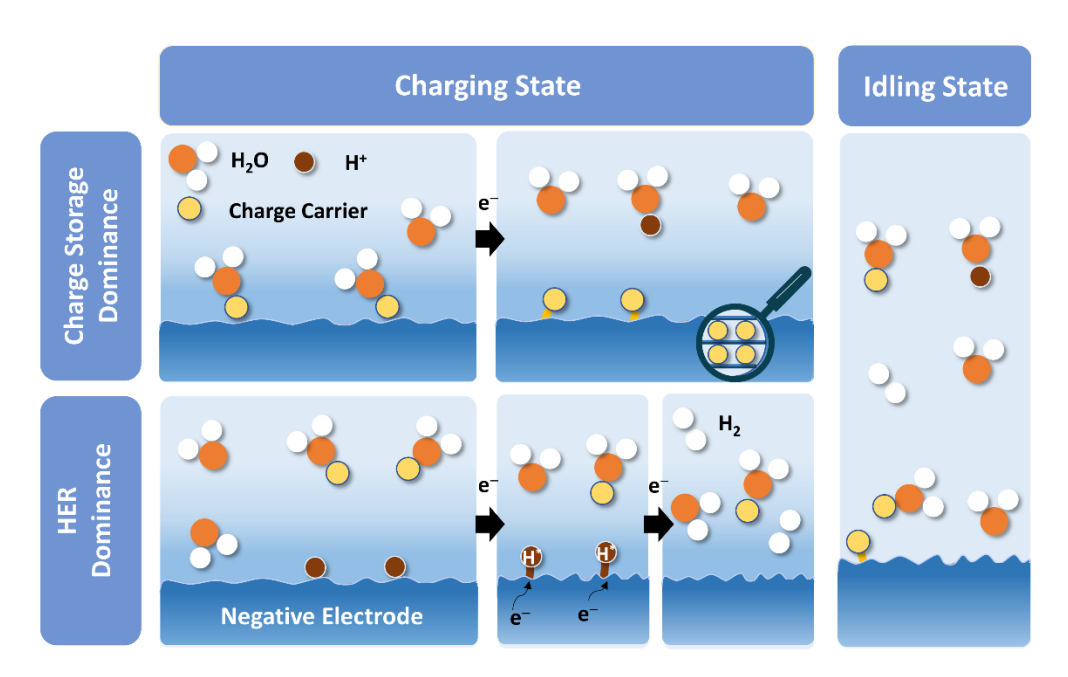


Figure 12. Schematic illustration of the competing routes between HER and redox reaction over the negative electrode during the charging process (left), where the cation charge carriers (yellow

balls) are either adsorbed on the electrode surface or inserted into the electrode, displayed by the schematic magnifier, and the electrode at the idling state (right). The blue gradient area near anode represents the Helmholtz double layer formed during charging state.

4.1.2 OER on Cathode:

OER can occur on the cathode during or after the charging process, and during charging, it competes against the charge storage process to contribute electrons. The conditions in Equation 24 need to be met to facilitate the stable operation of the cathode, where the $E_{positive}$ stands for the thermodynamic oxidation potential of the cathode, the $\eta_{positive}$ is the overpotential of cathode's oxidation reaction, the E_{OER} represents the thermodynamic OER potential, and the η_{OER} is the overpotential of OER reaction.

$$E_{positive} + \eta_{positive} < E_{OER} + \eta_{OER}$$
 Equation 24

For high-voltage aqueous batteries, the cathode should exhibit both a high redox potential on the basis of fast reaction kinetics (low $\eta_{positive}$) and a high OER overpotential. Their detailed competition process is schematically shown in Figure 13.

During charging, upon increasing the potential, hydrated OH⁻ or water that involves in the OER process migrates/diffuses towards the cathode surface, while the de-insertion of cation or the insertion of anion charge carriers for energy storage occurs in the electrodes. The OER and the charge storage will compete for the electrochemical–active sites on the electrode surface. Then, the adsorbed species of OER will compete to donate electrons to the cathode against the cathode itself in cation de-insertion or anion insertion. ^{104,105}

Similar to the HER, the charged cathode at idling states may also induce OER by directly reacting with H_2O when its equilibrium electrode potential is higher than the oxidation potential of water. In this case, the surface of the electrode may be negatively charged, where in the Helmholtz double-layer, water molecules may orient toward the electrode with their end of hydrogens. During idling, OER at the cathode and together with HER at the anode contributes to the self-discharge of batteries, which is often observed for aqueous batteries.

To suppress OER, thermodynamic strategies have been reported to improve the electrolyte stability by strengthening the O-H bonds of H_2O . Meanwhile, the strategies of kinetics aim at enhancing the OER overpotential by approaches such as tuning the selectivity of active sites, applying surfactants on electrodes, coating electrodes by the artificial solid-state interphases, and adding redox additives in electrolytes. It is worth noting that the field of OER is inundated with studies on OER-promoting electrocatalysts, where the trends of their varying catalytic properties have been reported. Here, we will provide some opposite-direction extrapolation of these trends to speculate what properties are conducive to OER suppression. OER suppression

has not received as much attention in comparison to the HER process of anode materials, where one factor is the inherently high overpotentials under acidic/neutral conditions.¹⁵

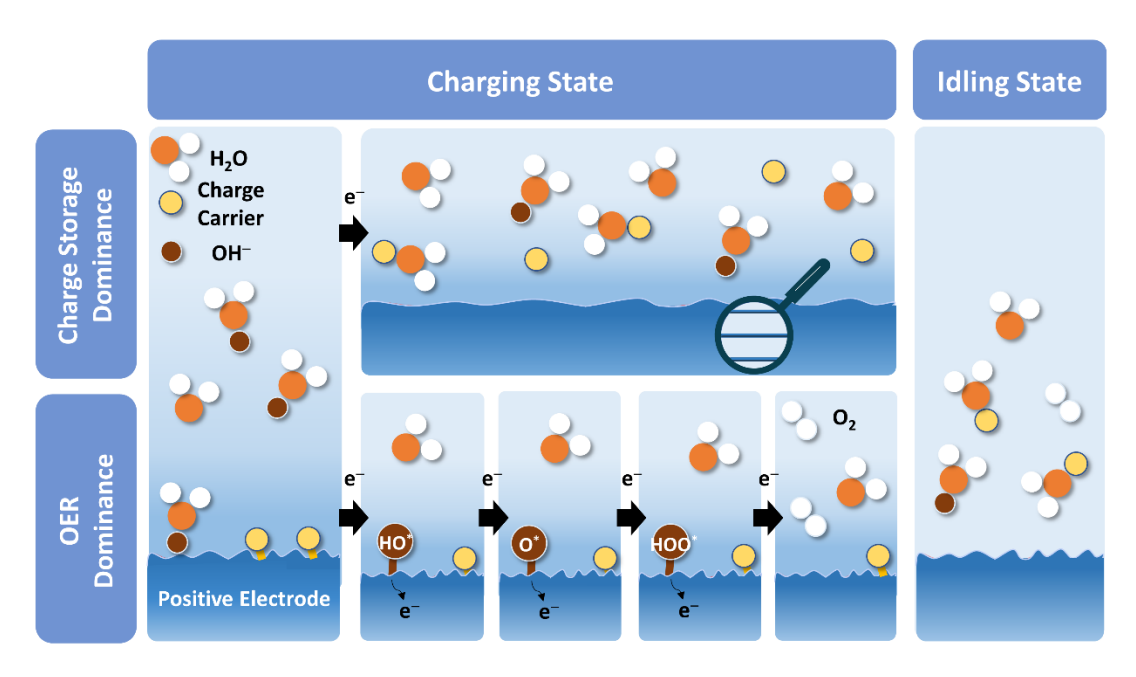


Figure 13. Schematic illustration of the competing routes between OER and the redox reaction over the positive electrode during the charging process (left), where the cation charge carriers (yellow ball) are either adsorbed on the electrode surface or intercalated into the electrode according to the energy storage chemistries at the initial state, and the electrode at the idling state (right).

4.2 HER/OER Suppression Strategies: A Thermodynamics Perspective

The thermodynamic stability of water primarily depends on its O–H covalent bond strength. In aqueous electrolytes, water has a complex chemical environment: either strongly coordinating cations, or weakly coordinating anions, or freely roaming in electrolytes. To promote the thermodynamic stability of aqueous electrolytes, efforts have been made to strengthen the O–H bonds of H₂O through tailoring its chemical environment. Besides, the specific thermodynamic HER/OER potentials are also affected by the pH of electrolytes, where HER and OER are disfavored in alkaline and acidic environments, respectively. In this section, we will review strategies, including 1) the strengthening of O–H bonds in water molecules, which could be achieved via the salt-concentrated electrolytes and the electrolyte additives, and 2) the decoupling of alkaline anolyte and acidic/neutral catholyte.

4.2.1 Strengthening O—H bonds in Water:

The strength of O–H covalent bonds in water is the key to its thermodynamic stability. As such, stiffening O–H bonds is regarded an effective route to suppress detrimental water electrolysis in aqueous batteries. In this section, we will discuss the pertinent strategies, including 1) the salt-concentrated electrolytes, where all H_2O molecules are arrested in cation's primary solvation shells, and O–H bond is reinforced, and 2) the electrolyte additives *e.g.*, cosolvents, salts, and organics, which improve the electrolyte stability by binding with cations or H_2O molecules.

4.2.1.1 Salt-Concentrated Electrolytes:

A high concentration of salts profoundly affects the chemical environment of both solvated ions and solvent itself, where the OER and HER properties of water can be significantly altered. Along this line, WiSE have been reported, where the dissolved ions exceed the H_2O molecules in their molar fraction of the solution. As a result, most H_2O molecules are bound in the primary solvation sheath rather than the secondary, and even the first solvation sheath can be incomplete compared to conventional coordination numbers. ¹⁰ In WiSE, the activity of water decreases, and there are few free water molecules, where these factors may shift the HER and OER onset potentials, bestowing a wider electrochemical stability window.

The salt prolifically used in WiSE is lithium bis(trifluoromethanesulfonyl)imide (LiTFSI), which exhibits high solubility in water. The 20 m (20 moles of solute in 1 kg water) LiTFSI electrolyte exhibits a H_2O/Li^+ molar ratio of 2.67. This electrolyte demonstrates a wide voltage window from 1.9 – 4.9 V vs. Li/Li⁺ at 10 mV s⁻¹. Based on the 21 m LiTFSI WiSE, the cell composed of LiMn₂O₄ and Mo₆S₈ electrodes presents an energy density of 100 Wh kg⁻¹ based on the mass of electrodes as well as excellent capacity retention (68% capacity remained after 1000 cycles at 4.5 C). The authors attributed the wider electrochemical stability window of the electrolyte partially to the stronger O-H in primary solvation sheath bonds, as discussed in Section 2, respectively. Besides, it was also pointed out that the wider window is partially due to the formation of SEI on the anode's surface, which would be expanded for discussion in Section 4.3.3. 10,28

To further decrease the number of free H_2O in electrolytes, a second salt (e.g., lithium trifluoromethanesulfonate (LiOTf)) was added into LiTFSI-based WiSE to form a 'water-in-bisalt' electrolytes (WiBEs) (21 m LiTFSI-7 m LiOTf). Consequently, the 21 m LiTFSI and 7 m LiOTf WIBS electrolyte contains 28 m Li⁺, thus decreasing the H_2O/Li^+ ratio to 2 and expanding the voltage window to 1.83-4.9 V vs. Li/Li^+ at a scan rate of 10 mV s⁻¹. Based on the electrolyte, the cell comprising the TiO_2 anode and the $LiMn_2O_4$ cathode delivers a discharge voltage of 2.1 V and an energy density of 100 Wh kg⁻¹ based on the mass of the electrodes. Likewise, the monohydrate melt (22.2 m LiTFSI-33.3 m LiPTFSI) and hydrate melt (19.4 m LiTFSI-8.3 m LiBET) present similar performances. ¹⁰⁸

Furthermore, mixing two room temperature hydrate melts at a eutectic ratio can minimize free H_2O in electrolytes.¹⁰⁹ For the mixture of $Li(TFSI)_x(BETI)_{1-x}(H_2O)_n$, the water amount (n) is at a minimum point of 2 when the molar ratio (x) is 0.7 (Figure 14a), where the water molecules are all isolated from each other and coordinated in the primary hydration shell of Li^+ .¹⁰⁹ The single

strong peak at 3565 cm $^{-1}$ in the Raman spectrum corroborates the diminishing number of free water molecules, where such a spectrum remembers that of crystalline hydrates (Figure 14b). Consequently, the electrolyte of eutectic hydrate melts exhibits a wide electrochemical stability window of 3.8 V ($^{\sim}1.25 - 5.25$ V vs. Li $^{+}$ /Li) at a low scan rate of 0.1 mV s $^{-1}$, thus enabling the stable operation of the Li $_{4}$ Ti $_{5}$ O $_{12}$ anode at 1.55 V vs. Li $^{+}$ /Li and the LiNi $_{0.5}$ Mn $_{1.5}$ O $_{4}$ cathode at 4.25 V and 5 V vs. Li $^{+}$ /Li.

However, the heavy usage of fluorinated lithium salts in highly concentrated electrolytes raises concerns on cost, toxicity, and environmental impacts. Alternatively, some metal acetates with a lower price and toxicity were used to produce the WiSE, such as the ammonium acetate $(NH_4Ac)^{110}$ and the potassium acetate $(KAc)^{111,112}$ Notably, the 30 m KAc electrolyte exhibits a wide stability window from -1.5–1.7 V vs. SHE at a scan rate of 1 mV s⁻¹. Besides, the amount of free H₂O molecules in the KAc-based WiSE could be further reduced by adding another metal acetate salt, including the NH_4Ac , lithium acetate $(LiAc)^{114}$ sodium acetate $(NaAc)^{115}$ For instance, in the eutectic mixture of 32 m KAc–8.0 m lithium acetate $(LiAc)^{114}$, the H₂O/cations ratio is as low as 1.3, theoretically with no free water molecules in the electrolytes.

Recently, inexpensive metal halide-based electrolytes have caught attention as well. For instance, the ZnCl₂-based WiSE has been broadly reported for applications in aqueous zinc-ion batteries. When increasing the salt concentration from 5.0 m to 30 m, the OER onset potential is considerably improved from 1.3 V to 1.8 V vs. SHE at a scan rate of 0.2 mV s⁻¹, demonstrating the higher oxidation stability of the electrolyte (Figure 14c). Furthermore, the effect of adding the second salt was also investigated. In an optimized concentration of 30 m ZnCl₂ + 10 m LiCl (referred to as 30ZC10LC) compared to that of 30 m ZnCl₂ (30ZC), the O–H stretching mode in Raman spectra blue-shifts from 3454 cm⁻¹ in 30ZC to 3481 cm⁻¹ in 30ZC10LC, which suggests shorter and stronger O-H bonds. Consequently, the thermodynamically more stable electrolyte could effectively mitigate the corrosion of the Zn metal anode due to HER and enable more reversible plating/stripping of Zn metal anode.

Another critical group of salt-concentrated electrolytes is called deep eutectic solvents (DES). 90,117,118 The aforementioned WiSE necessitates the high solubility of salts in water. In contrast, the DES electrolytes are generally composed of two more components besides water, including one salt and one hydrogen bond donor (HBD) that associate with each other through hydrogen bond interactions. Hore importantly, the produced DES is featured with a lower freezing point than that of each individual component, allowing the DES to remain in the liquid state at room temperature. Hore a trace amount of water (*i.e.*, hydrate water of salts) is added into the DES, the original chemical environment inside would be altered; specifically, the water molecules may partially replace HBDs and anions to enter cation's primary solvation shell. Similar to WiSE, no free water would exist in the DES-based aqueous electrolytes. For instance, a DES-based electrolyte composed of LiTFSI, Zn(TFSI)2, urea, and water with the Zn²⁺/Li⁺/urea/water molar ratio of 1:20:76:40 was investigated. The electrolyte presents a widened thermodynamic stability window from –1.26 to 1.66 V vs. SHE at a scan rate of 0.2 mV

s⁻¹. DFT–MD simulation reveals the unique electrolyte structure, where water confined in the cation solvation shell interacts with TFSI⁻ anions and urea through hydrogen bonds.

A localized WiSE can be formed near the surface of the anode by a metal organic framework (MOF) coating. A coating of ZIF-7 was doctor-bladed on Zn metal anode, through the tiny pores of which $Zn(H_2O)_6^{2+}$ has to dehydrate. The dehydration concentrates the electrolyte to become $Zn^{2+}\cdot SO_4^{2-}\cdot H_2O$ inside the MOF. The transition brought by the MOF coating is verified by the Raman spectra. The author observed that the v- SO_4^{2-} band shifts to a higher frequency at 992 cm⁻¹, indicating the stronger and closer $Zn^{2+}\cdot SO_4^{2-}$ ion coordination in MOF pores than that in bulk electrolytes (Figure 14d). They also observed the intensity-diminishing and blue-shifted O-H stretching vibration band, which suggests dehydration of salt ions (Figure 14e, f).

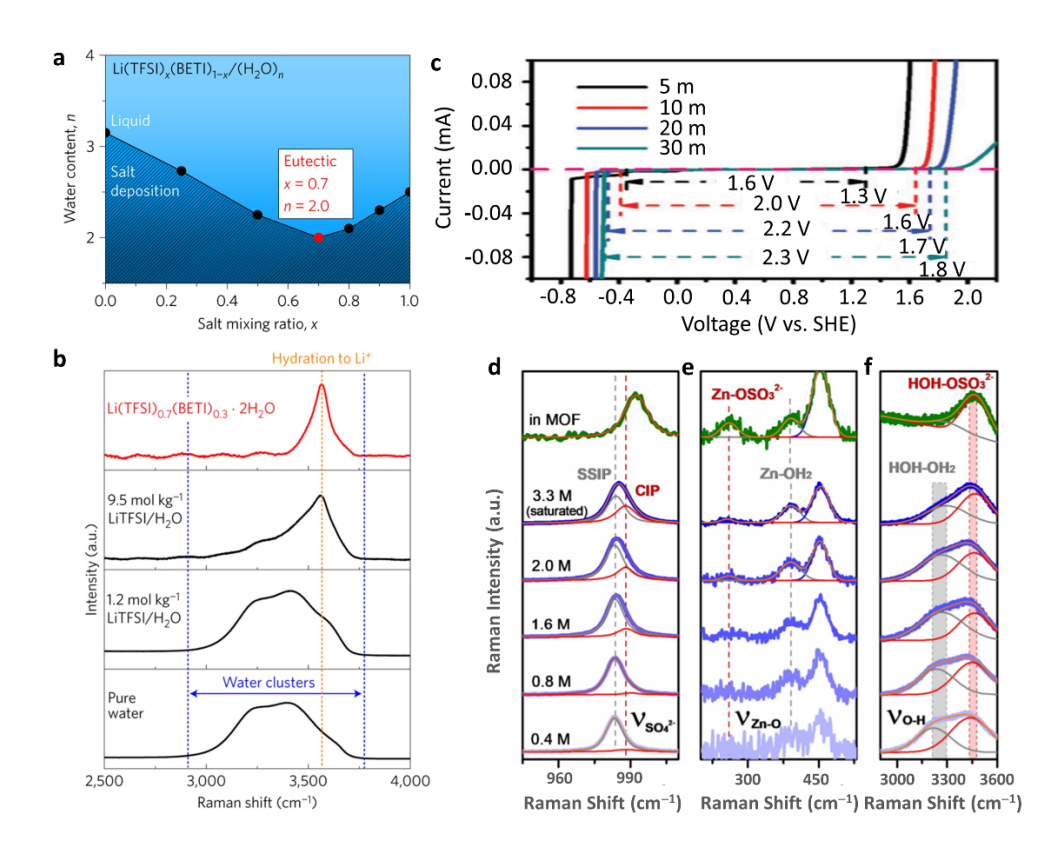


Figure 14. a) Liquidus line of Li(TFSI)_x(BETI)_{1-x} salt—water mixtures, where the Li(TFSI)_{0.7}(BETI)_{0.3} salt (x = 0.7) refers to the eutectic mixture that enables the formation of a hydrate melt state with the lowest water content (n = 2.0). Reproduced with permission from ref 109. Copyright 2016 Springer Nature. b) Raman spectra of pure water, Li(TFSI)_{0.7}(BETI)_{0.3} · 2H₂O, 9.5 m LiTFSI, and 1.2 m LiTFSI aqueous electrolytes, where the bands in the range of 2500–4000 cm⁻¹ correspond to the O–H stretching modes of water molecules and the bands in the range of 2900–

3700 cm⁻¹ (between the blue dashed lines) are assigned to the clusters of water molecules with various hydrogen-bonding environments, and the sharp peak at 3565 cm⁻¹ (orange dashed line) is ascribed to the Li⁺-solvated water molecules that are not clustered through hydrogen bonding. Reproduced with permission from ref 109. Copyright 2016 Springer Nature. c) Electrochemical stability window of ZnCl₂ aqueous electrolytes of different concentrations (*i.e.*, 5m, 10m, 20m, and 30m). Reproduced with permission from ref 116. Copyright 2018 Royal Society of Chemistry. Raman spectra of d) v-SO₄²⁻ band, e) Zn–O stretch bond, and f) H₂O stretch vibration band. Reproduced with permission from ref 120. Copyright 2020 Wiley-VCH.

4.2.1.2 Electrolyte Additives:

Besides the salt-concentrated electrolytes, other substances can also be added to electrolytes to modify the chemical environment of water and improve its thermodynamic stability. The additives could be categorized into two types: 1) non-electrolyte solutes that could reduce free water molecules by forming hydrogen bonds with them, 2) co-solvents that replace water in primary solvation shells to coordinate with cations, and 3) anti-solvents that replace water in primary solvation shells to promote the cation—anion coordination.

For the non-electrolyte solutes, they play the role of interrupting the fully "DDAA" bonded structure of free water molecules through solute-water chemical interactions, where a lack of hydrogen bonding strengthens the O-H bonds of water, akin to the function of the concentrated salt in WiSE. 121 Therefore, it also requires high concentrations of such solutes in electrolytes. The reported additives of this type include sugar¹²², and poly(ethylene glycol) (PEG)¹¹; both of them contain rich hydroxyl groups to bind with water molecules. For instance, sucrose, a disaccharide of glucose plus fructose, has outstanding solubility in water due to its many hydroxyl groups. 122 In concentrated sucrose solution (66.7 wt.% sucrose or 5.84 mol kg⁻¹), free water is significantly reduced in the unit volume of the electrolyte, thus strengthening the O-H bonds in water molecules. 122 The addition of the sugar solute helped realize a high stability voltage of ~ 2.8 V for a dilute electrolyte of 2.0 M NaNO₃. Similarly, water molecules can also be sequestered with redox-inert poly(ethylene glycol) (PEG), forming a so-called molecular-crowding electrolyte (Figure 15a). 11 The ethereal oxygen atom in PEG has a higher negative charge density than that in water molecules due to the inductive donating effects of alkyl groups in PEG. Therefore, a weaker H-bond forms between PEG and water molecules than that between two water molecules, thereby strengthening the O-H bonds in water molecules. At an optimizing composition of 2.0 m LiTFSI-94 wt.% PEG-6 wt.% H₂O, DFT-MD simulation shows that almost all H₂O molecules are surrounded by the PEG molecules, which explains the wide operation voltage of ~3.2 V. With this electrolyte, the full cell composed of Li₄Ti₅O₁₂ anode and LiMn₂O₄ cathode maintains a high energy density between 75 Wh Kg⁻¹ to 110 Wh Kg⁻¹ for over 300 cycles at 1 C. Furthermore, the novel electrolytes also reduce the usage of LiTFSI salt, which helps significantly cut the cost compared to the LiTFSI-based WiSE electrolytes.

Another type of additives serves as the co-solvent to solvate salts in electrolytes, where they could replace H_2O molecules in cation's primary solvation shells due to their higher Gutmann donor number than water. Taking dimethyl sulfoxide (DMSO) as an example, its Gutmann donor number (29.8) is well above that of water (18); thus, it would primarily coordinate with cations and appear in the Helmholtz double layer on anode during the charging process (Figure 15b). Meanwhile, the DMSO could also strongly interact with free H_2O molecules in electrolytes (Figure 15b), similar to the role of the PEG additive mentioned above. Both effects benefit the thermodynamic stability of water. Adding 20 wt.% DMSO into dilute 1.3 m ZnCl₂ aqueous electrolyte could widen the stability window from -0.76 V-1.24 V to -0.8 V-1.44 V vs. SHE at a scan rate of 1 mV s⁻¹ and significantly improve the cycling stability of Zn metal anode. The solution of the PEG additive mentioned above.

Yet another type of additives are named as anti-solvents because they are miscible with water solvent through H-bond interactions, while salts that provide charge carriers are not soluble inside. The provide charge carriers are not soluble to allow the provide charge carriers are not soluble to allow the provide charge carriers are not soluble to solve the provide charge carriers are not solves. The provide charge ch

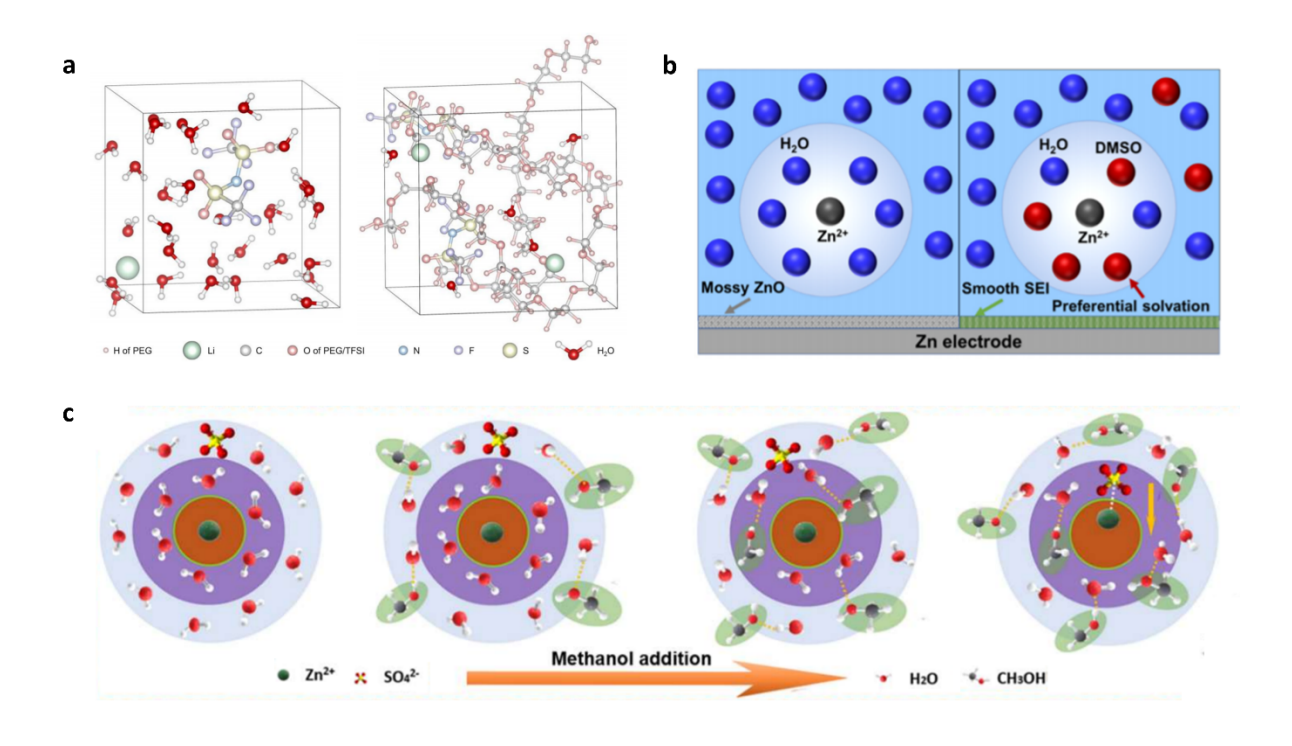


Figure 15. a) MD simulation on ions/water molecules coordination states in 2 m LiTFSI- H_2O (left) and 2 m LiTFSI-94% PEG-6% H_2O (right). Reproduced with permission from ref 11. Copyright 2020 Springer Nature. b) Schematic illustration of the Zn^{2+} solvation structure in water solvent (left) and in H_2O -DMSO dual solvents (right). Reproduced with permission from ref 123. Copyright 2020 American Chemical Society. c) Schematic illustration of Zn^{2+} solvation structure transition with the addition of methanol anti-solvent. Reproduced with permission from ref 124. Copyright 2021 American Chemical Society.

4.2.2 Decoupling Analytes and Catholytes:

As shown in Figure 4, the thermodynamic potentials for both HER and OER are sensitive to the pH of the electrolytes. Specifically, an acidic environment favors HER over OER, where the electrolyte is more anodically stable; conversely, a basic environment prefers OER to HER, where the electrolyte is more catholically stable. Adjusting the pH value of a homogeneous aqueous electrolyte cannot widen its electrochemical stability window; however, by blocking the neutralization between the basic analyte and the acidic catholyte, the electrolyte's window can be enlarged significantly. 125-131 For instance, by using Li_{1+x+v}Al_xTi_{2x}Si_vP_{3v}O₁₂ (LATSP), a ceramic, to divide the acidic catholyte (1 M H_2SO_4) from the alkaline anolyte (2 M KOH + 2 M LiOH)¹²⁶, the full cell comprising the Zn metal anode and the KMnO₄ cathode could work in a high voltage window of 2.8 V. In another study, a commercial bipolar membrane separates the acidic catholyte (0.3 M $H_2SO_4 + 3$ M $MnSO_4 + 0.06$ M $NiSO_4$) and the alkaline anolyte (3 M KOH + 0.3 M Zn(OH)₄²⁻) (Figure 16a). 129 The partitioned electrolyte exhibits a wide electrochemical stability window of ~3.45 V, which facilitates the stable plating of Zn metal and the deposition of MnO₂ over anode and cathode, respectively, at the scan rate of 5 mV s⁻¹. Furthermore, a three-chamber cell was reported, where the alkaline analyte and acidic catholyte are separated by two ionselective membranes and a chamber filled with neutral electrolyte (Figure 16b). 127,131 Such an design would improve the cell performance compared to the one-membrane two-chamber cell mentioned above by further mitigating the neutralization between H⁺ and OH⁻. The full cell with the MnO₂ cathode and the Zn metal anode could be charged to a high voltage of 3 V, where the cell's capacity barely fades after 116 deep cycles in contrast to the quick failure of the counterparts with the one-membrane and two chambers.

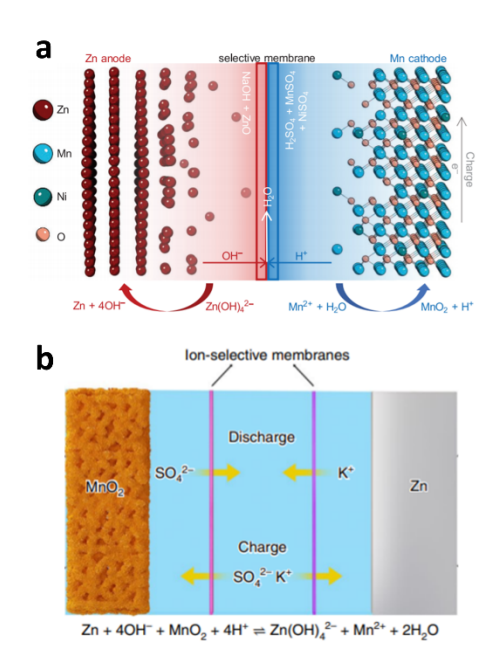


Figure 16. Schematic illustration of a) one-membrane two-chamber cell (Reproduced with permission from ref 129. Copyright 2020 Wiley-VCH.), and b) two-membrane three-chamber cell (Reproduced with permission from ref 127. Copyright 2020 Springer Nature.).

4.3 HER/OER Suppression Strategies: A Kinetics Perspective

From the perspective of kinetics, water electrolysis suppression strategies rely on enhancing the overpotentials of HER and OER on anode and cathode, respectively. As mentioned in Section 4.1, there are numerous factors for overpotentials. As for the electrode's properties, they include binding energy with water electrolysis intermediates, surface electrical conductivity, and the amount of exposed active sites. As for electrolyte properties, the pH and salt concentration matter. Experiment conditions are also relevant, including cycling rates, working temperature, the SOC, and so forth. In particular, efforts have been devoted to reducing the amount of active sites on electrode surfaces to realize the high-voltage aqueous batteries.

4.3.1 Water Electrolysis Anticatalysts:

The ideal electrodes of aqueous batteries should be good anticatalysts of water electrolysis, where they exhibit high selectivity towards the charge storage process while offering high electrochemical overpotential on the HER/OER processes. In order to achieve this, the material should exhibit appropriate binding energies with the HER/OER intermediates or superior energy-storage reaction kinetics so that energy-storage charge carriers can predominantly occupy the active sites. Meanwhile, compatible redox potentials are required for the material to meet the demand on high output voltages. Based on their properties, we will review the reported HER anticatalysts, including elemental metals, metal oxides, carbonaceous materials, and some other

less reported types, e.g., polymers, organics, and metal phosphates, and OER anticatalysts, including metal oxides, MOFs, and heteroatom-doped manganese oxides.

4.3.1.1 Promising HER Anticatalysts:

(1) Elemental Metals

Among the elemental metals, lead (Pb), zinc (Zn), and bismuth (Bi) are suitable anode materials for high–voltage aqueous batteries due to their high overpotentials towards HER. As shown in Figure 7a, these metals are situated at the left foot side of the volcano plots, far away from the peak, which indicates their weak binding energies with H* intermediates.

The Pb metal is commonly employed as an anode in lead–acid batteries and works by forming PbSO₄ in the discharge reaction, as shown in Equation 25.¹⁷ Its HER overpotential of $^{\sim}$ 0.58 V in 5 M H₂SO₄ (pH=-1) at the scan rate of 0.5 mV s⁻¹ is large enough to support the redox reaction theoretically occurring at around $^{-}$ 0.3 V vs. SHE.¹³² The cell comprising the Pb metal anode and PbO₂ cathode delivers a high voltage over 2 V in the $^{\sim}$ 5.0 M H₂SO₄ electrolyte. Nevertheless, the reaction product, PbSO₄ that exhibits poor electrical and HSO₄ $^{-}$ -ion conductivity, nucleates on the surface of the Pb anode, thus deteriorating the reaction kinetics for both HER and energy storage processes (Figure 17a).^{17,133} However, the PbSO₄ ununiform formation exacerbates the electrolyte consumption and causes the hydrogen evolution, thus hurting the cell's cyclic stability and shelf life.

$$Pb(s) + SO_4^{2-}(aq) \leftrightarrow PbSO_4(s) + 2e^-$$
 Equation 25

The problem can be resolved by adding a certain amount of conductive carbon, *e.g.*, activated carbon, carbon black, in the electrodes; the additives help homogenize the PbSO₄ formation and improve the reaction kinetics (Figure 17b). ^{17,133,134} Unfortunately, the carbon additives could trigger HER at a potential (*i.e.*, -0.427 V vs. SHE for AC) higher than the typical potential of Pb metal formation (-0.617 V vs. SHE). ^{135,136} The strategies for enhancing the HER overpotential over the carbon materials will be discussed in the next section.

The Zn metal anode receives much attention in recent years owing to its low cost and high theoretical capacity (~820 mAh g $^{-1}$). Furthermore, Zn metal exhibits a high HER overpotential (over 0.37 V in the 1 M ZnSO $_4$ electrolyte (pH=7) at the scan rate of 1 mV s $^{-1}$) that allows it to plate/strip at a low redox potential (-0.76 V vs. SHE) without vehement HER. $^{137-139}$ Cells based on the Zn metal anode are often reported to reach the cutoff voltage over 1.8 V. For instance, the Zn metal anode is coupled with zinc hexacyanoferrate (ZnHCF) cathode to present a high voltage of 1.85 V in the 1.0 M ZnSO $_4$ aqueous electrolyte. 139

Of note, the Zn metal anode operates with vastly different mechanisms under alkaline and acidic/neutral conditions, revealed by the Pourbaix diagram (Figure 17c). Under alkaline conditions, soluble $[Zn(OH)_4]^{2^-}$ is firstly formed in the discharging process and then decomposes into ZnO with poor electrical conductivity (Equation 26, 27). In the acidic/neutral electrolytes,

Zn metal strips into hydrated Zn^{2+} during discharge according to Equation 28. ^{141,142} Under alkaline conditions, it is the redox couple of $[Zn(OH)_4]^{2-}/Zn$ that dictates the redox potential of the Zn metal anode, which is at -1.20 V vs. SHE. Thus, despite the much lowered HER potential at pH 14, i.e., -0.826 V, the corrosion of the Zn metal anode can still take place.

Similar to the Pb metal anode in lead-acid batteries, the surface of Zn metal is also passivated by the reaction product of ZnO, thus leading to the large reaction polarization and the reduced capacity. In addition, like many other metal anodes in the battery field such as lithium¹⁴³, sodium¹⁴⁴, magnesium¹⁴⁵, and aluminum¹⁴⁶, the plating of Zn metal at rates that lead to the depletion zone near the surface according to the Sand's law can cause the formation of fluffy plated phases.¹⁴⁶⁻¹⁴⁹ This leads to the emergence of high-surface-area surface morphologies such as dendrites or whiskers or thin flakes.¹⁵⁰⁻¹⁵³ Such nanostructured surface morphologies with large surface areas would promote the HER by decreasing the concentration polarization of the HER process. The surface structures can fall off the surface of the electrode, thus losing the electrical contacts with the current collectors and becoming the dead mass.

$$Zn(s) + 40H^{-}(aq) \leftrightarrow Zn(OH)_{4}^{2-}(aq) + 2e^{-}$$
 Equation 26
 $Zn(OH)_{4}^{2-}(aq) \leftrightarrow ZnO(s) + 2OH^{-}(aq) + H_{2}O(l)$ Equation 27
 $Zn(s) \leftrightarrow Zn^{2+}(aq) + 2e^{-}$ Equation 28

Bi metal inhibits HER due to its weak binding energy with H* intermediates. In the 6.0 M KOH electrolytes, it can be deep-charged to -1.155 V vs. SHE at the scan rate of 5 mV s⁻¹, thus enabling the redox reaction at ~-0.655 V vs. theoretical HER potential at this pH value^{137,154} Furthermore, Bi can be coated over other materials' surface to enhance their inertness towards HER. Bi₂S₃, as an electrode additive, undergoes a reduction reaction during the charging process; the produced Bi metal is deposited onto the anode surface, thus elevating the HER overpotential and extending the lower operation window to -1.15 V vs. SHE at a rate of 100 mA g⁻¹. ^{155,156}

Of note, one unique feature of some metal anodes is that the HER can occur during the corrosion reactions of these metals in aqueous electrolytes, owing to their stripping potential lower than that of HER.¹⁵⁷ In batteries based on the Zn anode, corrosion is a severe issue since the reaction is spontaneous no matter the SOC of the cells. The corrosion reactions constantly consume the active mass and electrolytes (Figure 17d, e). ^{117,157-159}

In the corrosion reactions, the anodic half-reaction is the metal dissolution, and the cathodic half-reaction is the reduction of protons/water molecules to form hydrogen gas molecules. ¹⁵⁷ Specifically, the HER would proceed in two steps via the Volmer–Heyrovsky mechanism, where the protons and water molecule are the sources of hydrogen in acid and neutral/alkaline solutions, respectively, and they would receive electrons from the anodic half-reaction to form the H* intermediate and H_2 , consecutively (Figure 17d). ¹⁵⁷

It should be noted that the water molecules involved in the corrosion reaction can be not only the free ones but those in the solvation sheaths of cations and anions. ^{118,160} Furthermore, in mild

acid/neutral/alkaline environments, the chemical corrosion of metals can produce some electrochemical-inert by-products. 118,161,162 For instance, the Zn metal anode experiences severe corrosion after ten days of immersion in 3.0 M ZnSO₄ solution, and its surface is covered by loose sheet-like Zn₄(OH)₆SO₄·5H₂O side product (Figure 17f). The continuous corrosion causes piecemeal loss of the Zn metal anode (Figure 17g). 161,163

The corrosion problem due to HER could be addressed from both the anodic half-reaction and the cathodic half-reaction perspectives. As for the anodic half-reaction, it is promising to increase the oxidation potentials of metals, which reduces the overall electromotive force (voltage) of the corrosion reaction, thus suppressing the hydrogen evolution. Alloying is a common strategy to increase corrosion potentials. For instance, a Cu/Zn composite anode was fabricated by *in situ* growing a thin layer of Cu metal on the Zn metal surface. During the electrochemical cycling, the deposited Zn metal alloys with the Cu metal to form the intermetallic phases of Cu₅Zn₈ and Cu₁Zn₁. The polarization test reveals that the Cu-Zn alloy anode exhibits slightly higher corrosion potential (E_{corr} , -0.966 V vs. SCE) and a much lower corrosion current (I_{corr} , 7.94 μ A cm⁻²) than that of pristine Zn metal anode (-0.976 V vs. SCE, 37.15 μ A cm⁻²) in the 3.0 M ZnSO₄ electrolyte (Figure 17h). Furthermore, the Cu-Zn alloy anode maintains the smooth surface with no corrosion by-products after soaking in 3.0 M ZnSO₄ electrolytes for 30 days. However, the above strategy suffers from the disadvantage that the reversible capacity depends on the amount of Cu metal in the electrode.

Similarly, a thin layer of indium metal is introduced on the Zn metal surface to inhibit the corrosion; the protection effect is, unfortunately, temporary since the Zn prefers to deposit on the top of the coating surface, and the corrosion still exists when Zn deposits are exposed to the electrolytes. ¹⁶³

The problem can be solved by applying some materials with low electrical conductivity but high ionic conductivity as a coating on the Zn metal anode such as metal oxides $(Al_2O_3^{164}, TiO_2^{165})$, and ZnO^{166} or MOFs (ZIF- 7^{120} and HKUST- 1^{167}). Therein, the Zn^{2+} would transfer through the coating and deposit beneath it so that the protective effect can last for long time. Besides, the artificial SEI layer can also play the role of a physical barrier between the electrode and electrolytes; meanwhile, its electronic insulating nature may eradicate the electrochemical corrosion problem. Related works will be introduced in Section 4.2.2.3.

The corrosion resistance of the Zn metal is closely correlated to the crystalline planes exposed to the electrolyte. Generally, the (002) crystal plane of Zn exhibits better corrosion resistance than the preferential orientations of (101), (103). An explanation is that the (002) is the most closely packed plane in the hexagonal close-packed (hcp) lattice; it is more resistant to corrosion since the atoms have a higher binding energy. The interest of the corrosion is the corrosion of the atoms have a higher binding energy.

To obtain the crystal plane along the [002] orientation, several strategies have been explored to date. One strategy is to introduce additives in electrolytes that serve as capping agents to control the growth direction, with the examples of boric acids¹⁷⁴ and polyethylene glycol (PEG)¹⁷⁵. The

second strategy to deposit Zn epitaxially on the substrate. It was reported that the basal plane of graphene matches that of the (002) plane of Zn metal; thus, the substrate with the basal plane of well-dispersed graphene layer parallel to the electrode surface guides the Zn deposition along the [002) direction.¹⁷³ It should be mentioned that Zn that preferentially grows in (002) planes resist the dendrite formation, which further promotes the cycling efficiency of the Zn metal anode (Figure 17i).

Regarding the cathodic half-reaction of the corrosion reaction, it is reasonable to hypothesize that the adsorption energy of H* intermediates on metal anodes is a critical factor influencing the hydrogen evolution rates, owing to the similar mechanisms between corrosion and electroreduction of water. Therefore, the corrosion could be suppressed by enhancing the HER overpotential of the electrode; a facile strategy is to introduce HER-inert additives onto the electrode. For instance, Hg, Pb, Bi, and their oxides have been widely used to inhibit Zn metal corrosion. Recently, less toxic substances such as Zn-Al-In-layered double hydroxides and Zn-Ni-In alloys have been employed. Recently, less toxic substances such as Zn-Al-In-layered double hydroxides.

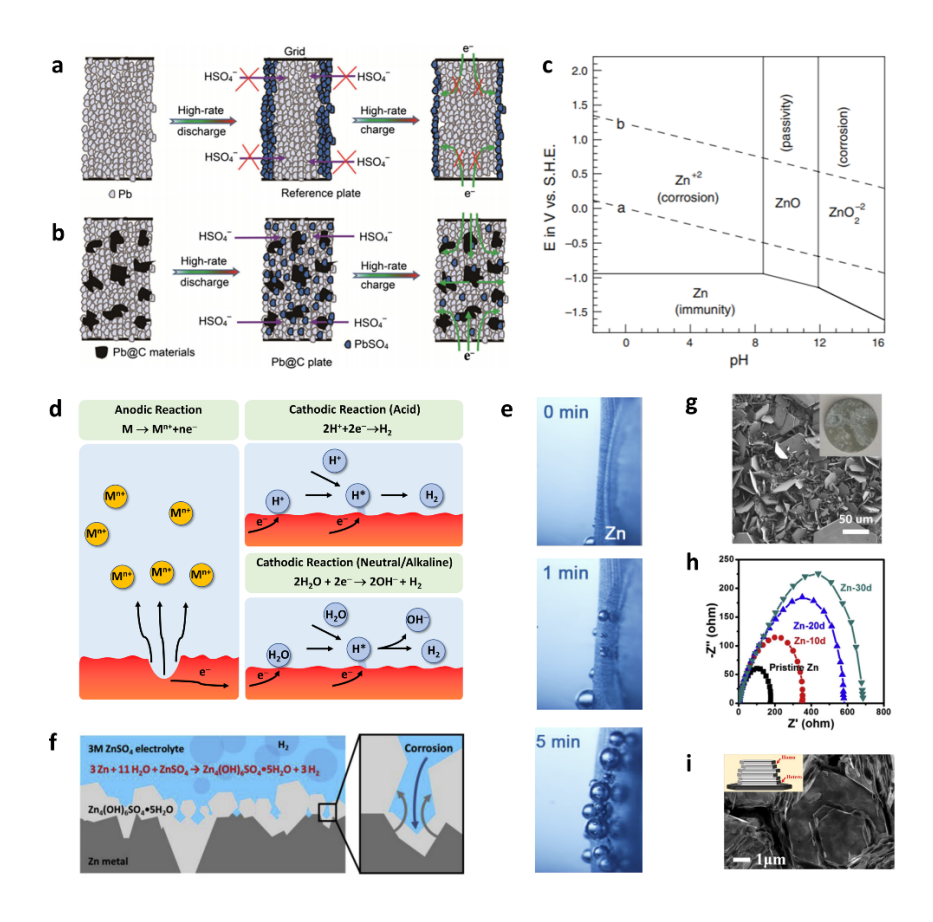


Figure 17. Schematic illustration of a) irreversible reaction occurred over Pb metal anode and b) the improvement through adding carbon within the electrodes. Reproduced with permission from ref 133. Copyright 2015 Elsevier. c) Pourbaix diagram of Zn metal. Reproduced with

permission from ref 140. Copyright 1997 Elsevier. d) Schematic illustrating the electrochemical corrosion process on metal anodes. e) *In situ* optical microscopic observation of hydrogen evolution on Zn metal anode in 0.5 M LiTFSI + 0.5 M Zn(TFSI)₂ aqueous electrolytes. Reproduced with permission from ref 117. Copyright 2019 Elsevier. f) Schematic illustration of the corrosion accompanied by the formation of electrochemical-inert by-products on Zn metal anode in 3.0 M ZnSO₄ aqueous electrolytes. Reproduced with permission from ref 161. Copyright 2020 Elsevier. g) SEM image of corroded Zn metal anode after immersion in 3.0 M ZnSO₄ solution for 30 days; inset is the optical image of the sample. Reproduced with permission from ref 161. Copyright 2020 Elsevier. h) EIS results of the Zn | |Zn symmetrical cells with 3.0 M ZnSO₄ electrolyte after resting for 0 days (pristine Zn), 10 days (Zn-10d), 20 days (Zn-20d), 30 days (Zn-30d). Reproduced with permission from ref 161. Copyright 2020 Elsevier. i) SEM image of Zn deposits on graphene-coated stainless steel; inset is the schematic illustration of the epitaxial deposition pattern. Reproduced with permission from ref 173. Copyright 2019 AAAS.

(2) Metal Oxides

Metal oxides represent another essential group of anodes in high-voltage aqueous batteries. Their high overpotentials towards HER originate from several characteristics. Firstly, they have appropriate binding energies with the H* intermediate. Besides, they commonly work via the pseudocapacitive mechanism, which bestows them excellent reaction kinetics of charge storage; furthermore, the predominant occupation of the active sites on the electrode surface by energy-storage charge carriers would effectively increase the HER polarization. Of note, the water reduction of metal oxides closely correlates to their properties, including the transition metal valence states, crystallinity, and defects. Herein, we summarize the materials with high HER overpotentials and discuss the impacts of the controlling factors on their performance.

Taking TiO₂ as an example, it exhibits a weak bonding strength towards the H* intermediate, indicating its inhibition nature on H* absorption. This offers TiO₂ the high HER overpotential, thus allowing its reversible storage/release of cations at deep potentials in aqueous systems. In the acidic electrolyte of 1.0 M AlCl₃ (pH \approx 3), hydrogen evolution does not take place on TiO₂ until -1.2 V vs. SHE at the scan rate of 20 mV s⁻¹, corresponding to a high HER overpotential of $^{\sim}1.02$ V. Sonsequently, most likely, the proton storage/release, albeit the authors assigned that to Al³⁺ storage/release, can stably proceed at -0.8 V vs. SHE via the Ti⁴⁺/Ti³⁺ redox reactions. In the LiOH-based alkaline electrolytes, Li⁺ ions can be reversibly accommodated in anatase-type TiO₂ anode at a low potential of -1.22 V vs. SHE and a scan rate of 10 mV s⁻¹, indicating an HER overpotential of 380 mV. Besides, TiO₂ also exhibits superior performance in mild/neutral electrolytes, e.g., 1.0 M Na₂SO₄, where HER does not occur above -1.2 V vs. SHE.

Similar to Bi metal, TiO_2 has also been applied as a HER-inhibition coating. Fe₃O₄@ TiO_2 composite electrode is synthesized through atomic layer depositing of TiO_2 over Fe_3O_4 nanorod arrays, thus enabling a low potential of -1.0 V vs. SHE for 1.0 M Li_2SO_4 electrolyte

at a scan rate of 50 mV s⁻¹. Of note, structural defects, *e.g.*, oxygen vacancies, may promote HER on TiO_2 . ^{187,190} First, the incorporation of oxygen vacancies by Ti^{3+} reduces the bandgap, which increases the electrical conductivity and benefits the reaction kinetics of both the HER and energy storage processes. Second, the oxygen vacancies may bind the H* intermediate better, thus enhancing the HER activity over TiO_2 .

Similarly, the performance of VO₂ also strongly depends on the valence states of V element. When the material contains both V^{4+} and V^{5+} , the primary charge storage reactions involve the transitions of $V^{5+} \rightarrow V^{4+}$ and $V^{4+} \rightarrow V^{3+}$, and the HER begins at around -0.4 V vs. SHE in the 1.0 M Na₂SO₄ aqueous electrolyte at a scan rate of 50 mV s⁻¹. Alternatively, when the VO₂ samples contain V^{4+} and V^{3+} , the reactions are $V^{4+} \rightarrow V^{3+}$ and $V^{3+} \rightarrow V^{2+}$, and the H₂ evolution potential drops to < -0.8 V vs. SHE under the same conditions. The phenomenon relates to the predominant occupation of active sites by charge storage charges at the lower potential. Alternatively in particular, the new redox pair of $V^{3+} \rightarrow V^{2+}$ elevates the working voltage of the full cell to 2.2 V.

In the case of surface-hydroxylated Mn_5O_8 ($Mn^{2+}_2Mn^{4+}_3O_8$) (Figure 18a), it can realize a deep operation potential at -1.09 V vs. SHE with the HER overpotential of 0.64 V in the 1.0 M Na_2SO_4 electrolyte at rates from 1 mV s^{-1} to 1000 mV s^{-1} (Figure 18b). This material shows superior cyclic stability at high cycling rates (e.g., 5 A g^{-1}) but undergoes rapid capacity decay at lower cycling rates (0.5 A g^{-1} and 1 A g^{-1}). It seems that a high-rate charge storage reaction increases the concentration overpotential of HER, kinetically suppressing or masking it. The poor low-rate-behavior may be an inherent challenge since Mn^{3+} is known for a high HER activity. Furthermore, the DFT calculation was conducted for the surfaces of hydroxylated Mn_5O_8 , pure Mn_5O_8 , and Mn_3O_4 . The hydroxylated Mn_5O_8 with a weak H^* binding energy of 1.41 eV can better inhibit water dissociation than pure Mn_5O_8 (0.45 eV) and Mn_3O_4 (0 eV) (Figure 18c). According to the Arrhenius equation, it is expected that the hydroxylated Mn_5O_8 has a water dissociation rate 17-orders of magnitude lower than that of Mn_3O_4 at room temperature. Besides, the rate-dependence behavior also relates to the kinetics of the energy storage process. The faster reaction kinetics favors the occupation of active sites on the anode surface, thus increasing the overpotential of the HER process.

Besides, the impacts of crystallinity of the birnessite-type MnO_2 on its HER activity was also studied. The disordered $Na_{0.27}MnO_2$ birnessite was synthesized through a solid-state reaction between NaOH and Mn_3O_4 ; the ordered $Na_{0.19}MnO_2$ birnessite was synthesized via the thermal decomposition of $NaMnO_4$ at 800 °C. CV curves reveal the strong HER passivation effect on the disordered $Na_{0.27}MnO_2$ birnessite compared to the ordered $Na_{0.19}MnO_2$ birnessite and the commercial β - MnO_2 . The disordered $Na_{0.27}MnO_2$ birnessite can be reduced to a deep potential of -1.05 V vs. SHE in the 0.1 M Na_2SO_4 electrolyte at a scan rate of 5 mV s⁻¹. This fact might be correlated to the predominantly exposed (001) planes in the disordered $Na_{0.27}MnO_2$ birnessite, which is both thermodynamically stable and HER inert.

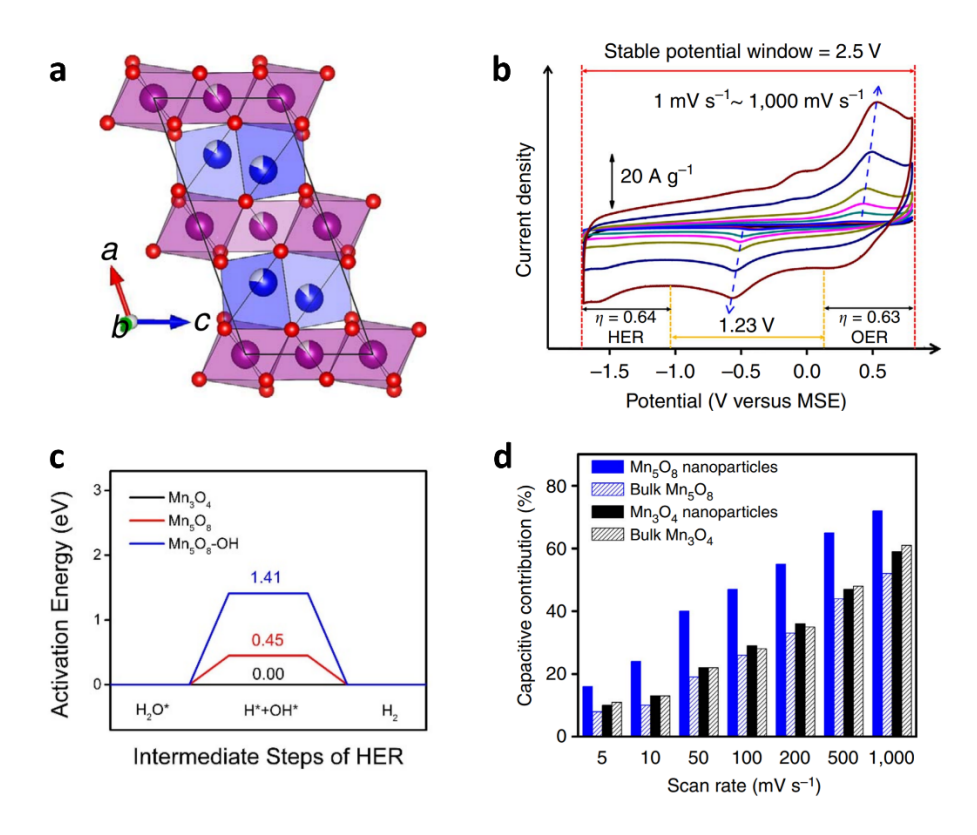


Figure 18. a) Schematic of the crystal structure of Mn_5O_8 . b) CV curves of Mn_5O_8 electrode at various scan rates from 1 mV s⁻¹ to 1000 mV s⁻¹, simultaneously exhibiting large overpotential towards HER/OER. c) Activation energies of forming the HER intermediates for hydroxylated Mn_5O_8 (Mn_5O_8 -OH), Mn_5O_8 , and Mn_3O_4 . d) Capacitive contribution to the overall capacity at various scan rates from 5 mV s⁻¹ to 1000 mV s⁻¹ of Mn_5O_8 and Mn_3O_4 nanoparticles and bulk materials. Reproduced with permission from ref 12. Copyright 2016 Springer Nature.

(3) Carbonaceous Materials

In aqueous electrolytes, carbonaceous materials are often employed as electrodes in electrochemical capacitors, storing charges through the surface electrical double layer effect. They exhibit high electrical conductivity, fast reaction kinetics, high chemical stability, and low cost. Furthermore, some carbon materials possess high HER overpotentials, which renders them suitable anodes for aqueous batteries. Besides, they are also employed as HER-inhibition coating over other materials. For example, graphitic carbon presents superior HER resistance because the nonpolar structure of the sp² carbon planes exhibit weak ion—dipole force to adsorb H⁺ from the electrolytes. Nevertheless, carbonaceous materials, particularly on edge sites, are rich in defects, *e.g.*, vacancies, doped heteroatoms (N or O), and functional groups. They may serve as the active sites to catalyze water electrolysis, thus hurting cell's electrochemical performance and calendar life. 198,199

In order to inhibit HER on the carbonaceous materials, the primary strategy is to introduce heteroatom doping or functional groups, which alters the electronic structure of the adjacent carbon atoms. Particularly, nitrogen doping, *e.g.*, pyrrolic N, is reported effective. It was experimentally confirmed that the pyrrolic N–doped activated carbon (NAC) electrode exhibits a lower onset potential for hydrogen evolution (-0.61 V vs. SHE) than that of the pristine AC electrode (-0.43 V vs. SHE) at the scan rate of 1 mV s⁻¹ in the 5.0 M H₂SO₄ aqueous electrolyte. The enhancement relates to two factors: (1) the carbon atoms adjacent to the pyrrolic N dopants form weaker bonds with the H* intermediate due to their electron deficiency, and (2) the pyrrolic N dopants exhibit high bonding strength with the H* intermediate, which increases the energy barrier for the H₂ release. In addition, the P–doped AC (P–AC) also shows enhanced HER suppression capability over the pristine AC. DFT calculation results indicate that the P-doping increases the adsorption energy of H* over the host, thus resulting in the HER inhibition in P-AC (Figure 19a). 203

Regarding the functional groups, oxygen-based ones are reported. For instance, oxygenated functionalities (carboxylic, quinone, phenolic, and ether) were introduced into AC through immersing it in 20 wt.% H₂O₂ solutions, thus negatively shifting the HER potentials to -0.59 V vs. SHE at 2 mV s⁻¹ in CV tests.²⁰⁴ It is worth noting that the introduced oxygenated functionalities also contribute additional capacity through pseudo-Faradaic redox reactions in the aqueous electrolytes.²⁰⁴ Carbon fibers (CF) was synthesized with rich oxygenated functionalities by heating carbon–fiber–reinforced polymers in air.²⁰⁵ The material exhibits a high HER inertness, thus expanding the HER onset potential to -1.16 V vs. SHE in the 1.0 M Na₂SO₄ electrolyte, measured at 50 mV s⁻¹ in CV tests, and the symmetrical supercapacitors based on the material can be charged to a high working voltage of 2.4 V. Note that the scan rate of 50 mV s⁻¹ seems too high to measure the onset potential of HER and OER.

Doping the carbonaceous materials with alkaline metal ions has been demonstrated as another effective method to ameliorate the side effects brought by the defects. Electroreduction is the primary method to dope alkaline–metal ions into carbonaceous hosts. ²⁰⁶⁻²⁰⁹ In one work, the carbonaceous materials were cycled in the 1.0 M Na₂SO₄ solution for 100 CV cycles at the scan rate of 25 mV s⁻¹ within the potential range of -1.255 - 0.245 V (vs. SHE). Consequently, Na⁺ ions are adsorbed over the defect sites which may be vacancies or consist of O-adatoms (i.e., C=O²¹⁰, O-H, C-O-C²¹¹) (Figure 19b, c), which can be validated by the XPS measurements and DFT calculations. ²⁰⁶ Due to the defect binding and the Na⁺ electrostatic shielding effect, the treated carbonaceous hosts present a much reduced HER activity relative to that of pristine porous carbon (PC), defect–free graphene layer, and heteroatom–rich AC (Figure 19d). ²⁰⁶ Furthermore, when this treated carbon anode was coupled with OER–inert cathode materials such as the Na_{0.25}MnO₂, the cell exhibited a wide operation window of 2.7 V demonstrated at rates of 1 to 25 mV s⁻¹ in CV and 2 A g⁻¹ in galvanostatic charge-discharge (GCD) tests. ^{206,212} Considering the clean/facile synthesis procedure, this work presents a promising route to design anodes in high–voltage aqueous batteries. It is worthwhile to emphasize that the adsorption of Na⁺ has to

be at least partially irreversible. It would negate the purposes if these adsorbed Na⁺ are released to the full cells to be assembled, which might revamp the defect sites of the carbon anode.

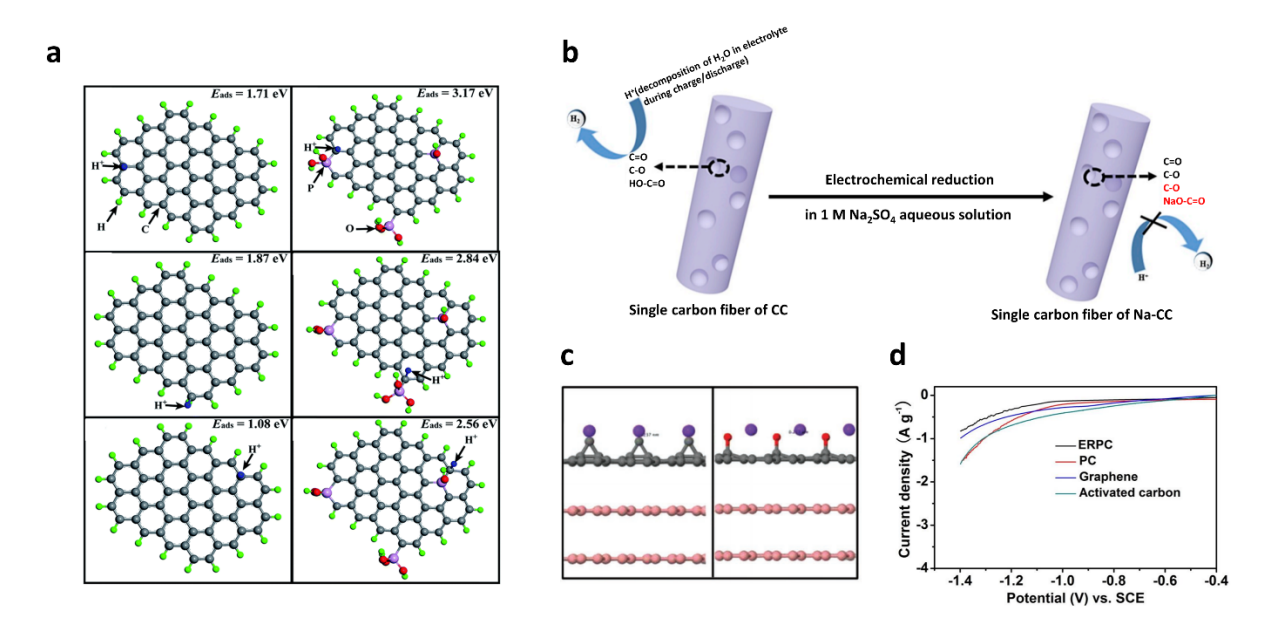


Figure 19. a) Optimized geometric structures and adsorption energies of H⁺ at different sites on AC (left) and P-AC (right). Reproduced with permission from ref 203. Copyright 2017 Royal Society of Chemistry. b) Schematic illustration of the electroreduction method to synthesize Na⁻-doped carbon cloth (Na-CC) materials. Reproduced with permission from ref 207. Copyright 2019 Elsevier. c) Simulation of adsorption of Na-ions on the prepared porous carbon (side view of Na⁺ adsorbed on C defect sites (left) and O defect sites (right) of graphite). Reproduced with permission from ref 206. Copyright 2018 Wiley-VCH. d) Linear sweep voltammetry (LSV) curves for the electrochemically reduced porous carbon (ERPC), PC, graphene and activated carbon electrodes separately in the 1.0 M Na₂SO₄ aqueous electrolyte at a scan rate of 1 mV s⁻¹. Reproduced with permission from ref 206. Copyright 2018 Wiley-VCH.

(4) Other Materials

Some polymers, organics, and metal phosphates that possess high HER overpotentials are reported as anodes in aqueous batteries. Herein, these types of materials and the factors affecting their HER activities will be discussed.

Polyimides (PIs) and their derivatives are widely applied as anodes in metal-ion aqueous batteries. Their HER activities can be tuned through changing the molecular structures. DFT calculations were conducted on two types of them: poly(naphthalene four formyl ethylenediamine) (PNFE) and poly(benzene four formyl ethylenediamine) (PBFE). The results revealed insights: (1) the most active sites for H* adsorption in the PI's structure are oxygen

atoms, (2) PNFE is more inert towards HER due to the larger energy barrier to form the H* intermediate (2.11 eV) than the PBFE counterpart (1.94 eV), and (3) over half of the HER active sites are preoccupied by alkaline ions (e.g., Li⁺ and Na⁺) during the charging process, resulting in sluggish kinetics of the HER process (Figure 20). Consequently, the composite anode (PNFE/CNT) delays H₂ evolution until a low potential of -1.23 V vs. SHE in the 0.5 M Li₂SO₄ electrolyte at the rate of 5 mV s⁻¹. The full cell composed of the PNFE/CNT anode and the LiMn₂O₄ cathode delivers a high voltage of 2 V. Besides, poly[N,N'–(ethane–1,2–diyl)–1,4,5,8–naphthale netetracarboxii mide] (PNDIE) was reported with a deep HER potential (-0.7 V vs. SHE) at 1 mV s⁻¹ in 2.5 M Ca(NO₃)₂.²¹⁸

In addition, some organics such as 3,4,9,10–Perylenetetracarboxylic diimide (PTCDI)¹⁸⁹ are potentially good anodes for high–voltage aqueous batteries. It was reported that PTCDI can reversibly store NH_4^+ from the 1.0 M (NH_4)₂SO₄ (pH=6) electrolyte via a process of two–step-carbonyl enolation.^{189,219} Of note, the anode can be charged to a deep potential of –0.85 V *vs.* SHE without noticeable H_2 evolution, measured by CV at 0.5 mV s⁻¹, demonstrating a high HER overpotential of at least 0.55 V.

Polyanion compounds such as $TiP_2O_7^{220}$, NASICON-type $LiTi_2(PO_4)_3$ (LTP)²²⁰, and NASICON-type $NaTi_2(PO_4)_3$ (NTP)²²¹⁻²²³ represent another group of materials displaying both high overpotential towards HER and suitable working potentials. TiP_2O_7 inhibits the hydrogen evolution until the potential of -0.6 V vs. SHE in the 5.0 M $LiNO_3$ electrolytes at the scan rate of 0.2 mV s⁻¹, deeper than its redox potential at -0.38 V vs. SHE.²²⁰ The LTP electrode presents an HER onset potential at -0.7 V vs. SHE, while the Li^+ intercalation proceeds at \sim -0.52 V vs. SHE in the same conditions. The NTP anode holds back HER until a potential lower than -1 V vs. SHE in both the 2.0 M NaOH and the 4.0 M NaOH electrolyte at the scan rate of 0.5 mV s⁻¹, below the Na⁺ intercalation potential around -0.9 V.²²² The high OER resistance of the materials may relate to the Ti^{4+} inside, which may exhibit suitable binding energy with the OER intermediates due to their band structures.

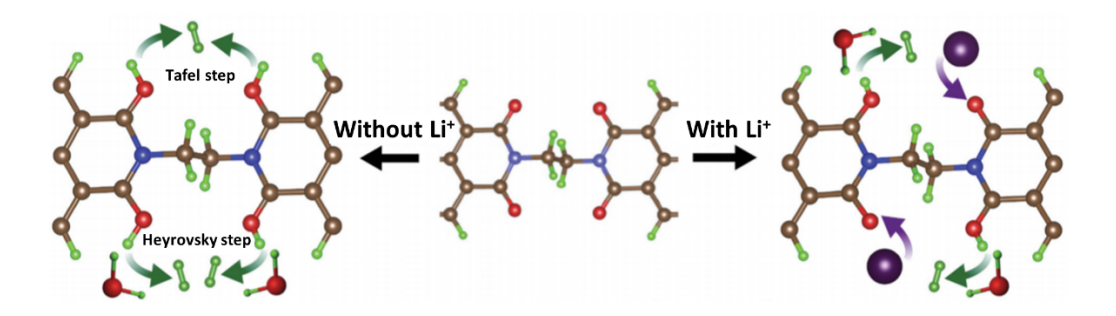


Figure 20. Schematic illustration of the HER passivation from reducing the number of active sites via Li[†] adsorption. Reproduced with permission from ref 216. Copyright 2016 Wiley-VCH.

4.3.1.2 Promising OER Anticatalysts:

Cathode of aqueous batteries should exhibit befitting binding energies with the OER intermediates (HO*, O*, OOH*) that are unfavorable to OER; or cathode exhibits superior reaction kinetics to achieve the high selectivity of charge carriers over OER intermediates. To date, materials that have been identified to meet these requirements include metal oxides such as heteroatom-doped manganese oxides and MOFs. Descriptors of these materials, *e.g.*, valence states, defects, crystallinity, and crystal structures, have impacts on the OER-inhibition performance. Herein, these materials and their associated descriptors will be discussed.

(1) Metal Oxides

According to the volcano plots (Figure 10c), some metal oxides (e.g., $SnO_2^{221,224}$, TiO_2^{225} , NbO_2^{226} , MnO_2^{227} , $Ta_2O_5^{228}$, PbO_2^{229} , and SiO_2^{230}) present either too high or too low binding energies with the OER intermediates, thus resulting in high overpotentials towards OER. Among them, few, e.g., Mn-based oxides and PbO_2 , have been reported as the cathodes in high-voltage aqueous batteries.

The first example is PbO₂, where its weak adsorption energy towards the intermediates bestows PbO₂ high inertness towards OER. Thus, the aqueous cells based on the PbO₂ cathode and the Pb metal anode could be charged to a high voltage of 2 V. 17,231 It should be mentioned that PbO₂ has two common crystal phases: the α -phase with the orthorhombic structure and the β -phase with the tetragonal structure; they display slightly different electrochemical and physical properties. ^{232,233} Specifically, the α -PbO₂ phase possesses lower electrical conductivity but higher OER overpotential and a more compact deposition morphology than the β -PbO₂, thus leading to better cyclic stability. Besides, it was reported that doping PbO₂ with elements such as Bi²³⁴ and F^{235,236} can enhance its OER overpotential via influencing the surface binding energy with OER intermediates. Notwithstanding the attractive advantages of PbO₂, *e.g.*, high electrical, good chemical stability, and high OER overpotential 231,232 , its toxicity limits future development.

Manganese oxides are another critical group of cathode materials for high–voltage aqueous batteries. They are abundant and environmentally benign. ^{237,238} Moreover, manganese bears rich stable valence states (+2, +3, +4, +7), thus occurring as different manganese oxides, including Mn^{II}O, Mn^{III}₂O₃, Mn^{IV}O₂, Mn^{II}Mn^{III}₂O₄ (Mn₃O₄), and Mn^{II}₂Mn^{IV}₃O₈ (Mn₅O₈). As discussed in Section 3.2, the OER activities of manganese oxides relate to their d–band structures, which differ between the valence states. In brief, Mn³⁺ exhibits a higher electrocatalytic activity towards water oxidation than other valence states. ^{85,239,240} For instance, α –Mn₂O₃ presents an orthorhombic crystal structure with Mn³⁺ octahedrally coordinated by oxygen atoms; α –Mn₃O₄ exhibits a tetragonal symmetry and a distorted spinel structure with the Mn³⁺ ions located in the octahedral sites, both of which are known OER-active. ²³⁹ Besides, introducing defects, *i.e.*, oxygen vacancy, into the MnO₂ crystal structure produces Mn³⁺; consequently, the MnO₂ will transition from being OER–inert to OER–active. ^{85,241} Meanwhile, defect engineering is also considered to optimize the ionic conductivity of manganese oxide for better rate performances. ²⁴²

Among the manganese oxides, $MnO_2^{187,243}$ and $Mn_5O_8^{12}$ have presented encouraging OER-suppression performances. Specifically, pseudocapacitive MnO_2 is broadly utilized as the cathode in aqueous supercapacitors and could work in a wide range of 0.245-1.245 V (vs. SHE) in the neutral Na_2SO_4 electrolytes without conspicuous O_2 evolution reported. The relatively wide operation window is partially correlated to the spontaneous disproportionation of unstable Mn^{3+} into stable Mn^{2+} and Mn^{4+} under the neutral conditions.

It was reported that the diluted Na_2SO_4 aqueous electrolytes can stably work at a high voltage of 2.6 V at the scan rate of 10 mV s⁻¹ in the MnO_2 -based cells. ¹⁸⁷ In regards to Mn_5O_8 , a layer of hydroxyl groups forms on the surface of the electrode during cycling (Figure 21a). According to the DFT calculations, the surface hydroxyl groups are effective in retarding the OER through altering the adsorption energies of the intermediates (Figure 21b). ¹² The material exhibits an exceptionally high OER overpotential of 0.63 V at a low scan rate of 1 mV s⁻¹ in the Na_2SO_4 aqueous electrolytes.

An interesting phenomenon, as briefly mentioned in Section 4.2.1.1, is that the cell consisting of Mn_5O_8 as both electrodes suffers severe electrolyte decomposition and capacity decay at relatively low cycling rates e.g., 0.5 A g^{-1} . In comparison, another cell delivers improved cyclic stability at high rates, e.g., 5 A g^{-1} . Caution must be taken to pan out the conclusion that high-rate reactions suppress OER. It is possible that the seemingly tempered OER is due to the predominant occupation of active sites of the electrode by the charge carriers of the charge storage process, thus suppressing the OER and improving the cycling stability. Alternatively, the improved cycle life can be simply due to the fact that a high-rate dwarfs OER kinetics. It is, thus, critical for researchers to highlight how many days during which the cycling life was recorded. If the scale of HER or OER is time dependent, tests at a high current rate with "mitigated" OER or HER are performative and, thus, illegitimate to suggest that OER or HER is really suppressed.

A unique example is Mn_3O_4 . Ideally, it should exhibit high OER activity due to the valence states of 3+ for 2/3 of the manganese; however, it presents a wide potential range (0.2 – 1.4 V vs. SHE) at the scan rate of 2 mV s⁻¹. Specifically, after the initial cycles, the rGO@Mn₃O₄ electrode undergoes a positive shift of the OER onset potential from 1.1 V to over 1.4 V vs. SHE (Figure 21c). The phenomenon relates to the new redox peak at ~1.0 V, corresponding to the redox reaction of $Mn^{4+} \rightarrow Mn^{7+}$; it appears near the OER onset potential of the first cycle, which kinetically overwhelms the OER process for electrons, thus increasing the OER overpotential. However, it is not known that if the above kinetic abating of OER due to better kinetics of redox reactions of charge storage is applicable during the idling of batteries at open circuit voltage (OCV). Unfortunately, cycling reported in academic papers typically does not have resting interludes at OCV, where charge storage mechanism is completely shut off.

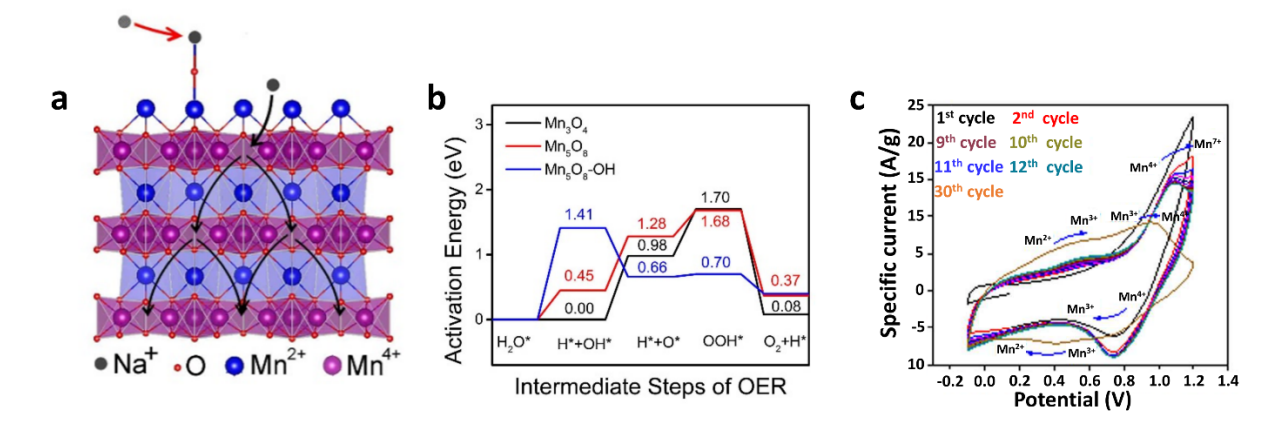


Figure 21. a) Schematic illustration of the hydroxylated Mn₅O₈ crystal structure with the hydroxylated interphase (-OH) marked by the red arrow. Reproduced with permission from ref 12. Copyright 2016 Springer Nature. b) Activation energies from electrode materials to intermediates and final products in the OER process for the (100) surface of surface hydroxylated Mn₅O₈ (Mn₅O₈-OH), Mn₅O₈, and (101) surface of Mn₃O₄. Reproduced with permission from ref 12. Copyright 2016 Springer Nature. c) CV curves of the rGO@Mn₃O₄ composite in the neutral 1.0 M Na₂SO₄. Reproduced with permission from ref 191. Copyright 2018 American Chemical Society.

(2) Metal Organic Frameworks

MOF materials do not receive much attention in the field, and related reports are limited. MOFs, particularly the metal hexacyanoferrates (MeHCF), present considerable OER overpotentials and are broadly applied in the aqueous batteries. Generally, MeHCF materials are of the face–centered cubic structures with the format of $A_xM[Fe(CN)_6]_y$, where A stands for the guest ion charges (*i.e.*, H^+ , Na^+ , K^+ , NH_4^+) and M stands for a transition metal (*e.g.*, Cu, Fe, V, Co, Mn) that is coordinated by nitrogen. In some structures, Fe is replaced by another metal, M'. The $M'(CN)_6$ and $M(NC)_6$ octahedra are spliced via the CN ligands in a linear structure with repeated units of -NC-Fe-CN-M-NC-, and the cavities in the framework are the sites for hosting the guest charges and lattice water molecules (Figure 22).

One critical advantage of the group of materials is the tunable sizes of the interstitial sites to accommodate charges of different sizes. And more importantly, some of them, e.g., $Na_2CoFe(CN)_6^{248}$, $Na_{0.6}Fe_2(CN)_6^{253}$, present excellent OER inertness and high upper potential limits. For instance, $Na_2CoFe(CN)_6$ cathode, as synthesized by a conventional co–precipitation method, exhibits stable CV curves with two pairs of redox peaks when cycled between 0.2 - 1.3 V vs. SHE with a scan rate of 0.1 mV s⁻¹ in the 1.0 M Na_2SO_4 electrolyte. No water electrolysis peaks appear near the upper cutoff potential of 1.3 V at an exacting scan rate of 0.1 mV s⁻¹, indicating a high OER overpotential of at least 0.5 V.

The OER inertness of these MOFs is yet to be well theorized. Some works reveal the strong impacts of crystallinity and structural defects such as Fe(CN)₆ and CN⁻ vacancies on the OER performance. Specifically, increasing the amounts of Fe(CN)₆ vacancies would deteriorate the spatial structures. Besides, it brings more water molecules into the interstitial sites; correspondingly, the content of A⁺ will decrease for balancing the charges, thus jeopardizing the charging capacity in the first cycles. ^{244,254-256} The defective sites may promote side reactions such as OER. Thus, the reduced crystallinity and increased CN vacancies are reported to directly aggravate the parasitic OER by supporting the formation of an oxy(hydroxide) active layer on the electrode surface. ^{257,258} Improving the crystallinity of MeHCF is an effective way to remove the defects, thus promoting a wide operation potential range in aqueous electrolytes. ^{246,257,258}

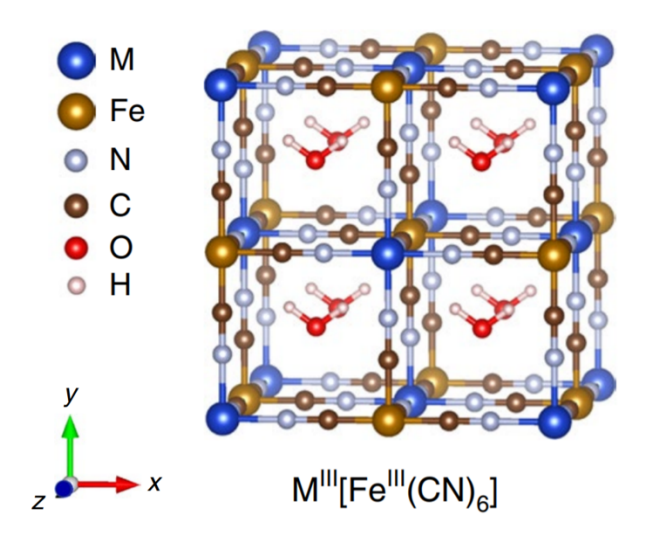


Figure 22. Schematic crystal structure of a Prussian blue analogue $M^{III}[Fe^{III}(CN)_6] \cdot 2H_2O$. Reproduced with permission from ref 252. Copyright 2019 Springer Nature.

(3) Heteroatom-Doped Manganese Oxide

In aqueous batteries, pre–insertion of alkaline metal ions, e.g., Li^+ , Na^+ , and K^+ , into MnO_2 crystal structure can stabilize the crystal structure, increase the capacity, and promote the cation rapid diffusion. Importantly, the doping is a facile way to enhance manganese oxide's overpotential towards OER. Before alkaline metal ion insertion, pristine MnO_2 cathode typically induces oxygen evolution at approximately 1.2 V vs. SHE in neutral electrolytes, which is measured through CV with a sweeping rate of 5 mV s⁻¹. SHE in neutral electrolytes, which is such as K_xMnO_2 or Na_xMnO_2 could withstand the upper cutoff potential of over 1.4 V vs. SHE. The specific mechanisms will be introduced in the following parts.

The K⁺-inserted α -MnO₂, *i.e.*, K_xMnO₂, exhibits a positive shift of the OER onset potential, observed when increasing the upper cutoff potential from 1 V to 1.2 V (Figure 23a). The enhancement relates to an additional redox reaction between 1 and 1.2 V in the CV curve that nears the OER onset potential. This anodic peak competes against the OER process for electrons, thus increasing the OER polarization and elevating the cutoff potential. However, it remains a question whether this new redox peak can damp the kinetics of OER when the batteries are at the OCV state. The appearance of the new anodic peak is closely correlated to the K⁺ pre-insertion, considering its absence in the CV curves of the pristine α -MnO₂ (Figure 23b). Furthermore, the origin of the additional redox reaction is investigated. The XPS tests show two facts: (1) when both materials are discharged to 0 V, the Mn valence states in K_xMnO₂ and α -MnO₂ are 3.0 and 3.7, respectively, (2) K_xMnO₂ can uptake more Na⁺ than α -MnO₂. Accordingly, a general mechanism is proposed that the pre-insertion of K⁺ ions activate the active sites inside the 2×2 tunnels of α -MnO₂. Consequently, the dominant reaction mechanism is converted from the surface electrical double-layer capacitance to pseudo-capacitance, thus producing the new peak in the CV curves (Figure 23c).

Birnessite–type $Na_{0.5}MnO_2$ with the layered structure was synthesized via the electrochemical oxidization of Mn_3O_4 . Similar to the K_xMnO_2 , an extra redox peak appears at 0.96 V in the cathodic scan, corresponding to the redox couple of Mn^{4+}/Mn^{3+} . The electron deficiency promotes the polarization of the OER process, thus elevating its onset potential from 1.25 V for pristine MnO_2 to 1.55 V. And CV results reveal that the material could reversibly work in a wide window of 0.25 – 1.55 V vs. SHE at a scan rate of 50 mV s⁻¹ without oxygen evolution in the 1.0 M Na_2SO_4 solution. Another fact that should be mentioned is that the disordered structure (low crystallinity) of the Na_xMnO_2 resulted from rich pre-inserted Na^+ does not have a great impact on the OER performances, differing from what we have discussed in the HER cases. I^{192}

A unique example is the $Ni_{0.25}Mn_{0.75}O$ solid solution electrode. When it is cycled in LiCl aqueous electrolytes between 0.245-1.645 V vs. SHE, serious O_2 evolution is detected in the initial cycles. In the following cycles, the OER intensity decays rapidly; concurrently, the pristine electrode undergoes the phase transformation from the crystalline $Ni_{0.25}Mn_{0.75}O$ to the amorphous $LiNi_{0.5}Mn_{1.5}O_4$. Consequently, the cathode could stably and reversibly work in the wide potential window from 0.245 V to 1.645 V vs. SHE at a scan rate of 5 mV s⁻¹. The mechanism behind the phenomenon has yet to be investigated.

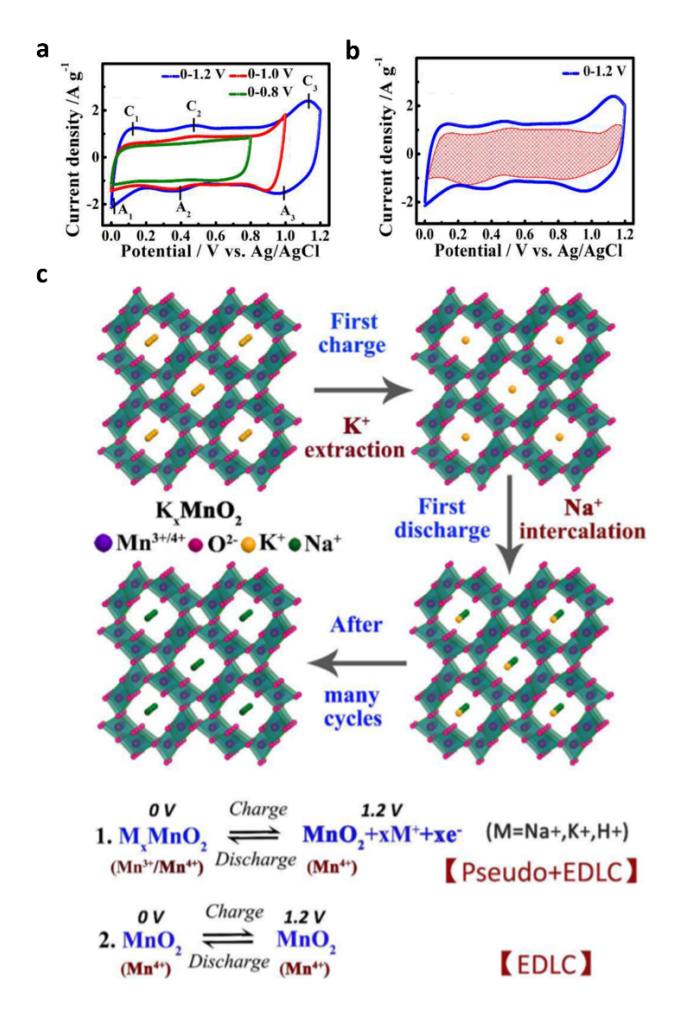


Figure 23. CV curves of a) K_xMnO_2 electrode and b) α -MnO₂ electrode in various potential windows at 5 mV s⁻¹. c) Illustration of storage mechanisms before and after K^+ pre-insertion. Reproduced with permission from ref 259. Copyright 2016 American Chemical Society.

4.3.2 Reduction of Active Sites:

As mentioned above, the charge storage reaction competing against the water electrolysis process may predominantly occupy the active sites on the electrodes, thus increasing the water electrolysis polarization. This strategy can inhibit water electrolysis during the charging process but may not be effective when the battery idles. Alternatively, the active sites towards water electrolysis can be blocked. One can use electrolysis inhibitors that are adsorbed over the active sites on electrodes or coat on electrodes the electrical insulating but ionic conductive solid-state interphases.

4.3.2.1 Electrolysis Inhibitors on Electrodes:

(1) HER Inhibitors on Anodes:

Some HER inhibitors on electrode surface can serve to reduce electroactive sites/areas, similar to the capping agents in the controlled syntheses of low-dimension nanomaterials, *i.e.*, quantum dots and nanofibers. The HER inhibitors need to be thermally, chemically, and electrochemically stable under battery working conditions and are strongly adsorbed over the electroactive sites to inhibit the water's electrolysis and the corrosion of the electrodes.¹⁷ There are generally two types of HER inhibitors in aqueous electrolytes: (1) organic ones and (2) inorganic ones.

Regarding the organic inhibitors, electrolyte additives, including derivatives of benzaldehyde $^{132,265-267}$ and benzene 268 were studied, showing HER hindrance performance in lead-acid batteries. For instance, adding 10^{-4} mol L⁻¹ 2–methoxybenzaldehyde into the 4.5 M H₂SO₄ aqueous electrolyte downshifts the HER onset potential of the Pb–Sb alloy anode from –0.574 V to –0.674 V vs. SHE, where the onset current density is set as 0.1 mA cm⁻² (Figure 24a). ²⁶⁷ The passivation effect relates to the interference of charges uptake through blocking the HER active sites; this can be rationalized by decreasing the double–layer capacitance to suppress water splitting. ^{269,270}

On the other hand, heed needs to be paid to the interactions between the additives and the electrode surface. In one model proposed, during the operation (discharge) of lead-acid battery, the Pb surface of the Pb–Sb alloy anode is positively charged, which prefers to absorb $SO_4^{2^-}$; the Sb surface is negatively charged, thus being preferentially covered by H^+ . The disparity is due to the PZC of Pb being lower than that of Sb by 500 mV. The higher oxidation potential of Sb inhibits the hydrogen evolution on its surface. Furthermore, the additives with moderate passivation degrees such as vanillin¹³² and 2–hydrorqbenzaldehyde²⁶⁸ exhibit high selectivity to passivate the Sb-exposed surface (Figure 24b). In comparison, the strong passivation additives, *e.g.*, p–propoxy acetophenone, 2–methoxybenzaldehyde, occupy both Pb and Sb surfaces, thus interfering with the regular charges intake on Pb surfaces (Figure 24c). The passivation degree relates to the functional groups such as –CHO, –COCH₃ or –COOH, –OCH₃, –OH, and –OC₃H₇ and their binding energies with the electrode surface. In addition, the concentration of additives is a critical parameter to consider. It is reported that the addition of vanillin impedes the reaction kinetics of the charge storage process when its concentration exceeds 5×10^{-4} mol L^{-1} , as indicated by the large voltage hysteresis. The passivation of the surface of the large voltage hysteresis.

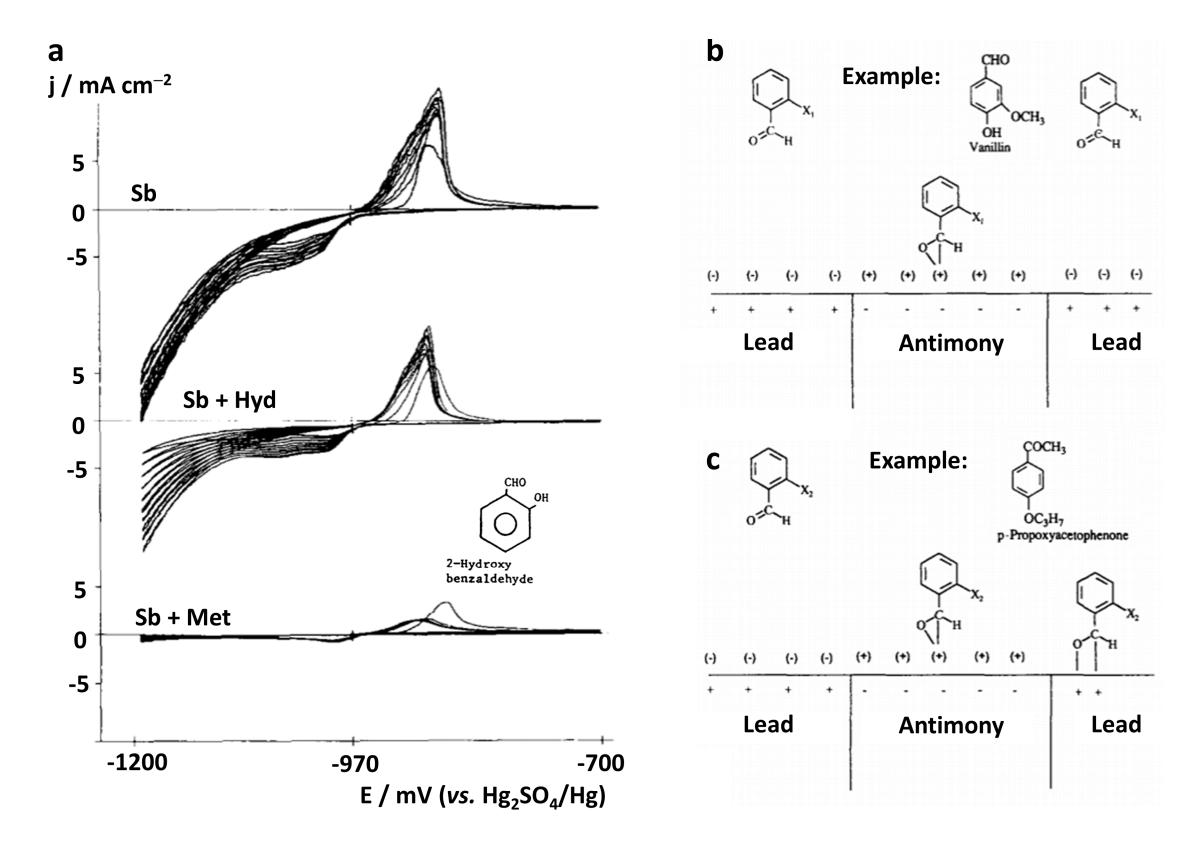


Figure 24. a) CV curves for a Pb-Sb alloy electrode in electrolytes with and without benzaldehyde additives (inset is the structure of 2-Hydroxy benzaldehydes). Reproduced with permission from ref 267. Copyright 1990 Elsevier. Schematic model of the adsorption of differently substituted benzaldehydes at the anode with b) moderate passivation effect and c) strong passivation effect. Reproduced with permission from ref 132. Copyright 1995 Elsevier.

In addition, sodium dodecyl sulfate (SDS) was reported as a electrolysis inhibitor to expand the operation window of aqueous Na/Zn-hybrid ion batteries. ¹⁴ Interestingly, with 0.8×10^{-3} mol L⁻¹ SDS in the electrolytes, the onset potential of HER and OER over the Ti grid current collector are respectively shifted to -1.15 V and 1.4 V vs. SHE at the scan rate of 10 mV s⁻¹, thus enabling a wide operation window of 2.5 V. The results demonstrate the feasibility of the SDS additive on HER/OER inhibition.

Another electrolysis inhibitor—alkanethiols—is reported to protect the Fe metal anode from HER. Note that the thermodynamic redox potential of the Fe(OH)₂/Fe couple is -0.808 V vs. SHE, whereas at pH 14, HER takes place at -0.826 vs. SHE; thus, the iron electrode, when idling, is thermodynamically stable in a strong alkaline solution. However, the charging process to form iron demands an overpotential, which could drag the potential of the iron electrode below that of HER. As shown in Figure 25a, a uniform monolayer of alkanethiols is grown on the Fe metal surface,²⁷¹ where the hydrophobic nature of the coating not only prevents the Fe metal electrode from contacting water but also depopulates the active sites on the electrode surface, thus

enhancing the HER overpotential. Of note, the HER-suppression performance of the surfactant relates to its chain formula; a maximum 90% reduction of HER rate is achieved at a chain length of six. Besides, the compactness of the coating also has strong impacts on cell performance; more compactness of the surfactant results in a higher charge resistance (Figure 25b) and a lower double–layer capacitance (Figure 25c).

The representative inorganic additives are the metal sulfides, which can be added into electrolytes (e.g., K_2S , Na_2S) or electrodes (e.g., FeS, PbS, Bi_2S_3). Several works validated that the additives allow the Fe metal anode to be deeply charged to -1.1 V vs. SHE without the occurrence of HER at a CV sweeping rate of 0.5 mV s^{-1} . The possible mechanism is that the dissolved S^{2-} that is chemisorbed over the electrode surface delays the Tafel reaction of H_2 formation due to the enhanced overpotential. Besides, S^{2-} is also suspected of entering the Fe(OH)₂ lattice, affecting the material's morphology and shortening the ion diffusion path, which benefits the reaction kinetics of the energy storage process. 156,272

lons can serve as additives to inhibit HER. For example, when adding 4.0 M LiCl into 2.0 M ZnSO₄-polyacrylamide hydrogels, the formed electrolytes (ZL-PMMa) could effectively reduce the corrosion and hydrogen evolution on Zn metal anode relative to that of pure 2.0 M ZnSO₄-polyacrylamide hydrogels (Z-PMMa). The improvements are correlated to the Li⁺-rich double layer interface formed on the anode during the charging process (Figure 25d). Besides, the presence of Li⁺ adsorption layer results in the transition of Zn deposition morphology from random nano-disks to oriented hexagonal rods, which may also account for improved corrosion-resistance (Figure 25e, f).

In fact, the additives that work via the physical- or chemical- adsorption mechanism have been well-studied in the corrosion field to protect the metals in aqueous environments. However, this approach has yet to receive much attention from the battery community. Hence, the knowledge of corrosion protection can be good references for selecting appropriate additives for high-voltage aqueous batteries.

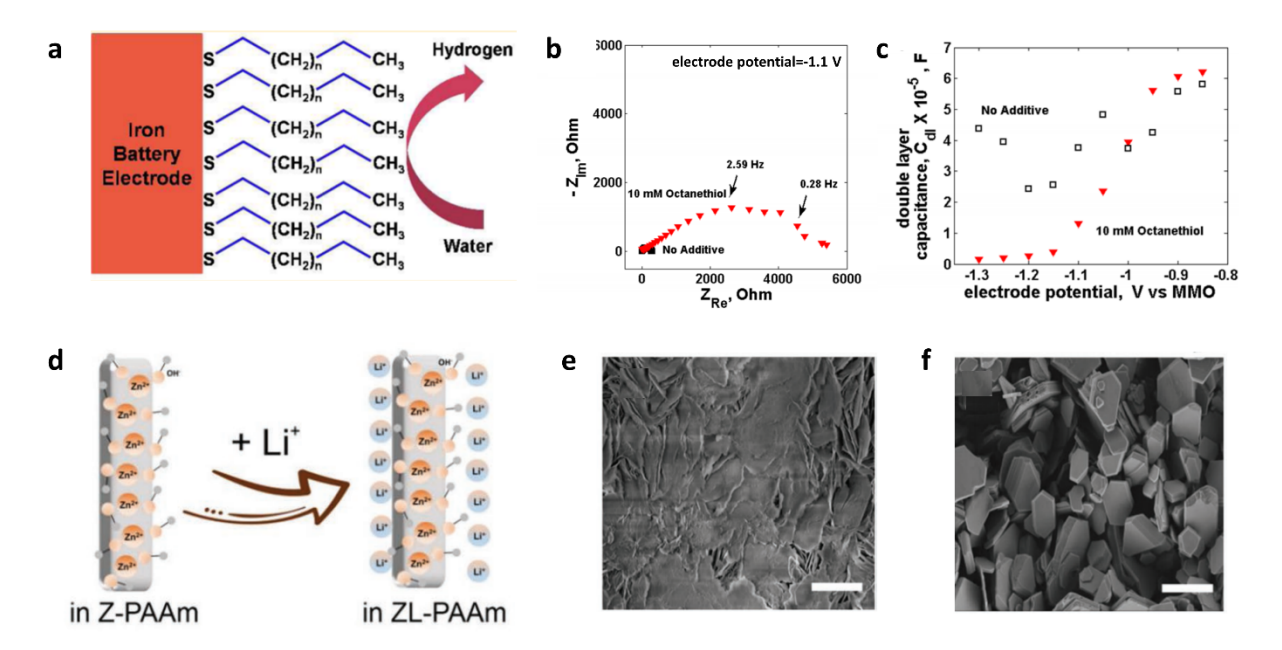


Figure 25. a) Schematic illustration of the HER passivation effect from the self-assembled monolayer of n-alkanethiols on the iron metal anode. b) Impedance results of the iron disk electrode at -1.1 V vs. SHE in 1.0 M potassium hydroxide with and without 10 mM octanethiol. c) Double-layer capacitance variance of the iron disk electrode in the electrolyte with or without 10 mM octanethiol at different electrode potentials. Reproduced with permission from ref 271. Copyright 2013 American Chemical Society. d) Schematic illustrating the interfacial differences in Z-PAAm and ZL-PAAm. SEM images of e) the Zn foil cycled in Z-PAAm and f) ZL-PAAm with the scale bar of 4 μm. Reproduced with permission from ref 274. Copyright 2020 Wiley-VCH.

(2) OER Inhibitors on Cathodes:

Similar with the anode's side pertaining to HER, the inhibitors on the cathode side are also demanded to be thermally, chemically, and electrochemically stable under the working conditions. More importantly, the inhibitors can be adsorbed over the active sites of electrode and are OER-inert. Generally, the inhibitors can be classified into inorganic ones and organic ones.

There are several examples of inorganic inhibitors. In lead–acid batteries, OER over the PbO $_2$ electrode can be ameliorated by adding H_3PO_4 into electrolytes, where H_3PO_4 is strongly adsorbed over the active sites, which increases the OER overpotential. Besides, sodium metaborate (NaBO $_2$) is feasible to inhibit the O_2 evolution over the Ni(OH) $_2$ electrode at high working temperatures. Furthermore, the addition of the metaborate ions reduces the resistance of charge transfer in the electrolytes, thus promoting the reaction kinetics of the energy storage process. Consequently, with the NaBO $_2$ additive, the cycling efficiency is enhanced to over 96% at 70 °C at the current rate of 1 C, while the efficiency is 92% in the plain electrolytes.

As for the reported organic inhibitors, the examples are disodium propane–1,3–disulfonate (PDSS)²⁸¹ and sodium dodecyl sulfate (SDS)¹⁴. PDSS uplifted the OER onset potential of the electrolyte (0.5 M LiNO₃ in a phosphate buffer (pH=7)) to over 1.8 V vs. SHE; the high anodic stability could even withstand high-potential cathodes such as LiNi_{0.5}Mn_{1.5}O₄ with two charging peaks at 1.69 V and 1.72 V vs. SHE, separately.²⁸¹ It is demonstrated that the PDSS anions serve as the physical barrier on the electrolyte/electrode interface to prevent the electrode from contacting water molecules. Similarly, the addition of SDS realizes the stable operation of another high–voltage material, Na₂MnFe(CN)₆, in the 1.0 M Na₂SO₄ + 1.0 M ZnSO₄ electrolyte.¹⁴ With the SDS additive in electrolytes, the OER onset potential is increased from 1.1 V to 1.4 V vs. SHE, high enough to include the two redox pairs of the electrode at 0.7 V and 1.1 V vs. SHE, respectively. DFT calculations validate that the SDS film blocks the transference of water molecules through its hydrophobic body.

4.3.2.2 Artificial Solid-State Interphases on Electrodes:

(1) Artificial SEI Layers on Anodes:

Forming an SEI layer or a solid-state electrolyte layer over anode can kinetically palliate HER. The interphase should be both a superior ionic conductor and an electrical insulator.¹³ Besides, the interphase ought to uniformly cover the electrode surface and be stable, *i.e.*, thermally, chemically, and mechanically, under the operating conditions. As discussed above, during charging, the solvated cations would be adsorbed over the negatively charged anode and confined in the Helmholtz double layer. Generally, it is the solvating water molecules that will receive electrons from the anode. Therefore, unlike the non-aqueous batteries, where via the decomposition of the organic solvent, the SEI layer forms *in situ* below certain potentials (corresponding to LUMO of the solvent), the solvent reduction product of aqueous electrolytes is H₂ gas, not contributing to the SEI formation but damaging the surface films if there are any.

The first solution is to tailor the solvation structure of cations, aiming at replacing H_2O molecules with other SEI-producing substances. As mentioned in Section 4.2, co-solvents with high Guttman donor numbers could replace water to enter the cation's solvation shell and get reduced prior to water molecules. Adding 20 wt.% DMSO into a 1.3 m aqueous $ZnCl_2$ electrolyte is demonstrated applicable to produce an SEI enriched with $Zn_{12}(SO_4)_3Cl_3(OH)_{15}\cdot SH_2O$, $ZnSO_3$, and ZnS, thus suppressing the HER on the zinc metal anode. In another case, adding tetraethylene glycol dimethyl ether (TEGDME) into the LiTFSI-based WiSE could facilitate the entering of the ether co-solvent into the Li^+ primary solvation shell as well. MD calculations and XPS further support the preference of the reduction of both TFSI anion and the ether co-solvent to form a SEI layer enriched with LiF and carbonaceous species. As a result, the "ether-in-water" electrolyte presents an exceptionally wide electrochemical stability window of 4.2 V, supporting the stable running of a 2.5 V $LiMn_2O_4 \mid Li_4Ti_5O_{12}$ full cell.

Salt concentrations in electrolytes greatly affect the chemical environment inside the electrolytes. In WiSE, the anions are expected to be in the closer vicinity to cations relative to the case of dilute electrolytes (Figure 2a₂). In addition, the properties of Helmholtz double layer are a function of the salt concentration inside the electrolytes. Specifically, the inner region of the double layer enriched with cations would be compressed at higher salt concentrations, thus pulling anions closer to the anode surface. This promotes the defluorination of anions such as BETI²⁸³, TFSI^{-7,106}, and CF₃SO₃⁻²⁸⁴⁻²⁸⁶ to form SEI on the anode surface. For instance, the LiF-rich SEI layer forms on the anode surface in the LiTFSI-based WiSE, which suppresses HER by physically blocking the exposure of water molecules. Unfortunately, the application of anion reduction to produce stable SEI has one potential limitation: at deeply low potentials, water molecules that are sensitive to the potential changes due to its large dipole moment and small size can be pulled near the electrode surface with hydrogen atoms of water pointed to the surface, where HER would jeopardize the SEI formation, accompanied by the low CE.^{3,31,287}

In WiSE, the dissolved gases may also involve in the formation of the SEI layer. ^{7,285} For instance, both Li_2CO_3 and Li_2O can be found in the SEI layer in the 21m LiTFSI electrolyte, which is proposed to originate from the reduction of CO_2 and O_2 gases dissolved in electrolytes, respectively (Figure 26a). It was rationalized that SEI may be formed in diluted aqueous electrolytes as well by consuming the dissolved gases, but therein they undergo rapid decay and dissolution after repeated cycling. The dissolved gases is a superior of the SEI layer. The second consuming the dissolved gases are consumed to the second consuming the dissolved gases.

Another solution is to introduce the artificial SEI or the solid-state electrolyte layer over the anode before cycling. For instance, a heterostructure anode is designed (Figure 256), where the Li metal is coated sequentially by an inner layer of a gel-polymer electrolyte (GPE) saturated with 1.0 M LiClO₄ in ethylene carbonate, diethyl carbonate, and dimethyl carbonate (1:1:1, V:V:V) and an outer layer of a LISICON film consisting of Li₂O-Al₂O₃-SiO₂-P₂O₅-TiO₂-GeO₂. ^{13,288} Therein, the GPE serves as the buffer layer to inhibit side reactions, and the LISICON film plays the role of preventing the permeation of protons, water, and hydrated ions. At the same time, both GPE (0.2 mS cm⁻²) and LISICON films (0.1 mS cm⁻²) possess superior Li⁺ conductivity, thus facilitating the reversible cycling of the composite electrode even at high rates. Consequently, the pioneering GPE coating allows the plating/stripping of the lithium electrode operating even at -3.04 V vs. SHE in 0.5 M Li₂SO₄ aqueous electrolytes, indicating the efficacious HER-suppression of the strategy. Furthermore, the cell composed of the composite anode and the LiMn₂O₄ cathode delivers a high output voltage over 4 V in the 0.5 M Li₂SO₄ aqueous electrolyte, a high CE close to 100%, and a high energy density up to 446 Wh Kg⁻¹ based on the mass of electrodes, which is even close to that of the commercial LIBs using the organic electrolytes. Later on, similar heterostructures were also applied in other anode materials with low redox potentials, e.g., graphite²⁸⁹ at 0.1 V vs. Li/Li⁺, Mg metal²⁹⁰ at -2.34 V vs. SHE.

Applying the artificial SEI layers, reversible plating/stripping behaviors of Mg and AI (-1.7 V vs. SHE) metals are reported in aqueous electrolytes. Specifically, the polymeric SEI layer for the Mg anode comprises thermal–cyclized polyacrylonitrile (cPAN with a molecular formula of $(C_3H_3N)_n$) and Mg trifluoromethanesulfonate (Mg(CF₃SO₃)₂) (Figure 26c), which helps extend the

full cell voltage to over 3.0 V. In the work for the Al anode, an ionic liquid (IL)–rich artificial SEI layer was formed on the pristine Al metal anode by immersing the electrode in the IL of $AlCl_3/[EMIm]Cl$ (1.3:1) for one day. Artificial SEI is capable of inhibiting HER for high–voltage aqueous batteries.

Artificial SEI layers have also been introduced over the Zn metal anode to prevent corrosion and the accompanied hydrogen evolution. ^{168-170,293} For instance, a polyamide (PA)-based artificial SEI is designed to protect the Zn metal anode. ¹⁶⁸ The PA coating suppresses the side reactions via two mechanisms (Figure 26d). Firstly, the interphase physically blocks the free water molecules from the bulk electrolyte. Secondly, the polar amide groups in the PA chains can interrupt the solvation sheaths of Zn^{2+} inside the interphase by forming hydrogen bonds with the water molecules. Then more dehydrated Zn^{2+} instead of the reactive $[Zn(OH_2)_6]^{2+}$ complexes would be involved in the plating reaction. Consequently, the corrosion resistance of the coated anode is significantly enhanced, which is supported by the positively shifted E_{corr} from -0.73 V to -0.72 V vs. SHE in linear polarization tests (Figure 26e) and the clean and smooth surface after 100 cycles of plating/stripping in the 2.0 M ZnSO₄ electrolyte.

Overall, the field of HER suppression by SEI is still at a rudimentary stage. For future development, more focus should be shifted to the selection of suitable additives in the electrolytes that assist the formation of efficacious SEI layers. Under aqueous environments, the resulting SEI needs to be more robust than the counterparts in aprotic batteries. It is, therefore, pivotal to study the durability of SEI, particularly the evolving HER kinetics at various SOC of batteries, including when the batteries are idling.

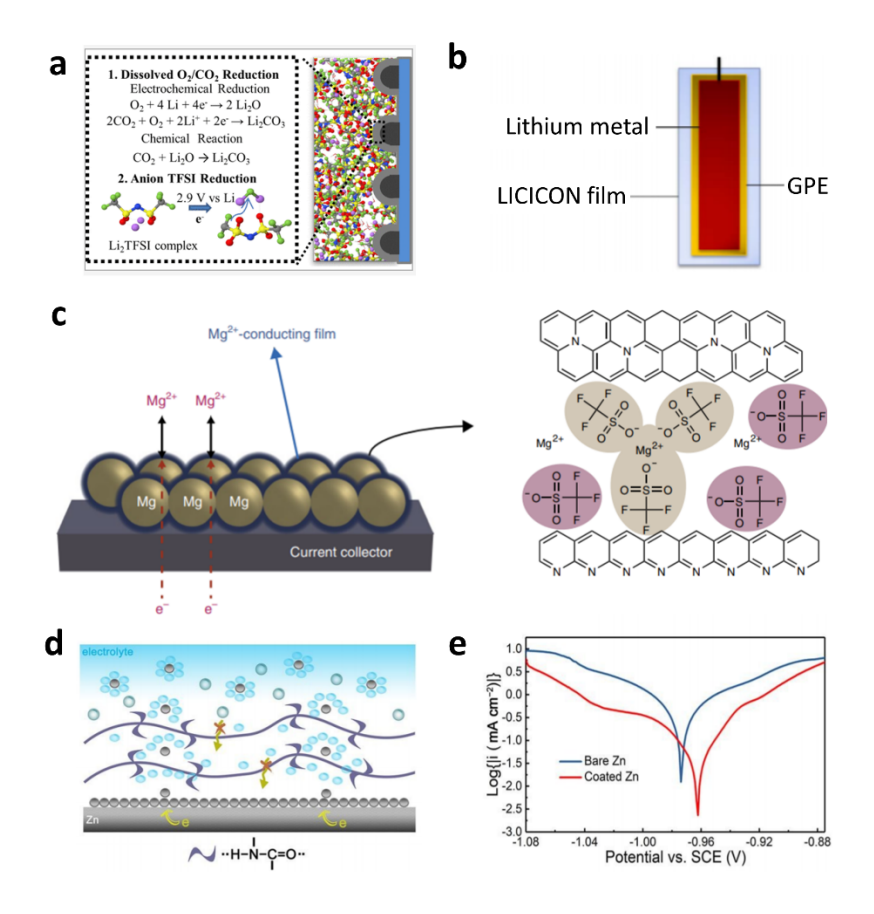


Figure 26. Schematic illustration of a) SEI formation mechanisms in WiSE (Reproduced with permission from ref 7. Copyright 2017 American Chemical Society.), b) A lithium metal anode coated by the artificial SEI layers of GPE and LISICON films (Reproduced with permission from ref 13. Copyright 2013 Springer Nature.), and c) the structure of Mg²⁺-conducting artificial SEI over the Mg powder electrode (Reproduced with permission from ref 291. Copyright 2018 Springer Nature.). d) Schematic diagrams for Zn deposition on the coated Zn, suggesting the role of PA layer in the inhibition of side reactions. e) Tafel plots showing the corrosion potentials of the bare Zn and the coated Zn. Reproduced with permission from ref 168. Copyright 2019 Royal Society of Chemistry.

(2) Artificial Cathode-Electrolyte Interphase Layer on Cathodes:

The cathode-electrolyte interphase (CEI) layer, a cathode version of SEI, needs to be electronically insulating and ionically conductive. Similar to the SEI formation on the anode, water electrolysis of the aqueous electrolytes cannot constitute a CEI layer on cathodes; hence the formation of CEI can only count on the additives and salts in the electrolytes.

For instance, the impact of a vinylene carbonate (VC) additive in the 1.0 M LiNO₃ aqueous electrolyte was studied, where the addition of 1 wt.% VC significantly improves the cyclic stability and CE for the Li_{1.05}Cr_{0.1}Mn_{1.85}O₄ cathode. ²⁹⁴ This is ascribed to the *in situ* formed polymeric

interphase on the electrode surface, which inhibits OER by blocking the water molecules. Additionally, an additive of tris(trimethylsilyl) borate (TMSB) can contribute to the formation of an effective CEI layer in concentrated electrolytes. The resulting amorphous interphase is formed through the oxidation of TMSB, as suggested by the peak at 1.6 V vs. SHE in the first CV cycle. The CEI helps improve the cycling stability and CE of a LiCoO_2 cathode by inhibiting OER and avoiding the dissolution of Co-ions. The full cell presents a high voltage of 2.5 V and an energy density of 120 Wh kg^{-1} based on the mass of electrodes. Furthermore, the theoretical calculations demonstrate that the thiophene with the highest occupied molecular orbital (HOMO) at -5.8 eV is potentially a good CEI-formation additive.

These reported strategies show a vast potential to protect high–potential cathode materials from triggering OER; however, meager attention has yet to be devoted to this area. It is expected that more additives will be identified to form effective CEI on cathodes. It is not a question that artificial CEI bears opportunities to realize the OER suppression for high–voltage aqueous batteries.

5. Challenges and Outlooks:

The solutions to address HER and OER can be thermodynamic or kinetics in nature. The thermodynamic solutions pertain to strengthening the O–H bonds inside the water solvent, managing the operation potentials of the electrodes, and decoupling the alkaline analytes and acidic catholytes through an ion-selective membrane. The kinetic solutions relate to enhancing the overpotentials for both the HER and OER processes.

Overall, the anticatalytic field for aqueous batteries is at its burgeoning stage; the further progress of the area demands out-the-the-box strategies, the practice of widely accepted standard protocols on the screening of electrode materials and electrolytes, and the rigorous, impartial data analysis. Here we offer our perspectives on these aspects.

5.1 Considerations to Tackle Water's Electrolysis:

5.1.1 About Thermodynamic Solutions:

Both HER and OER cripple aqueous batteries, causing self-discharge and compromised cycle life. Commercial aqueous batteries, including lead-acid batteries and NiMH batteries, have been grappling with these parasitic reactions ever since. The aqueous battery community should put these reactions at the crosshair to tackle, which should be prioritized over developing intricate electrode structures. Compared to OER, HER may potentially cause safety consequences of explosion. HER intrinsically exhibits higher activity than OER does because it requires half the number of electrons in the process. In addition, HER transpires at the potential higher than most desirable anode materials; in contrast, OER sits near the redox potentials of many cathode candidates. The four-electron process also bestows OER with an inherently higher overpotential. In addition, HER shortens the shelf-life of batteries by corroding the metal anode such as Zn.

Therefore, the field might consider prioritizing to address HER so that the next-generation aqueous batteries can enter the market sooner with an acceptable cycle life and a lack of safety concern. To the authors' knowledge, two routes are attractive from the thermodynamic point of view, which deserve more attention.

A promising path forward is to investigate the thermodynamic stability of water molecules themselves. We consider the thermodynamic solutions to take electrolysis as the most fundamental, which, once elucidated, will solve the problems without resorting to the kinetic ones. Despite being ubiquitous on this planet, our understanding of water still remains rudimentary. It is of significant fundamental values to investigate the relationships between the chemical environments and the resulting O-H bond strength of water molecules. The pertinent chemical environments are composed of the electrolytes as well as the surface of the electrodes. It is pivotal to point out that all electrochemical properties of water root in the seemingly simple covalent bonds inside this molecule. Guided by the knowledge of such correlations, it will be viable to identify or design the chemical environments that can promote the robustness of the O-H chemical bond and consequently transform the water molecules more inert. More inert water molecules will certainly better defend themselves facing the attacks of electrons or electron holes from the electrodes.

To understand the chemical environments of water molecules, a suite of interdisciplinary expertise needs to be mustered such as electrochemical experiments, advanced characterization, and computation, which is certainly non-trivial for a single research group. Collaborative research is indispensable. The chemical environments of electrolytes can be complicated, particularly those binary and ternary concentrated WiSE or DES. Importantly, in a convoluted system, the researchers need to find a salient descriptor property or properties of the system that is most sensitively correlated to water's bond strength.

In addition, partitioning the anode and cathode in basic anolyte and acidic catholyte, respectively, by ion-selective membranes as separators could expand the thermodynamic stability window of the electrolytes to over 2 V. Combining the acid-alkaline mixed electrolytes with the kinetics-pertinent water-stabilizing strategies mentioned above is expected to elevate the operation voltage of aqueous electrolytes to an even higher level. Besides, further research should be placed on developing ion-selective membrane with higher ionic conductivity and designing new cell structure to facilitate the practicality of the solution.

Another route is to uncover the thermodynamic properties of electrodes themselves in different environments. For example, the $[Zn(OH)_4]^2$ -/Zn and the $Zn^{2+}(aq)$ /Zn redox couple exhibit vastly different redox potentials. The ion speciation of the electrolytes and the concentrations of the ions have profound impacts on the redox potentials of the electrodes.

5.1.2 About Kinetic Solutions:

If water electrolysis is inevitable from a thermodynamic point of view. It is critical to retard such reactions as much as possible from a kinetic standpoint. As one direction, it is pivotal to further

beef up the volcano plots of HER and OER initiated by the catalysis field. The plots are woefully incomplete for the sake of designing aqueous batteries, where most electrode materials cannot be found on these plots. More studies are, therefore, needed to understand the interactions of the intermediates such as H* and HO* with some of the most promising electrode materials in aqueous batteries. Fundamental principles that reliably predict the inertness of electrodes in HER and OER should be elucidated. In this vein, extrapolation of the current trends revealed by the screening of electrocatalysts will be found valuable in identifying better electrode materials. Both empirical and theoretical studies, if conducted synergistically, will be able to push the envelope of the knowledge for the purposes of the anticatalytic effect of large overpotentials.

There has been a lack of basic understanding of active sites on most battery materials for HER and OER processes unraveled in basic steps. Such understanding will be essential to use the least amount of decoration substances on the electrode surface to passivate the electrode from attacks of aqueous species. To gain such understanding, one must zero in on the electrical double layers of the electrode at different SOC with the consideration of the PZC of the electrode materials. The chemical and electrostatic interactions between the electrode and the electrolyte will be one key to reveal what it takes to address the attacks of aqueous species. Another key is the understanding of the solvation structures of ions or, more precisely, the binding environment of water molecules. One must consider factors holistically, including the electrode surface, the orientation of water molecules, and the double-layer-sequestered ions, to understand the binding of aqueous species to the electrode surface.

If neither the thermodynamic solutions nor the surface binding engineering with aqueous species can effectively curtail the water electrolysis, one has to resort to physically blocking water molecules from coming ashore to the electrode surface. One needs an SEI, either *in situ* formed in an operating cell or during conditioning or artificially pre-formed before assembling the batteries. The conventional wisdom of SEI comes from the knowledge in Li-ion batteries, where solvent and salt conveniently decompose into a hermetic mosaic film over the surface of electrodes, which is ionically conductive but electronically insulating. It seems that fluorinated salts are still the most effective ingredient in forming efficacious SEI in aqueous electrolytes. The endeavors to identify the electrolyte formulae to form robust SEI have just gained traction. It can be expected that more interesting SEI-formation reactions will find their power to seal the electrodes. After all, reactions in aqueous electrolytes can be characterized more easily, and it is likely that the design of SEI for aqueous batteries will be ungraded faster than its counterparts in LIBs.

5.1.3 Insights from Other Areas:

Of note, HER and OER are also considered harmful in other fields using aqueous electrolytes such as metal deposition, electrosynthesis of organics by CO_2 reduction, electrochemical synthesis of ozone gas (O_3) , synthesis of hydrogen peroxide (H_2O_2) , and organic oxidation

for water pollution treatment³⁰⁰. In the fields, researchers have investigated interesting materials (*e.g.*, boron–doped diamond), additives (*e.g.*, choline chloride), and strategies (*e.g.*, hydrophobic polymer coating). Unfortunately, these studies have received little attention for the purposes the aqueous batteries. These works should be referenced to help the water stabilization in aqueous batteries.

Most importantly, much can be learned from the prowess of the corrosion field, where corrosion is often tantamount to HER, which can be essentially considered as an electroless reaction of a metal anode in aqueous metal batteries when resting at OCV or idling. It is our observation that it is high time for the aqueous battery field to scrutinize the results from the well-established corrosion-protection field carefully. The conventional corrosion inhibition methods, including alloying, 301-303 coating with high corrosion resistance, 304,305 applying the corrosion inhibitors 306-309, improving surface hydrophobicity 310,311 have rarely been employed to protect electrodes in aqueous batteries.

Of note, the corrosion protection in batteries is slightly different from that elsewhere. Firstly, the metal anode in batteries undergoes metal plating/stripping during charging and discharging, respectively, albeit there are resting interludes. Secondly, in batteries, the metal anode experiences dramatic morphology changes, *i.e.*, dissolved/reformed, that may negate the corrosion protection measures. For example, it will be a question whether the alloys will be reformed after a cycle of stripping and plating of the active mass, where the redox behavior of the insert element is critical to consider. On the other hand, the anti-corrosion mechanisms may impede the electrochemical reactions. For example, it is well known that the native surface film of MgO on Mg metal is corrosion resistant but also causes a large overpotential for the stripping reaction of Mg. Importantly, the electrode protection may come easier than the conventional prevention of corrosion. For instance, the electrolyte components in the battery field could be modified with a great leeway of flexibility while the environments are often fixed in conventional metal protection fields. Therefore, it is very likely that befitted electrolyte additives could be found to optimize the anti-corrosion behavior of metal anodes.

5.2 Characterization of Water Electrolysis on Electrodes:

LSV (Figure 27a) 312 and CV (Figure 27b) 220 can evaluate the electrochemical stability window of aqueous electrolytes. As discussed above, the HER/OER concentration overpotential is positively related to the scanning rate. For a fair comparison of electrolyte's thermodynamic stability, we suggest the community use a scanning rate below 0.5 mV s $^{-1}$ for LSV and CV measurements. Furthermore, Tafel plots can reveal the reaction kinetics of HER and OER (Figure 27c), which can be derived from the LSV curves. The higher slope for the Tafel plots, the more effective the battery electrode materials are in inhibiting HER and OER. It is worth pointing out that the scanning rates used to probe the onset potential of HER or OER should not be over 0.5 mV s $^{-1}$; otherwise, the stability of the electrolytes will be overestimated. Increasing temperature facilitates the reaction kinetics of the water electrolysis process according to the Arrhenius law ($k = Ae^{\frac{-E_a}{RT}}$), which narrows the stability window of water by increasing the dissociation constant

of water (K_w) and the activity of H^+ and OH^- . Therefore, testing conditions need to be considered when comparing electrode materials or electrolytes in their HER/OER behaviors. It is also important that the community starts to adopt a similar current density to mark the onset potential. The current density, *e.g.*, 0.05 mA cm⁻², needs to be considerably lower than those used for evaluating electrocatalysts.

Regarding the corrosion caused by HER, the oxidation potentials of the metal anodes and the HER rate could be estimated from the E_{corr} and I_{corr} in a linear polarization curve, respectively (Figure 27d). Specifically, I_{corr} can be calculated by the Stern–Geary equation (Equation 29). The Stern–Geary constant B can be further expressed as Equation 30, where the b_a and b_c can be obtained by the log I vs. E plots in both anodic and cathodic regions of the Tafel plots. The fitted value of R_p represents the overall resistance of the anode surface corrosion. The fitted value of R_p represents the overall resistance of the anode surface corrosion.

$$I_{corr} = \frac{B}{R_p}$$
 Equation 29

$$B = \frac{b_a b_c}{2.303(b_a + b_c)}$$
 Equation 30

Note that E_{corr} and R_p evolve as the function of immersion time, which should be considered, as shown in Figure 27e, f. 315,316,320

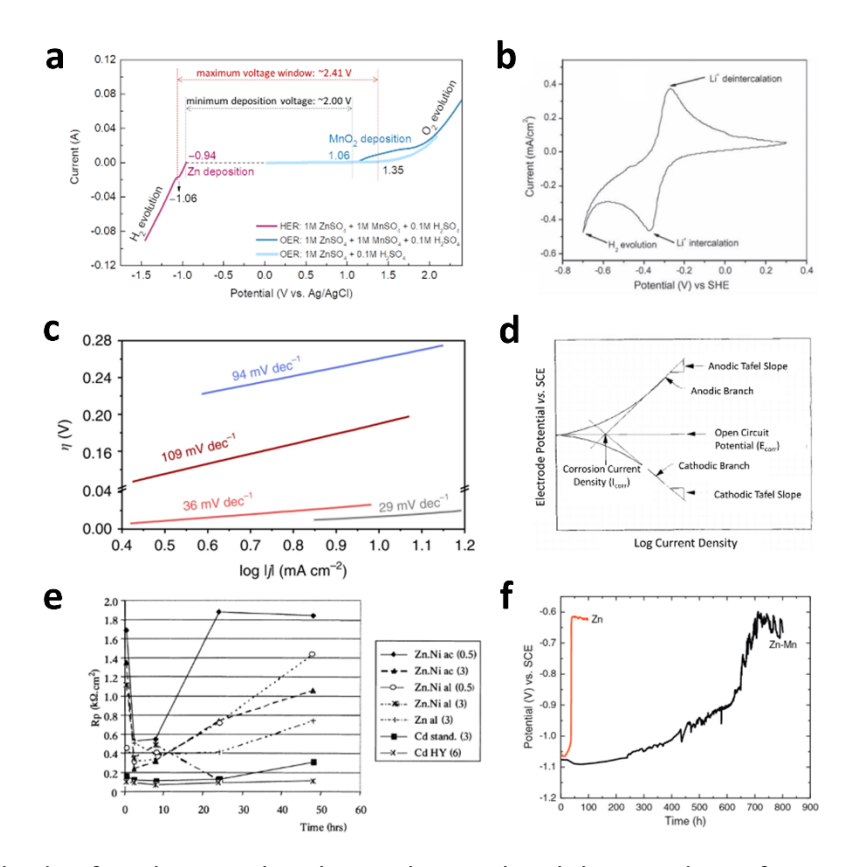


Figure 27. Methods of evaluating the electrochemical stability window of aqueous electrolytes, including a) LSV (Reproduced with permission from ref 312. Copyright 2019 Wiley-VCH.) and b) CV (Reproduced with permission from ref 220. Copyright 2007 Elsevier.). Methods on evaluating the reaction kinetics of water electrolysis, including c) Tafel plots (Reproduced with permission from ref 321. Copyright 2020 Springer Nature.) and d) Linear polarization curve (Reproduced with permission from ref 317. Copyright 1989 American Ceramic Society.). e) Evolution of the polarization resistance with the immersion time for various coatings including Zn–Ni alloy prepared in an acidic (ac) or alkaline (al) bath, pristine Zn metal prepared in alkaline bath, and Cd (standard or high yield). Reproduced with permission from ref 320. Copyright 2000 Elsevier. f) Evolution of E_{corr} as a function of time for Zn and Zn–Mn alloy. Reproduced with permission from ref 315. Copyright 2014 Elsevier.

In addition, precisely measuring the volume of the evolved gas will be invaluable to evaluate the performance of water electrolysis inhibition. Water-drainage method (Figure 28a) is widely used due to its high practicality and low cost. Specifically, the produced gas (e.g., O₂, H₂) will diffuse into a down-facing glass cylinder and expel the filled water out; the amount of gas can be measured.

Another common method is online electrochemical mass spectrometer (OEMS), where the evolved gas in electrolytes are constantly carried out to the mass spectrometer by Ar gas flow. ^{11,28} The method not only measures the total volume of evolved gas molecules but also *in situ* records

their concentration variance (Figure 28b). The regular testing cell is based on a three-electrode configuration. The cell could be placed in a five-neck beaker, with each neck corresponding to working electrode, reference electrode, counter electrode, gas outlet, and Ar gas inlet, respectively (Figure 28c).²⁸ Later, an upgraded testing cell was designed, which better resembles the lab-used coin cells, where the working electrode and counter electrode are separated by a separator soaked with limited electrolytes (dozens of microliters) (Figure 28d). Furthermore, to avoid the electrolyte evaporation brought by gas flowing, a blank cell (right with only electrolytes is set before the tested cell (left) to moist the Ar gas.

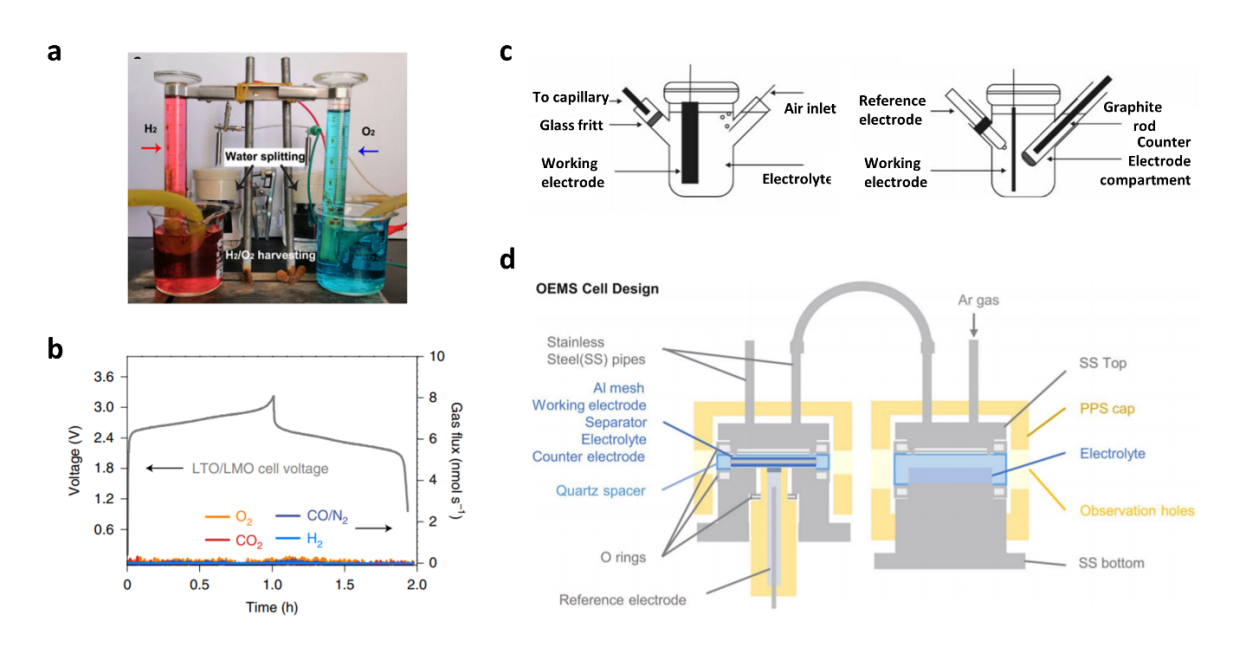


Figure 28. a) A gas collection device via the water drainage method. Reproduced with permission from ref ³²². Copyright 2019 Elsevier. b) OEMS results of the L-LTO/LMO full cell during the galvanostatic tests with the concentration variance of several gases (O₂, CO₂, CO/N₂, H₂). Reproduced with permission from ref 11. Copyright 2020 Springer Nature. Schematic illustration of the OEMS cells based on c) five-neck beakers (two side views are presented) (Reproduced with permission from ref 28. Copyright 2018 Royal Society of Chemistry.), and d) coin-cell structure designed by Lu *et al.* (Reproduced with permission from ref 11. Copyright 2020 Springer Nature.).

5.3 Theoretical Simulation Methods:

Theoretical simulation is a powerful tool in the study of aqueous batteries. Generally, they play the role of explaining phenomena in experiments, elucidating mechanisms at the microscopic scale, and even predicting the properties of materials. As mentioned above, MD and DFT are the most frequently used simulation methods, and they serve different functions.

MD simulation can describe the motion of particles, where information of molecular assemblies can be obtained by calculating the forces under different interaction potentials. For instance, solvation structures of ions or water's chemical environment in aqueous electrolytes on the atomic level could be unveiled by applying the classic MD (CMD) and *ab initio* MD (AIMD). Despite the minor differences in solvation compactness, the general structures simulated by the methods are basically the same. Besides, the AIMD could also simulate the decomposition of electrolytes and the initial formation of SEI/CEI over electrodes.

Based on the Born-Oppenheimer approximation to the Schrodinger equation, DFT becomes a convenient method to simulate properties of solid materials, particularly electronic structures. For example, DFT is widely applied to calculate the adsorption energy of HER/OER intermediates over electrodes, thus allowing researchers to construct the relationships between the reaction kinetics and electrodes' electronic structures. Also, DFT calculation could describe the electron/charge distribution in electrode materials, which helps reveal the active sites towards both charge storage and water electrolysis processes. In addition to the electrode materials in the solid phase, DFT can estimate the frontier orbitals (HOMO and LUMO) for electrolytes as well. Hence, several works integrated the DFT and MD to explain the role of water's chemical environment in its thermodynamic stability. Also, 11,109,117

Overall, the theoretical simulation is complementary to experimental studies to understand reaction mechanisms at an atom scale, which can shed light on the selection of electrodes and the optimization of electrolyte components. However, water electrolysis in the aqueous battery is complicated, engaging factors, thermodynamic and kinetic. It is expected that simulation will play a larger role in the future by considering more factors, which can better predict gas evolution reactions in the electrolytes.

5.4 Conclusions:

The battery field will witness a renaissance of the aqueous electrolytes, which are being scrutinized for the next—generation rechargeable batteries. Despite all merits, the future of aqueous batteries hinges on solutions for tackling HER and OER transpiring on anodes and cathodes, respectively. These solutions must effectively suppress these parasitic reactions to the extent that they do not cause a safety concern or significantly shorten the battery's longevity. The primary solutions toward the water electrolysis problems will enhance either the thermodynamic stability of the aqueous electrolytes or the kinetics-pertinent overpotentials of HER and OER. Correspondingly, the available strategies, e.g., salt-concentrated electrolytes and water electrolysis anticatalytic strategies, have shown the potential to promote aqueous batteries' performance. However, in the authors' opinion, the aqueous battery field should shift the focus from electrodes to the interface properties in the Helmholtz layer, e.g., solvation structures, defined by the interactions between electrolytes and electrodes. It seems that insights are available for addressing these ubiquitous reactions of HER and OER from other fields, where battery chemists will need to roam into other areas' literature for existing or new solutions. Besides, the characterization and evaluation of water electrolysis in batteries need to be devised with extra care, where the results from different studies

can be comparable. Meanwhile, theoretical simulation method (*e.g.*, MD, DFT) should be further advanced to assist the fundamental understanding for water electrolysis process and the precise prediction for cell's performances in practical situation. It is very likely that water electrolysis, the century-old problem, will be further understood and addressed in aqueous batteries in the near future.

Acknowledgements

X. Ji thanks U.S. National Science Foundation for the financial support with Awards CBET 2038381 and DMR 2004636.

Biographies

Yiming Sui received his B.Sc. degree in 2017 from the Northeastern University, China, and M.Sc. Degree in 2019 from the University of Washington, Seattle, USA. Currently, he is a Ph.D. student in Oregon State University in Prof. Xiulei Ji's lab. His research interests focus on batteries with new chemistries, such as dual-ion batteries and proton batteries.

Prof. Xiulei Ji is an Associate Professor of Chemistry at Oregon State University. He graduated from Jilin University with B.Sc. in Chemistry in 2003. He obtained his M.Sc. and Ph.D. in Materials Chemistry from the University of Waterloo in 2006 and 2009. He was an NSERC Postdoctoral Fellow at the University of California, Santa Barbara. He joined the Department of Chemistry at Oregon State University in 2012.

References

- (1) Mahmood, N.; Tang, T.; Hou, Y. Nanostructured Anode Materials for Lithium Ion Batteries: Progress, Challenge and Perspective. *Adv. Energy Mater.* **2016**, *6*, 1600374.
- (2) Liu, Z.; Huang, Y.; Huang, Y.; Yang, Q.; Li, X.; Huang, Z.; Zhi, C. Voltage Issue of Aqueous Rechargeable Metal-Ion Batteries. *Chem. Soc. Rev.* **2020**, *49*, 180-232.
- Yang, C.; Chen, J.; Qing, T.; Fan, X.; Sun, W.; von Cresce, A.; Ding, M. S.; Borodin, O.; Vatamanu, J.; Schroeder, M. A.et al. 4.0 V Aqueous Li-Ion Batteries. *Joule* **2017**, *1*, 122-132.
- (4) Rezaei, B.; Taki, M. Effects of Tetrabutylammonium Hydrogen Sulfate as an Electrolyte Additive on the Electrochemical Behavior of Lead Acid Battery. *J. Solid State Electrochem.* **2008**, *12*, 1663-1671.
- (5) Wan, F.; Zhu, J.; Huang, S.; Niu, Z. High-Voltage Electrolytes for Aqueous Energy Storage Devices. *Batter. Supercaps* **2020**, *3*, 323-330.
- (6) Chen, L.; Zhang, J.; Li, Q.; Vatamanu, J.; Ji, X.; Pollard, T. P.; Cui, C.; Hou, S.; Chen, J.; Yang, C.et al. A 63 m Superconcentrated Aqueous Electrolyte for High-Energy Li-Ion Batteries. *ACS Energy Lett.* **2020**, *5*, 968-974.
- (7) Suo, L.; Oh, D.; Lin, Y.; Zhuo, Z.; Borodin, O.; Gao, T.; Wang, F.; Kushima, A.; Wang, Z.; Kim, H.-C.et al. How Solid-Electrolyte Interphase Forms in Aqueous Electrolytes. *J. Am. Chem. Soc.* **2017**, *139*, 18670-18680.

- (8) Zhang, L.; Rodríguez-Pérez, I. A.; Jiang, H.; Zhang, C.; Leonard, D. P.; Guo, Q.; Wang, W.; Han, S.; Wang, L.; Ji, X. ZnCl₂ "Water-in-Salt" Electrolyte Transforms the Performance of Vanadium Oxide as a Zn Battery Cathode. Adv. Funct. Mater. 2019, 29, 1902653.
- (9) Wang, F.; Suo, L.; Liang, Y.; Yang, C.; Han, F.; Gao, T.; Sun, W.; Wang, C. Spinel LiNi_{0.5}Mn_{1.5}O₄ Cathode for High-Energy Aqueous Lithium-Ion Batteries. *Adv. Energy Mater.* **2017,** *7*, 1600922.
- (10) Suo, L.; Borodin, O.; Gao, T.; Olguin, M.; Ho, J.; Fan, X.; Luo, C.; Wang, C.; Xu, K. "Water-in-Salt" Electrolyte Enables High-Voltage Aqueous Lithium-Ion Chemistries. *Science* **2015**, *350*, 938-943.
- (11) Xie, J.; Liang, Z.; Lu, Y.-C. Molecular Crowding Electrolytes for High-Voltage Aqueous Batteries. *Nat. Mater.* **2020**, *19*, 1006-1011.
- (12) Shan, X.; Charles, D. S.; Lei, Y.; Qiao, R.; Wang, G.; Yang, W.; Feygenson, M.; Su, D.; Teng, X. Bivalence Mn₅O₈ with Hydroxylated Interphase for High-Voltage Aqueous Sodium-Ion Storage. *Nat. Commun.* **2016**, *7*, 13370.
- (13) Wang, X.; Hou, Y.; Zhu, Y.; Wu, Y.; Holze, R. An Aqueous Rechargeable Lithium Battery Using Coated Li Metal as Anode. *Sci. Rep.* **2013**, *3*, 1401.
- (14) Hou, Z.; Zhang, X.; Li, X.; Zhu, Y.; Liang, J.; Qian, Y. Surfactant Widens the Electrochemical Window of An Aqueous Electrolyte for Better Rechargeable Aqueous Sodium/Zinc Battery. *J. Mater. Chem. A* **2017**, *5*, 730-738.
- (15) Eftekhari, A. High-Energy Aqueous Lithium Batteries. Adv. Energy Mater. 2018, 8, 1801156.
- (16) Qianzhi Gou, S. Z., Jiacheng Wang, Meng Li, Junmin Xue. Recent Advances on Boosting the Cell Voltage of Aqueous Supercapacitors. *Nano-Micro Lett.* **2020**, *12*, 1-22.
- (17) Wang, F.; Hu, C.; Zhou, M.; Wang, K.; Lian, J.; Yan, J.; Cheng, S.; Jiang, K. Research Progresses of Cathodic Hydrogen Evolution in Advanced Lead–Acid Batteries. *Sci. Bull.* **2016**, *61*, 451-458.
- (18) Chao, D.; Qiao, S.-Z. Toward High-Voltage Aqueous Batteries: Super- or Low-Concentrated Electrolyte? *Joule* **2020**, *4*, 1846-1851.
- (19) Yuan, X.; Ma, F.; Zuo, L.; Wang, J.; Yu, N.; Chen, Y.; Zhu, Y.; Huang, Q.; Holze, R.; Wu, Y.et al. Latest Advances in High-Voltage and High-Energy-Density Aqueous Rechargeable Batteries. *Electrochem. Energy Rev.* **2021**, *4*, 1-34.
- (20) Chao, D.; Zhou, W.; Xie, F.; Ye, C.; Li, H.; Jaroniec, M.; Qiao, S.-Z. Roadmap for Advanced Aqueous Batteries: From Design of Materials to Applications. *Sci. Adv.* **2020**, *6*, eaba4098.
- (21) Edward, M. Introduction to Corrosion Science; Springer, New York, NY, 2010.
- (22) Viswanath, R. P. A Patent for Generation of Electrolytic Hydrogen by a Cost Effective and Cheaper Route. *Int. J. Hydrog. Energy* **2004**, *29*, 1191-1194.
- (23) Jiang, H.; Shin, W.; Ma, L.; Hong, J. J.; Wei, Z.; Liu, Y.; Zhang, S.; Wu, X.; Xu, Y.; Guo, Q.et al. A High-Rate Aqueous Proton Battery Delivering Power Below −78 °C via an Unfrozen Phosphoric Acid. Adv. Energy Mater. 2020, 10, 2000968.
- (24) Ulleberg, Ø. Modeling of Advanced Alkaline Electrolyzers: A System Simulation Approach. *Int. J. Hydrog. Energy* **2003**, *28*, 21-33.
- (25) Xiao, B. Intercalated Water in Aqueous Batteries. Carbon Energy 2020, 2, 251-264.
- (26) Cotton, F. A.; Wilkinson, G. Advanced Inorganic Chemistry; New York: Wiley, 1988.
- (27) Tomiyasu, H.; Shikata, H.; Takao, K.; Asanuma, N.; Taruta, S.; Park, Y.-Y. An Aqueous Electrolyte of the Widest Potential Window and Its Superior Capability for Capacitors. *Sci. Rep.* **2017,** *7*, 45048.
- (28) Dubouis, N.; Lemaire, P.; Mirvaux, B.; Salager, E.; Deschamps, M.; Grimaud, A. The Role of the Hydrogen Evolution Reaction in the Solid–Electrolyte Interphase Formation Mechanism for "Water-in-Salt" Electrolytes. *Energy Environ. Sci.* **2018**, *11*, 3491-3499.
- (29) Zhang, C.; Shin, W.; Zhu, L.; Chen, C.; Neuefeind, J. C.; Xu, Y.; Allec, S. I.; Liu, C.; Wei, Z.; Daniyar, A. The Electrolyte Comprising More Robust Water and Superhalides Transforms Zn-Metal Anode Reversibly and Dendrite-Free. *Carbon Energy* **2020**, DOI:10.1002/cey2.70.

- (30) Vyalikh, A.; Emmler, T.; Grünberg, B.; Xu, Y.; Shenderovich, I.; Findenegg, G.; Limbach, H.-H.; Buntkowsky, G. Hydrogen bonding of water confined in controlled-pore glass 10-75 studied by 1H-solid state NMR. *Z. Phys. Chem.* **2007**, *221*, 155-168.
- (31) Borodin, O.; Self, J.; Persson, K. A.; Wang, C.; Xu, K. Uncharted Waters: Super-Concentrated Electrolytes. *Joule* **2020**, *4*, 69-100.
- (32) Fic, K.; Lota, G.; Meller, M.; Frackowiak, E. Novel Insight into Neutral Medium as Electrolyte for High-Voltage Supercapacitors. *Energy Environ. Sci.* **2012**, *5*, 5842-5850.
- (33) Hindman, J. Nuclear Magnetic Resonance Effects in Aqueous Solutions of 1–1 Electrolytes. *J. Chem. Phys.* **1962**, *36*, 1000-1016.
- (34) Jiao, Y.; Zheng, Y.; Jaroniec, M.; Qiao, S. Z. Design of Electrocatalysts for Oxygen- and Hydrogen-Involving Energy Conversion Reactions. *Chem. Soc. Rev.* **2015**, *44*, 2060-2086.
- (35) Qu, Q.; Zhang, P.; Wang, B.; Chen, Y.; Tian, S.; Wu, Y.; Holze, R. Electrochemical Performance of MnO₂ Nanorods in Neutral Aqueous Electrolytes as a Cathode for Asymmetric Supercapacitors. *J. Phys. Chem. C* **2009**, *113*, 14020-14027.
- (36) Lu, F.; Zhou, M.; Zhou, Y.; Zeng, X. First-Row Transition Metal Based Catalysts for the Oxygen Evolution Reaction under Alkaline Conditions: Basic Principles and Recent Advances. *Small* **2017**, *13*, 1701931.
- (37) Suen, N.-T.; Hung, S.-F.; Quan, Q.; Zhang, N.; Xu, Y.-J.; Chen, H. M. Electrocatalysis for the Oxygen Evolution Reaction: Recent Development and Future Perspectives. *Chem. Soc. Rev.* **2017**, *46*, 337-365.
- (38) Fang, M.; Dong, G.; Wei, R.; Ho, J. C. Hierarchical Nanostructures: Design for Sustainable Water Splitting. *Adv. Energy Mater.* **2017**, *7*, 1700559.
- (39) Morales-Guio, C. G.; Stern, L.-A.; Hu, X. Nanostructured Hydrotreating Catalysts for Electrochemical Hydrogen Evolution. *Chem. Soc. Rev.* **2014**, *43*, 6555-6569.
- (40) Dau, H.; Limberg, C.; Reier, T.; Risch, M.; Roggan, S.; Strasser, P. The Mechanism of Water Oxidation: From Electrolysis via Homogeneous to Biological Catalysis. *ChemCatChem* **2010**, *2*, 724-761.
- (41) Sabatier, P. Hydrogénations et déshydrogénations par catalyse. Chem. Ber. 1911, 44, 1984-2001.
- (42) Parsons, R. The Rate of Electrolytic Hydrogen Evolution and the Heat of Adsorption of Hydrogen. *Trans. Faraday Soc.* **1958**, *54*, 1053-1063.
- (43) Zheng, Y.; Jiao, Y.; Zhu, Y.; Li, L. H.; Han, Y.; Chen, Y.; Du, A.; Jaroniec, M.; Qiao, S. Z. Hydrogen Evolution by a Metal-Free Electrocatalyst. *Nat. Commun.* **2014**, *5*, 3783.
- (44) Trasatti, S. Work Function, Electronegativity, and Electrochemical Behaviour of Metals: III. Electrolytic Hydrogen Evolution in Acid Solutions. *J. Electroanal. Chem. Interf. Electrochem.* **1972**, *39*, 163-184.
- (45) Rossmeisl, J.; Karlberg, G. S.; Jaramillo, T.; Nørskov, J. K. Steady State Oxygen Reduction and Cyclic Voltammetry. *Faraday Discuss.* **2009**, *140*, 337-346.
- (46) Hammer, B.; Norskov, J. K. Why Gold is the Noblest of all the Metals. *Nature* **1995**, *376*, 238-240.
- (47) Zheng, Y.; Jiao, Y.; Vasileff, A.; Qiao, S.-Z. The Hydrogen Evolution Reaction in Alkaline Solution: From Theory, Single Crystal Models, to Practical Electrocatalysts. *Angew. Chem. Int. Ed.* **2018**, *57*, 7568-7579.
- (48) Kibler, L. A.; El-Aziz, A. M.; Hoyer, R.; Kolb, D. M. Tuning Reaction Rates by Lateral Strain in a Palladium Monolayer. *Angew. Chem. Int. Ed.* **2005**, *44*, 2080-2084.
- (49) Jiang, K.; Zhang, H.-X.; Zou, S.; Cai, W.-B. Electrocatalysis of Formic Acid on Palladium and Platinum Surfaces: From Fundamental Mechanisms to Fuel Cell Applications. *Phys. Chem. Chem. Phys.* **2014**, *16*, 20360-20376.
- (50) Ruban, A.; Hammer, B.; Stoltze, P.; Skriver, H. L.; Nørskov, J. K. Surface Electronic Structure and Reactivity of Transition and Noble Metals. *J. Mol. Catal. A Chem.* **1997**, *115*, 421-429.

- (51) Mavrikakis, M.; Hammer, B.; Nørskov, J. K. Effect of Strain on the Reactivity of Metal Surfaces. *Phys. Rev. Lett.* **1998**, *81*, 2819-2822.
- (52) Quaino, P.; Santos, E.; Soldano, G.; Schmickler, W. Recent Progress in Hydrogen Electrocatalysis. *Adv. Phys. Chem.* **2011**, *2011*, 851640.
- (53) Wakisaka, M.; Mitsui, S.; Hirose, Y.; Kawashima, K.; Uchida, H.; Watanabe, M. Electronic Structures of Pt–Co and Pt–Ru Alloys for CO-Tolerant Anode Catalysts in Polymer Electrolyte Fuel Cells Studied by EC–XPS. *J. Phys. Chem. B* **2006**, *110*, 23489-23496.
- (54) Liu, X.; Meng, C.; Han, Y. Defective Graphene Supported MPd₁₂ (M= Fe, Co, Ni, Cu, Zn, Pd) Nanoparticles as Potential Oxygen Reduction Electrocatalysts: A First-Principles Study. J. Phys. Chem. C 2013, 117, 1350-1357.
- (55) Zheng, Y.; Jiao, Y.; Jaroniec, M.; Qiao, S. Z. Advancing the Electrochemistry of the Hydrogen-Evolution Reaction through Combining Experiment and Theory. *Angew. Chem. Int. Ed.* **2015**, *54*, 52-65.
- (56) Jiao, Y.; Zheng, Y.; Davey, K.; Qiao, S. Activity Origin and Catalyst Design Principles for Electrocatalytic Hydrogen Evolution on Heteroatom-Doped Graphene. *Nat. Energy* **2016**, *1*, 16130.
- (57) Zheng, Y.; Jiao, Y.; Li, L. H.; Xing, T.; Chen, Y.; Jaroniec, M.; Qiao, S. Z. Toward Design of Synergistically Active Carbon-Based Catalysts for Electrocatalytic Hydrogen Evolution. *ACS Nano* **2014**, *8*, 5290-5296.
- (58) Wang, X.; Vasileff, A.; Jiao, Y.; Zheng, Y.; Qiao, S. Electronic and Structural Engineering of Carbon-Based Metal-Free Electrocatalysts for Water Splitting. *Adv. Mater.* **2019**, *31*, 1803625.
- (59) Rheinländer, P. J.; Herranz, J.; Durst, J.; Gasteiger, H. A. Kinetics of the Hydrogen Oxidation/Evolution Reaction on Polycrystalline Platinum in Alkaline Electrolyte Reaction Order with Respect to Hydrogen Pressure. *J. Electrochem. Soc.* **2014**, *161*, F1448-F1457.
- (60) Trout, B. L.; Parrinello, M. Analysis of the Dissociation of H₂O in Water Using First-Principles Molecular Dynamics. *J. Phys. Chem. B* **1999**, *103*, 7340-7345.
- (61) Ledezma-Yanez, I.; Wallace, W. D. Z.; Sebastián-Pascual, P.; Climent, V.; Feliu, J. M.; Koper, M. T. M. Interfacial Water Reorganization as a pH-Dependent Descriptor of the Hydrogen Evolution Rate on Platinum Electrodes. *Nat. Energy* 2017, 2, 17031.
- (62) Mahmood, N.; Yao, Y.; Zhang, J.-W.; Pan, L.; Zhang, X.; Zou, J.-J. Electrocatalysts for Hydrogen Evolution in Alkaline Electrolytes: Mechanisms, Challenges, and Prospective Solutions. *Adv. Sci.* **2018**, *5*, 1700464.
- (63) Conway, B. E.; Jerkiewicz, G. Relation of Energies and Coverages of Underpotential and Overpotential Deposited H at Pt and Other Metals to the 'Volcano Curve' for Cathodic H₂ Evolution Kinetics. *Electrochim. Acta* **2000**, *45*, 4075-4083.
- (64) Zeradjanin, A. R.; Grote, J.-P.; Polymeros, G.; Mayrhofer, K. J. J. A Critical Review on Hydrogen Evolution Electrocatalysis: Re-exploring the Volcano-relationship. *Electroanalysis* **2016**, *28*, 2256-2269.
- (65) Zheng, Y.; Jiao, Y.; Zhu, Y.; Li, L. H.; Han, Y.; Chen, Y.; Jaroniec, M.; Qiao, S.-Z. High Electrocatalytic Hydrogen Evolution Activity of an Anomalous Ruthenium Catalyst. *J. Am. Chem. Soc.* **2016**, *138*, 16174-16181.
- (66) Fajín, J. L. C.; D. S. Cordeiro, M. N.; Gomes, J. R. B. Density Functional Theory Study of the Water Dissociation on Platinum Surfaces: General Trends. *J. Phys. Chem. A* **2014**, *118*, 5832-5840.
- (67) Fajin, J. L.; Cordeiro, M. N. I. D.; Gomes, J. R. Water Dissociation on Bimetallic Surfaces: General Trends. *J. Phys. Chem. C* **2012**, *116*, 10120-10128.
- (68) Karlberg, G. S. Adsorption Trends for Water, Hydroxyl, Oxygen, and Hydrogen on Transition-Metal and Platinum-Skin Surfaces. *Phys. Rev. B* **2006**, *74*, 153414.

- (69) McCrory, C. C. L.; Jung, S.; Peters, J. C.; Jaramillo, T. F. Benchmarking Heterogeneous Electrocatalysts for the Oxygen Evolution Reaction. *J. Am. Chem. Soc.* **2013**, *135*, 16977-16987.
- (70) Görlin, M.; Ferreira de Araújo, J.; Schmies, H.; Bernsmeier, D.; Dresp, S.; Gliech, M.; Jusys, Z.; Chernev, P.; Kraehnert, R.; Dau, H.et al. Tracking Catalyst Redox States and Reaction Dynamics in Ni–Fe Oxyhydroxide Oxygen Evolution Reaction Electrocatalysts: The Role of Catalyst Support and Electrolyte pH. J. Am. Chem. Soc. 2017, 139, 2070-2082.
- (71) Seitz, L. C.; Dickens, C. F.; Nishio, K.; Hikita, Y.; Montoya, J.; Doyle, A.; Kirk, C.; Vojvodic, A.; Hwang, H. Y.; Norskov, J. K.et al. A Highly Active and Stable IrO_x/SrIrO₃ Catalyst for the Oxygen Evolution Reaction. *Science* **2016**, *353*, 1011-1014.
- (72) Hu, C.; Zhang, L.; Gong, J. Recent Progress Made in the Mechanism Comprehension and Design of Electrocatalysts for Alkaline Water Splitting. *Energy Environ. Sci.* **2019**, *12*, 2620-2645.
- (73) Giordano, L.; Han, B.; Risch, M.; Hong, W. T.; Rao, R. R.; Stoerzinger, K. A.; Shao-Horn, Y. pH Dependence of OER Activity of Oxides: Current and Future Perspectives. *Catal. Today* **2016**, *262*, 2-10.
- (74) Valdés, Á.; Brillet, J.; Grätzel, M.; Gudmundsdóttir, H.; Hansen, H. A.; Jónsson, H.; Klüpfel, P.; Kroes, G.-J.; Le Formal, F.; Man, I. C.et al. Solar Hydrogen Production with Semiconductor Metal Oxides: New Directions in Experiment and Theory. *Phys. Chem. Chem. Phys.* **2012**, *14*, 49-70.
- (75) Su, H.-Y.; Gorlin, Y.; Man, I. C.; Calle-Vallejo, F.; Nørskov, J. K.; Jaramillo, T. F.; Rossmeisl, J. Identifying Active Surface Phases for Metal Oxide Electrocatalysts: a Study of Manganese Oxide Bi-functional Catalysts for Oxygen Reduction and Water Oxidation Catalysis. *Phys. Chem. Chem. Phys.* **2012**, *14*, 14010-14022.
- (76) Man, I. C.; Su, H.-Y.; Calle-Vallejo, F.; Hansen, H. A.; Martínez, J. I.; Inoglu, N. G.; Kitchin, J.; Jaramillo, T. F.; Nørskov, J. K.; Rossmeisl, J. Universality in Oxygen Evolution Electrocatalysis on Oxide Surfaces. *ChemCatChem* **2011**, *3*, 1159-1165.
- (77) Fabbri, E.; Habereder, A.; Waltar, K.; Kötz, R.; Schmidt, T. J. Developments and Perspectives of Oxide-based Catalysts for the Oxygen Evolution Reaction. *Catal. Sci. Technol.* **2014**, *4*, 3800-3821.
- (78) Hammer, B. N., Jens Kehlet. Theoretical surface science and catalysis calculations and concepts. *Adv. Catal.* **2000**, *45*, 71.
- (79) Bjørk Hammer, J. K. N. Theoretical Surface Science and Catalysis Calculations and Concepts. *Adv. Catal.* **2000**, *45*, 71-129.
- (80) Suntivich, J.; May, K. J.; Gasteiger, H. A.; Goodenough, J. B.; Shao-Horn, Y. A Perovskite Oxide Optimized for Oxygen Evolution Catalysis from Molecular Orbital Principles. *Science* **2011**, *334*, 1383-1385.
- (81) Vojvodic, A.; Nørskov, J. K. Optimizing Perovskites for the Water-Splitting Reaction. *Science* **2011**, *334*, 1355-1356.
- (82) Grimaud, A.; May, K. J.; Carlton, C. E.; Lee, Y.-L.; Risch, M.; Hong, W. T.; Zhou, J.; Shao-Horn, Y. Double Perovskites as a Family of Highly Active Catalysts for Oxygen Evolution in Alkaline Solution. *Nat. Commun.* **2013**, *4*, 2439.
- (83) Ballhausen, C. J.; Gray, H. B. The Electronic Structure of the Vanadyl Ion. *Inorg. Chem.* **1962,** *1*, 111-122.
- (84) Zheng, Y.; Jiao, Y.; Zhu, Y.; Cai, Q.; Vasileff, A.; Li, L. H.; Han, Y.; Chen, Y.; Qiao, S.-Z. Molecule-Level g-C₃N₄ Coordinated Transition Metals as a New Class of Electrocatalysts for Oxygen Electrode Reactions. *J. Am. Chem. Soc.* **2017**, *139*, 3336-3339.
- (85) Morgan Chan, Z.; Kitchaev, D. A.; Nelson Weker, J.; Schnedermann, C.; Lim, K.; Ceder, G.; Tumas, W.; Toney, M. F.; Nocera, D. G. Electrochemical Trapping of Metastable Mn³⁺ Ions for Activation of MnO₂ Oxygen Evolution Catalysts. *Proc. Natl. Acad. Sci.* **2018**, *115*, E5261-E5268.

- (86) Jasem, S.; Tseung, A. A Potentiostatic Pulse Study of Oxygen Evolution on Teflon-Bonded Nickel-Cobalt Oxide Electrodes. *J. Electrochem. Soc.* **1979**, *126*, 1353.
- (87) Lu, Z.; Chen, G.; Li, Y.; Wang, H.; Xie, J.; Liao, L.; Liu, C.; Liu, Y.; Wu, T.; Li, Y. Identifying the Active Surfaces of Electrochemically Tuned LiCoO₂ for Oxygen Evolution Reaction. *J. Am. Chem. Soc.* **2017**, *139*, 6270-6276.
- (88) Liu, B.; Chen, H. M.; Liu, C.; Andrews, S. C.; Hahn, C.; Yang, P. Large-Scale Synthesis of Transition-Metal-Doped TiO₂ Nanowires with Controllable Overpotential. *J. Am. Chem. Soc.* **2013**, *135*, 9995-9998.
- (89) Zhai, Y.; Dou, Y.; Zhao, D.; Fulvio, P. F.; Mayes, R. T.; Dai, S. Carbon Materials for Chemical Capacitive Energy Storage. *Adv. Mater.* **2011**, *23*, 4828-4850.
- (90) Kim, K. i.; Guo, Q.; Tang, L.; Zhu, L.; Pan, C.; Chang, C. h.; Razink, J.; Lerner, M. M.; Fang, C.; Ji, X. Reversible Insertion of Mg-Cl Superhalides in Graphite as a Cathode for Aqueous Dual-Ion Batteries. *Angew. Chem. Int. Ed.* **2020**, *132*, 20096-20100.
- (91) Jiao, Y.; Zheng, Y.; Jaroniec, M.; Qiao, S. Z. Origin of the Electrocatalytic Oxygen Reduction Activity of Graphene-Based Catalysts: A Roadmap to Achieve the Best Performance. *J. Am. Chem. Soc.* **2014**, *136*, 4394-4403.
- (92) Foster, J. P.; Weinhold, F. Natural Hybrid Orbitals. J. Am. Chem. Soc. 1980, 102, 7211-7218.
- (93) Xia, C.; Back, S.; Ringe, S.; Jiang, K.; Chen, F.; Sun, X.; Siahrostami, S.; Chan, K.; Wang, H. Confined Local Oxygen Gas Promotes Electrochemical Water Oxidation to Hydrogen Peroxide. *Nat. Catal.* 2020, 3, 125-134.
- (94) Danilovic, N.; Subbaraman, R.; Chang, K.-C.; Chang, S. H.; Kang, Y. J.; Snyder, J.; Paulikas, A. P.; Strmcnik, D.; Kim, Y.-T.; Myers, D. Activity–Stability Trends for the Oxygen Evolution Reaction on Monometallic Oxides in Acidic Environments. *J. Phys. Chem. Lett.* **2014**, *5*, 2474-2478.
- (95) William D Callister, J., David G Rethwisch *Materials Science and Engineering : An Introduction*; Wiley, 2018.
- (96) Zhao, G.; Rui, K.; Dou, S. X.; Sun, W. Heterostructures for Electrochemical Hydrogen Evolution Reaction: A Review. *Adv. Funct. Mater.* **2018**, *28*, 1803291.
- (97) Trasatti, S. Electrocatalysis in the Anodic Evolution of Oxygen and Chlorine. *Electrochim. Acta* **1984**, *29*, 1503-1512.
- (98) Wang, X.; Xu, C.; Jaroniec, M.; Zheng, Y.; Qiao, S.-Z. Anomalous Hydrogen Evolution Behavior in High-pH Environment Induced by Locally Generated Hydronium Ions. *Nat. Commun.* **2019**, *10*, 4876.
- (99) Katsounaros, I.; Meier, J. C.; Klemm, S. O.; Topalov, A. A.; Biedermann, P. U.; Auinger, M.; Mayrhofer, K. J. J. The Effective Surface pH during Reactions at the Solid–Liquid Interface. *Electrochem. Commun.* **2011,** *13*, 634-637.
- (100) Zou, X.; Huang, X.; Goswami, A.; Silva, R.; Sathe, B. R.; Mikmeková, E.; Asefa, T. Cobalt-Embedded Nitrogen-Rich Carbon Nanotubes Efficiently Catalyze Hydrogen Evolution Reaction at All pH Values. *Angew. Chem. Int. Ed.* **2014**, *53*, 4372-4376.
- (101) Wang, J.; Xu, F.; Jin, H.; Chen, Y.; Wang, Y. Non-Noble Metal-based Carbon Composites in Hydrogen Evolution Reaction: Fundamentals to Applications. *Adv. Mater.* **2017**, *29*, 1605838.
- (102) Meyer, R. E. Cathodic Processes on Passive Zirconium. J. Electrochem. Soc. 1960, 107, 847.
- (103) Choi, C.; Ashby, D. S.; Butts, D. M.; DeBlock, R. H.; Wei, Q.; Lau, J.; Dunn, B. Achieving High Energy Density and High Power Density with Pseudocapacitive Materials. *Nat. Rev. Mater.* **2020**, *5*, 5-19.
- (104) Sui, Y.; Liu, C.; Masse, R. C.; Neale, Z. G.; Atif, M.; AlSalhi, M.; Cao, G. Dual-lon Batteries: The Emerging Alternative Rechargeable Batteries. *Energy Stor. Mater.* **2020**, *25*, 1-32.

- (105) Zhou, X.; Liu, Q.; Jiang, C.; Ji, B.; Ji, X.; Tang, Y.; Cheng, H.-M. Strategies towards Low-Cost Duallon Batteries with High Performance. *Angew. Chem. Int. Ed.* **2020**, *59*, 3802-3832.
- (106) Suo, L.; Borodin, O.; Sun, W.; Fan, X.; Yang, C.; Wang, F.; Gao, T.; Ma, Z.; Schroeder, M.; von Cresce, A.et al. Advanced High-Voltage Aqueous Lithium-Ion Battery Enabled by "Water-in-Bisalt" Electrolyte. *Angew. Chem. Int. Ed.* **2016**, *55*, 7136-7141.
- (107) Yang, C.; Chen, J.; Ji, X.; Pollard, T. P.; Lü, X.; Sun, C.-J.; Hou, S.; Liu, Q.; Liu, C.; Qing, T.et al. Aqueous Li-Ion Battery Enabled by Halogen Conversion–Intercalation Chemistry in Graphite. *Nature* **2019**, *569*, 245-250.
- (108) Ko, S.; Yamada, Y.; Miyazaki, K.; Shimada, T.; Watanabe, E.; Tateyama, Y.; Kamiya, T.; Honda, T.; Akikusa, J.; Yamada, A. Lithium-salt monohydrate melt: A stable electrolyte for aqueous lithium-ion batteries. *Electrochem. Commun.* **2019**, *104*, 106488.
- (109) Yamada, Y.; Usui, K.; Sodeyama, K.; Ko, S.; Tateyama, Y.; Yamada, A. Hydrate-Melt Electrolytes for High-Energy-Density Aqueous Batteries. *Nat. Energy* **2016**, *1*, 16129.
- (110) Holoubek, J. J.; Jiang, H.; Leonard, D.; Qi, Y.; Bustamante, G. C.; Ji, X. Amorphous Titanic Acid Electrode: Its Electrochemical Storage of Ammonium in a New Water-in-Salt Electrolyte. *Chem. Commun.* **2018**, *54*, 9805-9808.
- (111) Tian, Z.; Deng, W.; Wang, X.; Liu, C.; Li, C.; Chen, J.; Xue, M.; Li, R.; Pan, F. Superconcentrated Aqueous Electrolyte to Enhance Energy Density for Advanced Supercapacitors. *Funct. Mater. Lett.* **2017**, *10*, 1750081.
- (112) Leonard, D. P.; Wei, Z.; Chen, G.; Du, F.; Ji, X. Water-in-Salt Electrolyte for Potassium-Ion Batteries. *ACS Energy Lett.* **2018**, *3*, 373-374.
- (113) Qiu, S.; Xu, Y.; Li, X.; Sandstrom, S. K.; Wu, X.; Ji, X. Reinforced Potassium and Ammonium Storage of the Polyimide Anode in Acetate-Based Water-in-Salt Electrolytes. *Electrochem. Commun.* **2021**, *122*, 106880.
- (114) Lukatskaya, M. R.; Feldblyum, J. I.; Mackanic, D. G.; Lissel, F.; Michels, D. L.; Cui, Y.; Bao, Z. Concentrated Mixed Cation Acetate "Water-in-Salt" Solutions as Green and Low-Cost High Voltage Electrolytes for Aqueous Batteries. *Energy Environ. Sci.* **2018**, *11*, 2876-2883.
- (115) Han, J.; Zarrabeitia, M.; Mariani, A.; Jusys, Z.; Hekmatfar, M.; Zhang, H.; Geiger, D.; Kaiser, U.; Behm, R. J.; Varzi, A. Halide-Free Water-in-Salt Electrolytes for Stable Aqueous Sodium-Ion Batteries. *Nano Energy* **2020**, *77*, 105176.
- (116) Zhang, C.; Holoubek, J.; Wu, X.; Daniyar, A.; Zhu, L.; Chen, C.; Leonard, D. P.; Rodríguez-Pérez, I. A.; Jiang, J.-X.; Fang, C.et al. A ZnCl₂ Water-in-Salt Electrolyte for a Reversible Zn Metal Anode. Chem. Commun. 2018, 54, 14097-14099.
- (117) Zhao, J.; Zhang, J.; Yang, W.; Chen, B.; Zhao, Z.; Qiu, H.; Dong, S.; Zhou, X.; Cui, G.; Chen, L. "Water-in-Deep Eutectic Solvent" Electrolytes Enable Zinc Metal Anodes for Rechargeable Aqueous Batteries. *Nano Energy* **2019**, *57*, 625-634.
- (118) Yang, W.; Du, X.; Zhao, J.; Chen, Z.; Li, J.; Xie, J.; Zhang, Y.; Cui, Z.; Kong, Q.; Zhao, Z. Hydrated Eutectic Electrolytes with Ligand-Oriented Solvation Shells for Long-Cycling Zinc-Organic Batteries. *Joule* **2020**, *4*, 1557-1574.
- (119) Zhang, Q.; Vigier, K. D. O.; Royer, S.; Jerome, F. Deep Eutectic Solvents: Syntheses, Properties and Applications. *Chem. Soc. Rev.* **2012**, *41*, 7108-7146.
- (120) Yang, H.; Chang, Z.; Qiao, Y.; Deng, H.; Mu, X.; He, P.; Zhou, H. Constructing a Super-Saturated Electrolyte Front Surface for Stable Rechargeable Aqueous Zinc Batteries. *Angew. Chem. Int. Ed.* **2020**, *59*, 9377-9381.
- (121) Sides, W. D.; Huang, Q. Ruthenium Electrodeposition from Water-in-Salt Electrolytes and the Influence of Tetrabutylammonium. *J. Electrochem. Soc.* **2020**, *167*, 062509.

- (122) Bi, H.; Wang, X.; Liu, H.; He, Y.; Wang, W.; Deng, W.; Ma, X.; Wang, Y.; Rao, W.; Chai, Y.et al. A Universal Approach to Aqueous Energy Storage via Ultralow-Cost Electrolyte with Super-Concentrated Sugar as Hydrogen-Bond-Regulated Solute. *Adv. Mater.* **2020**, *32*, 2000074.
- (123) Cao, L.; Li, D.; Hu, E.; Xu, J.; Deng, T.; Ma, L.; Wang, Y.; Yang, X.-Q.; Wang, C. Solvation Structure Design for Aqueous Zn Metal Batteries. *J. Am. Chem. Soc.* **2020**, *142*, 21404-21409.
- (124) Hao, J.; Yuan, L.; Ye, C.; Chao, D.; Davey, K.; Guo, Z.; Qiao, S. Boosting Zn Electrode Reversibility in Aqueous Electrolyte Using Low-Cost Antisolvents. *Angew. Chem. Int. Ed.* **2021**, DOI:10.1002/ange.202016531.
- (125) Yu, F.; Pang, L.; Wang, X.; Waclawik, E. R.; Wang, F.; Ostrikov, K.; Wang, H. Aqueous Alkaline—Acid Hybrid Electrolyte for Zinc-Bromine Battery with 3V Voltage Window. *Energy Stor. Mater.* **2019**, *19*, 56-61.
- (126) Chen, L.; Guo, Z.; Xia, Y.; Wang, Y. High-Voltage Aqueous Battery Approaching 3 V Using an Acidic–Alkaline Double Electrolyte. *Chem. Commun.* **2013**, *49*, 2204-2206.
- (127) Zhong, C.; Liu, B.; Ding, J.; Liu, X.; Zhong, Y.; Li, Y.; Sun, C.; Han, X.; Deng, Y.; Zhao, N.et al. Decoupling Electrolytes towards Stable and High-Energy Rechargeable Aqueous Zinc–Manganese Dioxide Batteries. *Nat. Energy* **2020**, *5*, 440-449.
- (128) Li, C.; Wu, W.; Zhang, S.; He, L.; Zhu, Y.; Wang, J.; Fu, L.; Chen, Y.; Wu, Y.; Huang, W. A High-Voltage Aqueous Lithium Ion Capacitor with High Energy Density from an Alkaline–Neutral Electrolyte. *J. Mater. Chem. A* **2019**, *7*, 4110-4118.
- (129) Chao, D.; Ye, C.; Xie, F.; Zhou, W.; Zhang, Q.; Gu, Q.; Davey, K.; Gu, L.; Qiao, S.-Z. Atomic Engineering Catalyzed MnO₂ Electrolysis Kinetics for a Hybrid Aqueous Battery with High Power and Energy Density. *Adv. Mater.* **2020**, *32*, 2001894.
- (130) Li, C.; Wu, W.; Wang, P.; Zhou, W.; Wang, J.; Chen, Y.; Fu, L.; Zhu, Y.; Wu, Y.; Huang, W. Fabricating an Aqueous Symmetric Supercapacitor with a Stable High Working Voltage of 2 V by Using an Alkaline–Acidic Electrolyte. *Adv. Sci.* **2019**, *6*, 1801665.
- (131) Wang, X.; Chandrabose, R. S.; Jian, Z.; Xing, Z.; Ji, X. A 1.8 V Aqueous Supercapacitor with a Bipolar Assembly of Ion-Exchange Membranes as the Separator. *J. Electrochem. Soc.* **2016**, *163*, A1853-A1858.
- (132) Dietz, H.; Hoogestraat, G.; Laibach, S.; von Borstel, D.; Wiesener, K. Influence of Substituted Benzaldehydes and Their Derivatives as Inhibitors for Hydrogen Evolution in Lead/Acid Batteries. *J. Power Sources* **1995**, *53*, 359-365.
- (133) Tong, P.; Zhao, R.; Zhang, R.; Yi, F.; Shi, G.; Li, A.; Chen, H. Characterization of Lead (||)Containing Activated Carbon and Its Excellent Performance of Extending Lead-Acid Battery Cycle
 Life for High-Rate Partial-State-of-Charge Operation. *J. Power Sources* **2015**, *286*, 91-102.
- (134) Xiang, J.; Ding, P.; Zhang, H.; Wu, X.; Chen, J.; Yang, Y. Beneficial Effects of Activated Carbon Additives on the Performance of Negative Lead-Acid Battery Electrode for High-Rate Partial-State-of-Charge Operation. *J. Power Sources* **2013**, *241*, 150-158.
- (135) Lam, L. T.; Louey, R. Development of Ultra-Battery for Hybrid-Electric Vehicle Applications. *J. Power Sources* **2006**, *158*, 1140-1148.
- (136) Furukawa, J.; Takada, T.; Monma, D.; Lam, L. T. Further Demonstration of the VRLA-type UltraBattery Under Medium-HEV Duty and Development of the Flooded-Type UltraBattery for Micro-HEV Applications. *J. Power Sources* **2010**, *195*, 1241-1245.
- (137) Zeng, Y.; Lin, Z.; Wang, Z.; Wu, M.; Tong, Y.; Lu, X. In Situ Activation of 3D Porous Bi/Carbon Architectures: Toward High-Energy and Stable Nickel–Bismuth Batteries. *Adv. Mater.* **2018**, *30*, 1707290.
- (138) Zhang, X. G. Corrosion and Electrochemistry of Zinc; Springer, 1996.

- (139) Ma, L.; Li, N.; Long, C.; Dong, B.; Fang, D.; Liu, Z.; Zhao, Y.; Li, X.; Fan, J.; Chen, S.et al. Achieving Both High Voltage and High Capacity in Aqueous Zinc-Ion Battery for Record High Energy Density. *Adv. Funct. Mater.* **2019**, *29*, 1906142.
- (140) Beverskog, B.; Puigdomenech, I. Revised Pourbaix Diagrams for Zinc at 25–300 °C. *Corros. Sci.* **1997**, *39*, 107-114.
- (141) Barton, G. W.; Scott, A. C. A Validated Mathematical Model for a Zinc Electrowinning Cell. *J. Appl. Electrochem.* **1992**, *22*, 104-115.
- (142) Minakshi, M.; Ionescu, M. Anodic Behavior of Zinc in Zn-MnO₂ Battery Using ERDA Technique. *Int. J. Hydrog. Energy* **2010**, *35*, 7618-7622.
- (143) Zou, P.; Chiang, S. W.; Zhan, H.; Sui, Y.; Liu, K.; Hu, S.; Su, S.; Li, J.; Kang, F.; Yang, C. A Periodic "Self-Correction" Scheme for Synchronizing Lithium Plating/Stripping at Ultrahigh Cycling Capacity. *Adv. Funct. Mater.* **2020**, *30*, 1910532.
- (144) Liu, W.; Liu, P.; Mitlin, D. Tutorial Review on Structure Dendrite Growth Relations in Metal Battery Anode Supports. *Chem. Soc. Rev.* **2020,** *49*, 7284-7300.
- (145) Jäckle, M.; Groß, A. Microscopic Properties of Lithium, Sodium, and Magnesium Battery Anode Materials Related to Possible Dendrite Growth. *J. Chem. Phys.* **2014**, *141*, 174710.
- (146) Jäckle, M.; Helmbrecht, K.; Smits, M.; Stottmeister, D.; Groß, A. Self-Diffusion Barriers: Possible Descriptors for Dendrite Growth in Batteries? *Energy Environ. Sci.* **2018**, *11*, 3400-3407.
- (147) Sand, H. J. III. On the Concentration at the Electrodes in a Solution, with Special Reference to the Liberation of Hydrogen by Electrolysis of a Mixture of Copper Sulphate and Sulphuric Acid. *Lond. Edinb. Dubl. Phil. Mag. J. Sci.* **1901**, *1*, 45-79.
- (148) Brissot, C.; Rosso, M.; Chazalviel, J.-N.; Lascaud, S. Dendritic Growth Mechanisms in Lithium/Polymer Cells. *J. Power Sources* **1999**, *81*, 925-929.
- (149) Li, S.; Jiang, M.; Xie, Y.; Xu, H.; Jia, J.; Li, J. Developing High-Performance Lithium Metal Anode in Liquid Electrolytes: Challenges and Progress. *Adv. Mater.* **2018**, *30*, 1706375.
- (150) Nong, S.; Dong, W.; Yin, J.; Dong, B.; Lu, Y.; Yuan, X.; Wang, X.; Bu, K.; Chen, M.; Jiang, S.et al. Well-Dispersed Ruthenium in Mesoporous Crystal TiO₂ as an Advanced Electrocatalyst for Hydrogen Evolution Reaction. *J. Am. Chem. Soc.* **2018**, *140*, 5719-5727.
- (151) Konarov, A.; Voronina, N.; Jo, J. H.; Bakenov, Z.; Sun, Y.-K.; Myung, S.-T. Present and Future Perspective on Electrode Materials for Rechargeable Zinc-Ion Batteries. *ACS Energy Lett.* **2018**, *3*, 2620-2640.
- (152) Wu, Y.; Zhang, Y.; Ma, Y.; Howe, J. D.; Yang, H.; Chen, P.; Aluri, S.; Liu, N. Ion-Sieving Carbon Nanoshells for Deeply Rechargeable Zn-Based Aqueous Batteries. *Adv. Energy Mater.* **2018**, *8*, 1802470.
- (153) Song, J.; Xu, K.; Liu, N.; Reed, D.; Li, X. Crossroads in the Renaissance of Rechargeable Aqueous Zinc Batteries. *Mater. Today* **2021**, DOI:10.1016/j.mattod.2020.12.003.
- (154) Zeng, Y.; Lin, Z.; Meng, Y.; Wang, Y.; Yu, M.; Lu, X.; Tong, Y. Flexible Ultrafast Aqueous Rechargeable Ni//Bi Battery Based on Highly Durable Single-Crystalline Bismuth Nanostructured Anode. *Adv. Mater.* **2016**, *28*, 9188-9195.
- (155) Rajan, A. S.; Sampath, S.; Shukla, A. K. An in Situ Carbon-Grafted Alkaline Iron Electrode for Iron-Based Accumulators. *Energy Environ. Sci.* **2014**, *7*, 1110-1116.
- (156) Hang, B. T.; Yoon, S.-H.; Okada, S.; Yamaki, J.-i. Effect of Metal-Sulfide Additives on Electrochemical Properties of Nano-Sized Fe₂O₃-Loaded Carbon for Fe/Air Battery Anodes. *J. Power Sources* **2007**, *168*, 522-532.
- (157) Marcus, P. Corrosion Mechanisms in Theory and Practice; CRC press, 2011.
- (158) Xie, C.; Li, Y.; Wang, Q.; Sun, D.; Tang, Y.; Wang, H. Issues and Solutions Toward Zinc Anode in Aqueous Zinc-Ion Batteries: A Mini Review. *Carbon Energy* **2020**, *2*, 540-560.

- (159) Weinrich, H.; Come, J.; Tempel, H.; Kungl, H.; Eichel, R.-A.; Balke, N. Understanding the Nanoscale Redox-Behavior of Iron-Anodes for Rechargeable Iron-Air Batteries. *Nano Energy* **2017**, *41*, 706-716.
- (160) Yufit, V.; Tariq, F.; Eastwood, D. S.; Biton, M.; Wu, B.; Lee, P. D.; Brandon, N. P. Operando Visualization and Multi-Scale Tomography Studies of Dendrite Formation and Dissolution in Zinc Batteries. *Joule* **2019**, *3*, 485-502.
- (161) Cai, Z.; Ou, Y.; Wang, J.; Xiao, R.; Fu, L.; Yuan, Z.; Zhan, R.; Sun, Y. Chemically Resistant Cu–Zn/Zn Composite Anode for Long Cycling Aqueous Batteries. *Energy Storage Mater.* **2020**, *27*, 205-211.
- (162) Aghzzaf, A. A.; Rhouta, B.; Rocca, E.; Khalil, A.; Steinmetz, J. Corrosion Inhibition of Zinc by Calcium Exchanged Beidellite Clay Mineral: A New Smart Corrosion Inhibitor. *Corros. Sci.* **2014**, *80*, 46-52.
- (163) Han, D.; Wu, S.; Zhang, S.; Deng, Y.; Cui, C.; Zhang, L.; Long, Y.; Li, H.; Tao, Y.; Weng, Z. A Corrosion-Resistant and Dendrite-Free Zinc Metal Anode in Aqueous Systems. *Small* **2020**, *16*, 2001736.
- (164) He, H.; Tong, H.; Song, X.; Song, X.; Liu, J. Highly Stable Zn Metal Anodes Enabled by Atomic Layer Deposited Al₂O₃ Coating for Aqueous Zinc-Ion Batteries. *J. Mater. Chem. A* **2020**, *8*, 7836-7846.
- (165) Zhao, K.; Wang, C.; Yu, Y.; Yan, M.; Wei, Q.; He, P.; Dong, Y.; Zhang, Z.; Wang, X.; Mai, L. Ultrathin Surface Coating Enables Stabilized Zinc Metal Anode. *Adv. Mater. Interfaces* **2018**, *5*, 1800848.
- (166) Xie, X.; Liang, S.; Gao, J.; Guo, S.; Guo, J.; Wang, C.; Xu, G.; Wu, X.; Chen, G.; Zhou, J. Manipulating the Ion-Transfer Kinetics and Interface Stability for High-Performance Zinc Metal Anodes. *Energy Environ. Sci.* **2020**, *13*, 503-510.
- (167) Cao, L.; Li, D.; Deng, T.; Li, Q.; Wang, C. Hydrophobic Organic-Electrolyte-Protected Zinc Anodes for Aqueous Zinc Batteries. *Angew. Chem. Int. Ed.* **2020**, *59*, 19292-19296.
- (168) Zhao, Z.; Zhao, J.; Hu, Z.; Li, J.; Li, J.; Zhang, Y.; Wang, C.; Cui, G. Long-Life and Deeply Rechargeable Aqueous Zn Anodes Enabled by a Multifunctional Brightener-Inspired Interphase. *Energy Environ. Sci.* **2019**, *12*, 1938-1949.
- (169) Cui, Y.; Zhao, Q.; Wu, X.; Chen, X.; Yang, J.; Wang, Y.; Qin, R.; Ding, S.; Song, Y.; Wu, J. An Interface-Bridged Organic–Inorganic Layer that Suppresses Dendrite Formation and Side Reactions for Ultra-Long-Life Aqueous Zinc Metal Anodes. *Angew. Chem. Int. Ed.* **2020,** *132,* 16737-16744.
- (170) Zhao, R.; Yang, Y.; Liu, G.; Zhu, R.; Huang, J.; Chen, Z.; Gao, Z.; Chen, X.; Qie, L. Redirected Zn Electrodeposition by an Anti-Corrosion Elastic Constraint for Highly Reversible Zn Anodes. *Adv. Funct. Mater.* **2020**, *31*, 2001867.
- (171) Khorsand, S.; Raeissi, K.; Golozar, M. An investigation on the Role of Texture and Surface Morphology in the Corrosion Resistance of Zinc Electrodeposits. *Corros. Sci.* **2011,** *53*, 2676-2678.
- (172) Mouanga, M.; Ricq, L.; Douglade, J.; Berçot, P. Corrosion Behaviour of Zinc Deposits Obtained under Pulse Current Electrodeposition: Effects of Coumarin as Additive. *Corros. Sci.* **2009**, *51*, 690-698.
- (173) Zheng, J.; Zhao, Q.; Tang, T.; Yin, J.; Quilty, C. D.; Renderos, G. D.; Liu, X.; Deng, Y.; Wang, L.; Bock, D. C. Reversible Epitaxial Electrodeposition of Metals in Battery Anodes. *Science* **2019**, *366*, 645-648.
- (174) Sun, K. E.; Hoang, T. K.; Doan, T. N. L.; Yu, Y.; Chen, P. Highly Sustainable Zinc Anodes for a Rechargeable Hybrid Aqueous Battery. *Chem. Eur. J.* **2018**, *24*, 1667-1673.

- (175) Sun, K. E.; Hoang, T. K.; Doan, T. N. L.; Yu, Y.; Zhu, X.; Tian, Y.; Chen, P. Suppression of Dendrite Formation and Corrosion on Zinc Anode of Secondary Aqueous Batteries. *ACS Appl. Mater. Interfaces* **2017**, *9*, 9681-9687.
- (176) Müller, S.; Holzer, F.; Haas, O. Optimized Zinc Electrode for the Rechargeable Zinc–Air Battery. *J. Appl. Electrochem.* **1998**, *28*, 895-898.
- (177) Lee, C. W.; Sathiyanarayanan, K.; Eom, S. W.; Kim, H. S.; Yun, M. S. Effect of Additives on the Electrochemical Behaviour of Zinc Anodes for Zinc/Air Fuel Cells. *J. Power Sources* **2006**, *160*, 161-164.
- (178) Shivkumar, R.; Kalaignan, G. P.; Vasudevan, T. Studies with Porous Zinc Electrodes with Additives for Secondary Alkaline Batteries. *J. Power Sources* **1998**, *75*, 90-100.
- (179) Wang, R.; Yang, Z.; Yang, B.; Wang, T.; Chu, Z. Superior Cycle Stability and High Rate Capability of Zn–Al–In-Hydrotalcite as Negative Electrode Materials for Ni–Zn Secondary Batteries. *J. Power Sources* **2014**, *251*, 344-350.
- (180) Lee, C. W.; Sathiyanarayanan, K.; Eom, S. W.; Yun, M. S. Novel Alloys to Improve the Electrochemical Behavior of Zinc Anodes for Zinc/Air Battery. *J. Power Sources* **2006**, *160*, 1436-1441.
- (181) Yi, Z.; Chen, G.; Hou, F.; Wang, L.; Liang, J. Strategies for the Stabilization of Zn Metal Anodes for Zn-Ion Batteries. *Adv. Energy Mater.* **2020**, *11*, 2003065.
- (182) Liu, S.; Hu, J. J.; Yan, N. F.; Pan, G. L.; Li, G. R.; Gao, X. P. Aluminum Storage Behavior of Anatase TiO₂ Nanotube Arrays in Aqueous Solution for Aluminum Ion Batteries. *Energy Environ. Sci.* **2012**, *5*, 9743-9746.
- (183) Verma, V.; Kumar, S.; Manalastas Jr., W.; Satish, R.; Srinivasan, M. Progress in Rechargeable Aqueous Zinc- and Aluminum-Ion Battery Electrodes: Challenges and Outlook. *Adv. Sustain. Syst.* **2019**, *3*, 1800111.
- (184) Reiman, K. H.; Brace, K. M.; Gordon-Smith, T. J.; Nandhakumar, I.; Attard, G. S.; Owen, J. R. Lithium Insertion into TiO₂ from Aqueous Solution − Facilitated by Nanostructure. *Electrochem. Commun.* **2006**, *8*, 517-522.
- (185) Wu, M.-S.; Wang, M.-J.; Jow, J.-J.; Yang, W.-D.; Hsieh, C.-Y.; Tsai, H.-M. Electrochemical Fabrication of Anatase TiO₂ Nanostructure as an Anode Material for Aqueous Lithium-Ion Batteries. *J. Power Sources* **2008**, *185*, 1420-1424.
- (186) Manickam, M.; Singh, P.; Issa, T. B.; Thurgate, S. Electrochemical Behavior of Anatase TiO₂ in Aqueous Lithium Hydroxide Electrolyte. *J. Appl. Electrochem.* **2006**, *36*, 599-602.
- (187) Tang, Y.; Li, Y.; Guo, W.; Wang, J.; Li, X.; Chen, S.; Mu, S.; Zhao, Y.; Gao, F. A Highly Ordered Multi-Layered Hydrogenated TiO₂-II Phase Nanowire Array Negative Electrode for 2.4 V Aqueous Asymmetric Supercapacitors with High Energy Density and Long Cycle Life. *J. Mater. Chem. A* **2018**, *6*, 623-632.
- (188) Li, R.; Ba, X.; Zhang, H.; Xu, P.; Li, Y.; Cheng, C.; Liu, J. Conformal Multifunctional Titania Shell on Iron Oxide Nanorod Conversion Electrode Enables High Stability Exceeding 30 000 Cycles in Aqueous Electrolyte. Adv. Funct. Mater. 2018, 28, 1800497.
- (189) Wu, G.; Li, P.; Zhu, C.; Lei, Y.; Zhao, H.; Li, T.; Yue, H.; Dou, B.; Gao, Y.; Yang, X. Amorphous Titanium Oxide Passivated Lithium Titanium Phosphate Electrode for High Stable Aqueous Lithium Ion Batteries with Oxygen Tolerance. *Electrochim. Acta* **2017**, *246*, 720-729.
- (190) Yan, Y.; Cheng, X.; Zhang, W.; Chen, G.; Li, H.; Konkin, A.; Sun, Z.; Sun, S.; Wang, D.; Schaaf, P. Plasma Hydrogenated TiO₂/Nickel Foam as an Efficient Bifunctional Electrocatalyst for Overall Water Splitting. *ACS Sustain. Chem. Eng.* **2019**, *7*, 885-894.
- (191) Sahoo, R.; Pham, D. T.; Lee, T. H.; Luu, T. H. T.; Seok, J.; Lee, Y. H. Redox-Driven Route for Widening Voltage Window in Asymmetric Supercapacitor. *ACS Nano* **2018**, *12*, 8494-8505.

- (192) Shan, X.; Guo, F.; Charles, D. S.; Lebens-Higgins, Z.; Abdel Razek, S.; Wu, J.; Xu, W.; Yang, W.; Page, K. L.; Neuefeind, J. C.et al. Structural Water and Disordered Structure Promote Aqueous Sodium-Ion Energy Storage in Sodium-Birnessite. *Nat. Commun.* **2019**, *10*, 4975.
- (193) Zhang, Y.; Xia, X.; Cao, X.; Zhang, B.; Tiep, N. H.; He, H.; Chen, S.; Huang, Y.; Fan, H. J. Ultrafine Metal Nanoparticles/N-Doped Porous Carbon Hybrids Coated on Carbon Fibers as Flexible and Binder-Free Water Splitting Catalysts. *Adv. Energy Mater.* **2017**, *7*, 1700220.
- (194) Jabeen, N.; Hussain, A.; Xia, Q.; Sun, S.; Zhu, J.; Xia, H. High-Performance 2.6 V Aqueous Asymmetric Supercapacitors based on In Situ Formed Na_{0.5}MnO₂ Nanosheet Assembled Nanowall Arrays. *Adv. Mater.* **2017**, *29*, 1700804.
- (195) Liu, Z.; Qin, X.; Xu, H.; Chen, G. One-Pot Synthesis of Carbon-Coated Nanosized LiTi₂(PO₄)₃ as Anode Materials for Aqueous Lithium Ion Batteries. *J. Power Sources* **2015**, *293*, 562-569.
- (196) Zhang, H.; Zhou, Y.; Li, C.; Yang, C.; Zhu, T. Phase Separation of the Electron–Ion Conducting Layer on the Surface of a TiP₂O₇ Anode Material for Aqueous Lithium Rechargeable Batteries. *J. Mater. Chem. A* **2016**, *4*, 13390-13394.
- (197) Tao, L.; Wang, Y.; Zou, Y.; Zhang, N.; Zhang, Y.; Wu, Y.; Wang, Y.; Chen, R.; Wang, S. Charge Transfer Modulated Activity of Carbon-Based Electrocatalysts. *Adv. Energy Mater.* **2020**, *10*, 1901227.
- (198) Brennan, M.; Brown, O. Carbon Electrodes: Part 1. Hydrogen Evolution in Acidic Solution. *J. Appl. Electrochem.* **1972**, *2*, 43-49.
- (199) Abbas, Q.; Ratajczak, P.; Babuchowska, P.; Comte, A. L.; Bélanger, D.; Brousse, T.; Béguin, F. Strategies to Improve the Performance of Carbon/Carbon Capacitors in Salt Aqueous Electrolytes. *J. Electrochem. Soc.* **2015**, *162*, A5148-A5157.
- (200) Wang, H.; Maiyalagan, T.; Wang, X. Review on Recent Progress in Nitrogen-Doped Graphene: Synthesis, Characterization, and Its Potential Applications. *ACS Catal.* **2012**, *2*, 781-794.
- (201) Hong, B.; Yu, X.; Jiang, L.; Xue, H.; Liu, F.; Li, J.; Liu, Y. Hydrogen Evolution Inhibition with Diethylenetriamine Modification of Activated Carbon for a Lead-Acid Battery. *RSC Adv.* **2014**, *4*, 33574-33577.
- (202) Jiang, Z.; Wang, T.; Song, L.; Guo, H.; Xia, W.; Gong, H.; Gao, B.; Feng, L.; Liu, X.; He, J. High Over-Potential Nitrogen-Doped Activated Carbon towards Hydrogen Evolution Inhibition in Sulfuric Acid Solution. *J. Mater. Sci. Mater. Electron.* **2018**, *29*, 14170-14179.
- (203) Wang, F.; Hu, C.; Lian, J.; Zhou, M.; Wang, K.; Yan, J.; Jiang, K. Phosphorus-Doped Activated Carbon as a Promising Additive for High Performance Lead Carbon Batteries. *RSC Adv.* **2017,** *7*, 4174-4178.
- (204) Khomenko, V.; Raymundo-Piñero, E.; Béguin, F. A New Type of High Energy Asymmetric Capacitor with Nanoporous Carbon Electrodes in Aqueous Electrolyte. *J. Power Sources* **2010**, 195, 4234-4241.
- (205) Zhou, Y.; Zhu, Z.; Zhao, C.; Zhang, K.; Wang, B.; Zhao, C.; Chen, G. Reclaimed Carbon Fiber-Based 2.4 V Aqueous Symmetric Supercapacitors. *ACS Sustain. Chem. Eng.* **2019**, *7*, 5095-5102.
- (206) Xiong, T.; Tan, T. L.; Lu, L.; Lee, W. S. V.; Xue, J. Harmonizing Energy and Power Density toward 2.7 V Asymmetric Aqueous Supercapacitor. *Adv. Energy Mater.* **2018**, *8*, 1702630.
- (207) Qin, T.; Chen, H.; Zhang, Y.; Chen, X.; Liu, L.; Yan, D.; Ma, S.; Hou, J.; Yu, F.; Peng, S. Modulating Surface Chemistry of Heteroatom-Rich Micropore Carbon Cloth Electrode for Aqueous 2.1 V High-Voltage Window All-Carbon Supercapacitor. *J. Power Sources* **2019**, *431*, 232-238.
- (208) Wu, X.; Huang, B.; Wang, Q.; Wang, Y. Wide Potential and High Energy Density for an Asymmetric Aqueous Supercapacitor. *J. Mater. Chem. A* **2019**, *7*, 19017-19025.
- (209) Zhang, S.-W.; Yin, B.-S.; Liu, X.-X.; Gu, D.-M.; Gong, H.; Wang, Z.-B. A High Energy Density Aqueous Hybrid Supercapacitor with Widened Potential Window through Multi Approaches. *Nano Energy* **2019**, *59*, 41-49.

- (210) Guo, H.-L.; Wang, X.-F.; Qian, Q.-Y.; Wang, F.-B.; Xia, X.-H. A Green Approach to the Synthesis of Graphene Nanosheets. *ACS Nano* **2009**, *3*, 2653-2659.
- (211) Toh, S. Y.; Loh, K. S.; Kamarudin, S. K.; Daud, W. R. W. Graphene Production via Electrochemical Reduction of Graphene Oxide: Synthesis and Characterisation. *Chem. Eng. J.* **2014**, *251*, 422-434.
- (212) Wang, D.; Liu, S.; Jiao, L.; Fang, G.; Geng, G.; Ma, J. Unconventional Mesopore Carbon Nanomesh Prepared through Explosion—Assisted Activation Approach: A Robust Electrode Material for Ultrafast Organic Electrolyte Supercapacitors. *Carbon* **2017**, *119*, 30-39.
- (213) Song, Z.; Zhan, H.; Zhou, Y. Polyimides: Promising Energy-Storage Materials. *Angew. Chem. Int. Ed.* **2010**, *49*, 8444-8448.
- (214) Wu, H.; Shevlin, S. A.; Meng, Q.; Guo, W.; Meng, Y.; Lu, K.; Wei, Z.; Guo, Z. Flexible and Binder-Free Organic Cathode for High-Performance Lithium-Ion Batteries. *Adv. Mater.* **2014**, *26*, 3338-3343.
- (215) Song, Z.; Xu, T.; Gordin, M. L.; Jiang, Y.-B.; Bae, I.-T.; Xiao, Q.; Zhan, H.; Liu, J.; Wang, D. Polymer–Graphene Nanocomposites as Ultrafast-Charge and -Discharge Cathodes for Rechargeable Lithium Batteries. *Nano Lett.* **2012**, *12*, 2205-2211.
- (216) Wang, Y.; Cui, X.; Zhang, Y.; Zhang, L.; Gong, X.; Zheng, G. Achieving High Aqueous Energy Storage via Hydrogen-Generation Passivation. *Adv. Mater.* **2016**, *28*, 7626-7632.
- (217) Deng, W.; Shen, Y.; Qian, J.; Yang, H. A Polyimide Anode with High Capacity and Superior Cyclability for Aqueous Na-Ion Batteries. *Chem. Commun.* **2015**, *51*, 5097-5099.
- (218) Gheytani, S.; Liang, Y.; Wu, F.; Jing, Y.; Dong, H.; Rao, K. K.; Chi, X.; Fang, F.; Yao, Y. An Aqueous Ca-Ion Battery. *Adv. Sci.* **2017**, *4*, 1700465.
- (219) Deng, W.; Shen, Y.; Qian, J.; Cao, Y.; Yang, H. A Perylene Diimide Crystal with High Capacity and Stable Cyclability for Na-Ion Batteries. *ACS Appl. Mater. Interfaces* **2015**, *7*, 21095-21099.
- (220) Wang, H.; Huang, K.; Zeng, Y.; Yang, S.; Chen, L. Electrochemical Properties of TiP_2O_7 and $LiTi_2(PO_4)_3$ as Anode Material for Lithium Ion Battery with Aqueous Solution Electrolyte. *Electrochim. Acta* **2007**, *52*, 3280-3285.
- (221) Wu, X.-y.; Sun, M.-y.; Shen, Y.-f.; Qian, J.-f.; Cao, Y.-l.; Ai, X.-p.; Yang, H.-x. Energetic Aqueous Rechargeable Sodium-Ion Battery Based on Na₂CuFe(CN)₆–NaTi₂(PO₄)₃ Intercalation Chemistry. *ChemSusChem* **2014**, *7*, 407-411.
- (222) Park, S. I.; Gocheva, I.; Okada, S.; Yamaki, J.-i. Electrochemical Properties of NaTi₂(PO₄)₃ Anode for Rechargeable Aqueous Sodium-Ion Batteries. *J. Electrochem. Soc.* **2011**, *158*, A1067.
- (223) Pang, G.; Yuan, C.; Nie, P.; Ding, B.; Zhu, J.; Zhang, X. Synthesis of NASICON-Type Structured NaTi₂(PO₄)₃–Graphene Nanocomposite as an Anode for Aqueous Rechargeable Na-Ion Batteries. *Nanoscale* **2014**, *6*, 6328-6334.
- (224) Xu, J.; Liu, G.; Li, J.; Wang, X. The Electrocatalytic Properties of an IrO₂/SnO₂ Catalyst Using SnO₂ as a Support and an Assisting Reagent for the Oxygen Evolution Reaction. *Electrochim. Acta* **2012**, *59*, 105-112.
- (225) Aromaa, J.; Forsén, O. Evaluation of the Electrochemical Activity of a Ti–RuO₂–TiO₂ Permanent Anode. *Electrochim. Acta* **2006**, *51*, 6104-6110.
- (226) Santana, M. H. P.; De Faria, L. A. Oxygen and Chlorine Evolution on RuO₂+TiO₂+CeO₂+Nb₂O₅ Mixed Oxide Electrodes. *Electrochim. Acta* **2006**, *51*, 3578-3585.
- (227) Ye, Z.-G.; Meng, H.-M.; Chen, D.; Yu, H.-Y.; Huan, Z.-S.; Wang, X.-D.; Sun, D.-B. Structure and Characteristics of Ti/IrO_{2(x)}+MnO_{2(1-x)} Anode for Oxygen Evolution. *Solid State Sci.* **2008**, *10*, 346-354.
- (228) Fernandes, K. C.; Silva, L. M. D.; Boodts, J. F. C.; De Faria, L. A. Surface, Kinetics and Electrocatalytic Properties of the Ti/(Ti+Ru+Ce)O₂-System for the Oxygen Evolution Reaction in Alkaline Medium. *Electrochim. Acta* **2006**, *51*, 2809-2818.

- (229) Dan, Y.; Lu, H.; Liu, X.; Lin, H.; Zhao, J. Ti/PbO₂ + Nano-Co₃O₄ Composite Electrode Material for Electrocatalysis of O₂ Evolution in Alkaline Solution. *Int. J. Hydrog. Energy* **2011**, *36*, 1949-1954.
- (230) Wang, X.-M.; Hu, J.-M.; Zhang, J.-Q. IrO₂–SiO₂ Binary Oxide Films: Preparation, Physiochemical Characterization and Their Electrochemical Properties. *Electrochim. Acta* **2010**, *55*, 4587-4593.
- (231) Li, X.; Pletcher, D.; Walsh, F. C. A Novel Flow Battery: A Lead Acid Battery Based on an Electrolyte with Soluble Lead(II): Part VII. Further Studies of the Lead Dioxide Positive Electrode. *Electrochim. Acta* **2009**, *54*, 4688-4695.
- (232) Abaci, S.; Pekmez, K.; Hökelek, T.; Yildiz, A. Investigation of Some Parameters Influencing Electrocrystallisation of PbO₂. *J. Power Sources* **2000**, *88*, 232-236.
- (233) Dodson, V. H. The Composition and Performance of Positive Plate Material in the Lead-Acid Battery. *J. Electrochem. Soc.* **1961**, *108*, 406.
- (234) Wu, X.; Luo, Y.; Sun, M.; Qian, J.; Cao, Y.; Ai, X.; Yang, H. Low-Defect Prussian Blue Nanocubes as High Capacity and Long Life Cathodes for Aqueous Na-Ion Batteries. *Nano Energy* **2015**, *13*, 117-123.
- (235) Velichenko, A. B.; Girenko, D. V.; Nikolenko, N. V.; Amadelli, R.; Baranova, E. A.; Danilov, F. I. Oxygen Evolution on Lead Dioxide Modified with Fluorine and Iron. *Russ. J. Electrochem.* **2000**, *36*, 1216-1220.
- (236) Cao, J.; Zhao, H.; Cao, F.; Zhang, J. The Influence of F⁻ Doping on the Activity of PbO₂ Film Electrodes in Oxygen Evolution Reaction. *Electrochim. Acta* **2007**, *52*, 7870-7876.
- (237) Huang, M.; Li, F.; Dong, F.; Zhang, Y. X.; Zhang, L. L. MnO₂-Based Nanostructures for High-Performance Supercapacitors. *J. Mater. Chem. A* **2015**, *3*, 21380-21423.
- (238) Sui, Y.; Liu, C.; Zou, P.; Zhan, H.; Cui, Y.; Yang, C.; Cao, G. Polypyrrole Coated δ-MnO₂ Nanosheet Arrays as a Highly Stable Lithium-Ion-Storage Anode. *Dalton Trans.* **2020**, *49*, 7903-7913.
- (239) Ramírez, A.; Hillebrand, P.; Stellmach, D.; May, M. M.; Bogdanoff, P.; Fiechter, S. Evaluation of MnO_x, Mn₂O₃, and Mn₃O₄ Electrodeposited Films for the Oxygen Evolution Reaction of Water. *J. Phys. Chem. C* **2014**, *118*, 14073-14081.
- (240) Walter, C.; Menezes, P. W.; Loos, S.; Dau, H.; Driess, M. Facile Formation of Nanostructured Manganese Oxide Films as High-Performance Catalysts for the Oxygen Evolution Reaction. *ChemSusChem* **2018**, *11*, 2554-2561.
- (241) Cheng, F.; Zhang, T.; Zhang, Y.; Du, J.; Han, X.; Chen, J. Enhancing Electrocatalytic Oxygen Reduction on MnO₂ with Vacancies. *Angew. Chem. Int. Ed.* **2013**, *52*, 2474-2477.
- (242) Zhao, Y.; Chang, C.; Teng, F.; Zhao, Y.; Chen, G.; Shi, R.; Waterhouse, G. I. N.; Huang, W.; Zhang, T. Defect-Engineered Ultrathin δ-MnO₂ Nanosheet Arrays as Bifunctional Electrodes for Efficient Overall Water Splitting. Adv. Energy Mater. 2017, 7, 1700005.
- (243) Wang, J.-G.; Yang, Y.; Huang, Z.-H.; Kang, F. A High-Performance Asymmetric Supercapacitor Based on Carbon and Carbon–MnO₂ Nanofiber Electrodes. *Carbon* **2013**, *61*, 190-199.
- (244) Wu, X.; Wu, C.; Wei, C.; Hu, L.; Qian, J.; Cao, Y.; Ai, X.; Wang, J.; Yang, H. Highly Crystallized Na₂CoFe(CN)₆ with Suppressed Lattice Defects as Superior Cathode Material for Sodium-Ion Batteries. *ACS Appl. Mater. Interfaces* **2016**, *8*, 5393-5399.
- (245) Chen, L.; Shao, H.; Zhou, X.; Liu, G.; Jiang, J.; Liu, Z. Water-Mediated Cation Intercalation of Open-Framework Indium Hexacyanoferrate with High Voltage and Fast Kinetics. *Nat. Commun.* **2016**, *7*, 11982.
- (246) Wu, X.; Sun, M.; Guo, S.; Qian, J.; Liu, Y.; Cao, Y.; Ai, X.; Yang, H. Vacancy-Free Prussian Blue Nanocrystals with High Capacity and Superior Cyclability for Aqueous Sodium-Ion Batteries. *ChemNanoMat* **2015**, *1*, 188-193.
- (247) Jiang, P.; Shao, H.; Chen, L.; Feng, J.; Liu, Z. Ion-Selective Copper Hexacyanoferrate with an Open-Framework Structure Enables High-Voltage Aqueous Mixed-Ion Batteries. *J. Mater. Chem. A* **2017**, *5*, 16740-16747.

- (248) Lee, J.-H.; Ali, G.; Kim, D. H.; Chung, K. Y. Metal-Organic Framework Cathodes Based on a Vanadium Hexacyanoferrate Prussian Blue Analogue for High-Performance Aqueous Rechargeable Batteries. *Adv. Energy Mater.* **2017**, *7*, 1601491.
- (249) Cai, D.; Yang, X.; Qu, B.; Wang, T. Comparison of the Electrochemical Performance of Iron Hexacyanoferrate with High and Low Quality as Cathode Materials for Aqueous Sodium-Ion Batteries. *Chem. Commun.* **2017**, *53*, 6780-6783.
- (250) Wu, X.; Xu, Y.; Jiang, H.; Wei, Z.; Hong, J. J.; Hernandez, A. S.; Du, F.; Ji, X. NH₄⁺ Topotactic Insertion in Berlin Green: An Exceptionally Long-Cycling Cathode in Aqueous Ammonium-Ion Batteries. *ACS Appl. Energy Mater.* **2018**, *1*, 3077-3083.
- (251) Zhang, L.; Chen, L.; Zhou, X.; Liu, Z. Towards High-Voltage Aqueous Metal-Ion Batteries Beyond 1.5 V: The Zinc/Zinc Hexacyanoferrate System. *Adv. Energy Mater.* **2015**, *5*, 1400930.
- (252) Wu, X.; Hong, J. J.; Shin, W.; Ma, L.; Liu, T.; Bi, X.; Yuan, Y.; Qi, Y.; Surta, T. W.; Huang, W. Diffusion-Free Grotthuss Topochemistry for High-Rate and Long-Life Proton Batteries. *Nat. Energy* **2019**, *4*, 123-130.
- (253) Wang, L.-P.; Wang, P.-F.; Wang, T.-S.; Yin, Y.-X.; Guo, Y.-G.; Wang, C.-R. Prussian Blue Nanocubes as Cathode Materials for Aqueous Na-Zn Hybrid Batteries. *J. Power Sources* **2017**, *355*, 18-22.
- (254) Lu, Y.; Wang, L.; Cheng, J.; Goodenough, J. B. Prussian Blue: A New Framework of Electrode Materials for Sodium Batteries. *Chem. Commun.* **2012**, *48*, 6544-6546.
- (255) You, Y.; Wu, X.-L.; Yin, Y.-X.; Guo, Y.-G. High-Quality Prussian Blue Crystals as Superior Cathode Materials for Room-Temperature Sodium-Ion Batteries. *Energy Environ. Sci.* **2014**, *7*, 1643-1647.
- (256) Pramudita, J. C.; Schmid, S.; Godfrey, T.; Whittle, T.; Alam, M.; Hanley, T.; Brand, H. E. A.; Sharma, N. Sodium Uptake in Cell Construction and Subsequent in Operando Electrode Behaviour of Prussian Blue Analogues, Fe[Fe(CN)₆]_{1-x}·yH₂O and FeCo(CN)₆. *Phys. Chem. Chem. Phys.* **2014**, *16*, 24178-24187.
- (257) Tang, S.; Li, L.; Ren, H.; Lv, Q.; Lv, R. Sodium-Ion Electrochemical Tuning of Prussian Blue Analog as an Efficient Oxygen Evolution Catalyst. *Mater. Today Chem.* **2019**, *12*, 71-77.
- (258) Yu, Z.-Y.; Duan, Y.; Liu, J.-D.; Chen, Y.; Liu, X.-K.; Liu, W.; Ma, T.; Li, Y.; Zheng, X.-S.; Yao, T.et al. Unconventional CN Vacancies Suppress Iron-Leaching in Prussian Blue Analogue Pre-Catalyst for Boosted Oxygen Evolution Catalysis. *Nat. Commun.* **2019**, *10*, 2799.
- (259) Jabeen, N.; Xia, Q.; Savilov, S. V.; Aldoshin, S. M.; Yu, Y.; Xia, H. Enhanced Pseudocapacitive Performance of α -MnO₂ by Cation Preinsertion. *ACS Appl. Mater. Interfaces* **2016**, *8*, 33732-33740.
- (260) Liu, Y.; Qiao, Y.; Zhang, W.; Xu, H.; Li, Z.; Shen, Y.; Yuan, L.; Hu, X.; Dai, X.; Huang, Y. High-Performance Aqueous Sodium-Ion Batteries with K_{0.27}MnO₂ Cathode and Their Sodium Storage Mechanism. *Nano Energy* **2014**, *5*, 97-104.
- (261) Liu, Y.; Qiao, Y.; Lou, X.; Zhang, X.; Zhang, W.; Huang, Y. Hollow K_{0.27}MnO₂ Nanospheres as Cathode for High-Performance Aqueous Sodium Ion Batteries. *ACS Appl. Mater. Interfaces* **2016**, *8*, 14564-14571.
- (262) Li, Z.; Young, D.; Xiang, K.; Carter, W. C.; Chiang, Y.-M. Towards High Power High Energy Aqueous Sodium-Ion Batteries: The NaTi₂(PO₄)₃/Na_{0.44}MnO₂ System. *Adv. Energy Mater.* **2013**, *3*, 290-294.
- (263) Zhang, B.; Liu, Y.; Wu, X.; Yang, Y.; Chang, Z.; Wen, Z.; Wu, Y. An Aqueous Rechargeable Battery Based on Zinc Anode and Na_{0.95}MnO₂. *Chem. Commun.* **2014**, *50*, 1209-1211.
- (264) Zuo, W.; Xie, C.; Xu, P.; Li, Y.; Liu, J. A Novel Phase-Transformation Activation Process toward Ni–Mn–O Nanoprism Arrays for 2.4 V Ultrahigh-Voltage Aqueous Supercapacitors. Adv. Mater. 2017, 29, 1703463.
- (265) Böhnstedt, W.; Radel, C.; Scholten, F. Antimony Poisoning in Lead-Acid Batteries. *J. Power Sources* **1987**, *19*, 307-314.

- (266) Döring, H.; Radwan, M.; Dietz, H.; Garche, J.; Wiesener, K. Untersuchungen Zur Inhibierung Der H₂-Entwicklung an Antimonkontaminierten Bleielektroden im Schwefelsauren Elektrolyten. *J. Power Sources* **1989**, *28*, 381-396.
- (267) Gust, S.; Hämeenoja, E.; Ahl, J.; Laitinen, T.; Savonen, A.; Sundholm, G. Effect of Organic Additives on the Lead/Acid Negative Plate. *J. Power Sources* **1990**, *30*, 185-192.
- (268) Dietz, H.; Radwan, M.; Döring, H.; Wiesener, K. On the Hydrogen Balance in Sealed Lead/Acid Batteries and Its Effect on Battery Performance. *J. Power Sources* **1993**, *42*, 89-101.
- (269) Zhao, Z.; Fan, X.; Ding, J.; Hu, W.; Zhong, C.; Lu, J. Challenges in Zinc Electrodes for Alkaline Zinc–Air Batteries: Obstacles to Commercialization. *ACS Energy Lett.* **2019**, *4*, 2259-2270.
- (270) Saakes, M.; J. Van Duin, P.; C.P. Ligtvoet, A.; Schmal, D. Investigations of the Negative Plate of Lead/Acid Cells 1. Selection of Additives. *J. Power Sources* **1994**, *47*, 129-147.
- (271) Malkhandi, S.; Yang, B.; Manohar, A. K.; Prakash, G. K. S.; Narayanan, S. R. Self-Assembled Monolayers of n-Alkanethiols Suppress Hydrogen Evolution and Increase the Efficiency of Rechargeable Iron Battery Electrodes. *J. Am. Chem. Soc.* **2013**, *135*, 347-353.
- (272) Hang, B. T.; Watanabe, T.; Egashira, M.; Watanabe, I.; Okada, S.; Yamaki, J.-i. The Effect of Additives on the Electrochemical Properties of Fe/C Composite for Fe/Air Battery Anode. *J. Power Sources* **2006**, *155*, 461-469.
- (273) Carta, R.; Dernini, S.; Polcaro, A. M.; Ricci, P. F.; Tola, G. The Influence of Sulphide Environment on Hydrogen Evolution at a Stainless Steel Cathode in Alkaline Solution. *J. Electroanal. Chem. Interfacial Electrochem.* **1988**, *257*, 257-268.
- (274) Zhu, M.; Wang, X.; Tang, H.; Wang, J.; Hao, Q.; Liu, L.; Li, Y.; Zhang, K.; Schmidt, O. G. Antifreezing Hydrogel with High Zinc Reversibility for Flexible and Durable Aqueous Batteries by Cooperative Hydrated Cations. *Adv. Funct. Mater.* **2020,** *30,* 1907218.
- (275) Solmaz, R. Investigation of the Inhibition Effect of 5-((E)-4-phenylbuta-1, 3-dienylideneamino)-1, 3, 4-thiadiazole-2-thiol Schiff Base on Mild Steel Corrosion in Hydrochloric Acid. *Corros. Sci.* **2010**, *52*, 3321-3330.
- (276) Zhu, Y.; Free, M. L.; Woollam, R.; Durnie, W. A Review of Surfactants as Corrosion Inhibitors and Associated Modeling. *Prog. Mater. Sci.* **2017**, *90*, 159-223.
- (277) Malik, M. A.; Hashim, M. A.; Nabi, F.; Al-Thabaiti, S. A.; Khan, Z. Anti-Corrosion Ability of Surfactants: A Review. *Int. J. Electrochem. Sci* **2011**, *6*, 1927-1948.
- (278) Bhattacharya, A.; Basumallick, I. N. Effect of Mixed Additives on Lead–Acid Battery Electrolyte. *J. Power Sources* **2003**, *113*, 382-387.
- (279) Vinod, M. P.; Vijayamohanan, K.; Joshi, S. N. Effect of Silicate and Phosphate Additives on the Kinetics of the Oxygen Evolution Reaction in Valve-Regulated Lead/Acid Batteries. *J. Power Sources* **1998**, *70*, 103-105.
- (280) Shangguan, E.; Wang, J.; Li, J.; Dan, G.; Chang, Z.; Yuan, X.-Z.; Wang, H. Enhancement of the High-Temperature Performance of Advanced Nickel–Metal Hydride Batteries with NaOH Electrolyte Containing NaBO₂. *Int. J. Hydrog. Energy* **2013**, *38*, 10616-10624.
- (281) Miyazaki, K.; Shimada, T.; Ito, S.; Yokoyama, Y.; Fukutsuka, T.; Abe, T. Enhanced Resistance to Oxidative Decomposition of Aqueous Electrolytes for Aqueous Lithium-Ion Batteries. *Chem. Commun.* **2016**, *52*, 4979-4982.
- (282) Shang, Y.; Chen, N.; Li, Y.; Chen, S.; Lai, J.; Huang, Y.; Qu, W.; Wu, F.; Chen, R. An "Ether-In-Water" Electrolyte Boosts Stable Interfacial Chemistry for Aqueous Lithium-Ion Batteries. *Adv. Mater.* **2020**, *32*, 2004017.
- (283) Ko, S.; Yamada, Y.; Yamada, A. Formation of a Solid Electrolyte Interphase in Hydrate-Melt Electrolytes. *ACS Appl. Mater. Interfaces* **2019**, *11*, 45554-45560.

- (284) Suo, L.; Borodin, O.; Wang, Y.; Rong, X.; Sun, W.; Fan, X.; Xu, S.; Schroeder, M. A.; Cresce, A. V.; Wang, F. "Water-in-Salt" Electrolyte Makes Aqueous Sodium-Ion Battery Safe, Green, and Long-Lasting. *Adv. Energy Mater.* **2017**, *7*, 1701189.
- (285) Lee, M. H.; Kim, S. J.; Chang, D.; Kim, J.; Moon, S.; Oh, K.; Park, K.-Y.; Seong, W. M.; Park, H.; Kwon, G. Toward a Low-Cost High-Voltage Sodium Aqueous Rechargeable Battery. *Mater. Today* **2019**, *29*, 26-36.
- (286) Jiang, L.; Lu, Y.; Zhao, C.; Liu, L.; Zhang, J.; Zhang, Q.; Shen, X.; Zhao, J.; Yu, X.; Li, H. Building Aqueous K-Ion Batteries for Energy Storage. *Nat. Energy* **2019**, *4*, 495-503.
- (287) Vatamanu, J.; Borodin, O. Ramifications of Water-in-Salt Interfacial Structure at Charged Electrodes for Electrolyte Electrochemical Stability. *J. Phys. Chem. Lett.* **2017**, *8*, 4362-4367.
- (288) Hou, Y.; Wang, X.; Zhu, Y.; Hu, C.; Chang, Z.; Wu, Y.; Holze, R. Macroporous LiFePO₄ as a Cathode for an Aqueous Rechargeable Lithium Battery of High Energy Density. *J. Mater. Chem. A* **2013**, *1*, 14713-14718.
- (289) Chang, Z.; Li, C.; Wang, Y.; Chen, B.; Fu, L.; Zhu, Y.; Zhang, L.; Wu, Y.; Huang, W. A Lithium Ion Battery Using an Aqueous Electrolyte Solution. *Sci. Rep.* **2016**, *6*, 28421.
- (290) Chang, Z.; Yang, Y.; Wang, X.; Li, M.; Fu, Z.; Wu, Y.; Holze, R. Hybrid System for Rechargeable Magnesium Battery with High Energy Density. *Sci. Rep.* **2015**, *5*, 11931.
- (291) Son, S.-B.; Gao, T.; Harvey, S. P.; Steirer, K. X.; Stokes, A.; Norman, A.; Wang, C.; Cresce, A.; Xu, K.; Ban, C. An Artificial Interphase Enables Reversible Magnesium Chemistry in Carbonate Electrolytes. *Nat. Chem.* **2018**, *10*, 532-539.
- (292) Zhao, Q.; Zachman, M. J.; Al Sadat, W. I.; Zheng, J.; Kourkoutis, L. F.; Archer, L. Solid Electrolyte Interphases for High-Energy Aqueous Aluminum Electrochemical Cells. *Sci. Adv.* **2018**, *4*, eaau8131.
- (293) Hao, J.; Li, X.; Zhang, S.; Yang, F.; Zeng, X.; Zhang, S.; Bo, G.; Wang, C.; Guo, Z. Designing Dendrite-Free Zinc Anodes for Advanced Aqueous Zinc Batteries. *Adv. Funct. Mater.* **2020**, *30*, 2001263.
- (294) Stojković, I. B.; Cvjetićanin, N. D.; Mentus, S. V. The Improvement of the Li-Ion Insertion Behaviour of Li_{1.05}Cr_{0.10}Mn_{1.85}O₄ in an Aqueous Medium upon Addition of Vinylene Carbonate. *Electrochem. Commun.* **2010**, *12*, 371-373.
- (295) Wang, F.; Lin, Y.; Suo, L.; Fan, X.; Gao, T.; Yang, C.; Han, F.; Qi, Y.; Xu, K.; Wang, C. Stabilizing High Voltage LiCoO₂ Cathode in Aqueous Electrolyte with Interphase-Forming Additive. *Energy Environ. Sci.* **2016**, *9*, 3666-3673.
- (296) Padhy, S. K.; Patnaik, P.; Tripathy, B. C.; Ghosh, M. K.; Bhattacharya, I. N. Electrodeposition of Manganese Metal from Sulphate Solutions in the Presence of Sodium Octyl sulphate. *Hydrometallurgy* **2016**, *165*, 73-80.
- (297) Mistry, H.; Varela, A. S.; Bonifacio, C. S.; Zegkinoglou, I.; Sinev, I.; Choi, Y.-W.; Kisslinger, K.; Stach, E. A.; Yang, J. C.; Strasser, P.et al. Highly Selective Plasma-Activated Copper Catalysts for Carbon Dioxide Reduction to Ethylene. *Nat. Commun.* **2016**, *7*, 12123.
- (298) Silva, L. M. D.; Faria, L. A. D.; Boodts, J. F. C. Green Processes for Environmental Application. Electrochemical Ozone Production. *Pure Appl. Chem.* **2001**, *73*, 1871.
- (299) Shi, X.; Siahrostami, S.; Li, G.-L.; Zhang, Y.; Chakthranont, P.; Studt, F.; Jaramillo, T. F.; Zheng, X.; Nørskov, J. K. Understanding Activity Trends in Electrochemical Water Oxidation to Form Hydrogen Peroxide. *Nat. Commun.* **2017**, *8*, 1-6.
- (300) Zhao, G.; Zhang, Y.; lei, Y.; Lv, B.; Gao, J.; Zhang, Y.; Li, D. Fabrication and Electrochemical Treatment Application of A Novel Lead Dioxide Anode with Superhydrophobic Surfaces, High Oxygen Evolution Potential, and Oxidation Capability. *Environ. Sci. Technol.* **2010**, *44*, 1754-1759.

- (301) Ramanauskas, R.; Quintana, P.; Maldonado, L.; Pomés, R.; Pech-Canul, M. Corrosion Resistance and Microstructure of Electrodeposited Zn and Zn Alloy Coatings. *Surf. Coat. Technol.* **1997,** *92*, 16-21.
- (302) Ramanauskas, R. Structural Factor in Zn Alloy Electrodeposit Corrosion. *Appl. Surf. Sci.* **1999**, *153*, 53-64.
- (303) Abou-Krisha, M.; Rageh, H.; Matter, E. Electrochemical Studies on the Electrodeposited Zn–Ni–Co Ternary Alloy in Different Media. *Surf. Coat. Technol.* **2008**, *202*, 3739-3746.
- (304) Wei, H.; Ding, D.; Wei, S.; Guo, Z. Anticorrosive Conductive Polyurethane Multiwalled Carbon Nanotube Nanocomposites. *J. Mater. Chem. A* **2013**, *1*, 10805-10813.
- (305) Vathsala, K.; Venkatesha, T. V. Zn–ZrO₂ Nanocomposite Coatings: Electrodeposition and Evaluation of Corrosion Resistance. *Appl. Surf. Sci.* **2011**, *257*, 8929-8936.
- (306) Sobhi, M. Gatifloxacin as Corrosion Inhibitor for Carbon Steel in Hydrochloric Acid Solutions. *Prot. Met. Phys. Chem. Surf.* **2014**, *50*, 825-832.
- (307) Kosari, A.; Moayed, M. H.; Davoodi, A.; Parvizi, R.; Momeni, M.; Eshghi, H.; Moradi, H. Electrochemical and Quantum Chemical Assessment of Two Organic Compounds from Pyridine Derivatives as Corrosion Inhibitors for Mild Steel in HCl Solution under Stagnant Condition and Hydrodynamic Flow. *Corros. Sci.* **2014**, *78*, 138-150.
- (308) Abdallah, M.; Sobhi, M.; Altass, H. Corrosion Inhibition of Aluminum in Hydrochloric Acid by Pyrazinamide Derivatives. *J. Mol. Liq.* **2016**, *223*, 1143-1150.
- (309) Raja, P. B.; Ismail, M.; Ghoreishiamiri, S.; Mirza, J.; Ismail, M. C.; Kakooei, S.; Rahim, A. A. Reviews on Corrosion Inhibitors: A Short View. *Chem. Eng. Commun.* **2016**, *203*, 1145-1156.
- (310) Mohamed, A. M.; Abdullah, A. M.; Younan, N. A. Corrosion Behavior of Superhydrophobic Surfaces: A Review. *Arab. J. Chem.* **2015**, *8*, 749-765.
- (311) Liu, L.; Li, Y.; Wang, F. Electrochemical Corrosion Behavior of Nanocrystalline Materials—A Review. *J. Mater. Sci. Technol.* **2010**, *26*, 1-14.
- (312) Chao, D.; Zhou, W.; Ye, C.; Zhang, Q.; Chen, Y.; Gu, L.; Davey, K.; Qiao, S.-Z. An Electrolytic Zn–MnO₂ Battery for High-Voltage and Scalable Energy Storage. *Angew. Chem. Int. Ed.* **2019**, *58*, 7823-7828.
- (313) Wang, H.; Liang, Y.; Gong, M.; Li, Y.; Chang, W.; Mefford, T.; Zhou, J.; Wang, J.; Regier, T.; Wei, F.et al. An Ultrafast Nickel–Iron Battery from Strongly Coupled Inorganic Nanoparticle/Nanocarbon Hybrid Materials. *Nat. Commun.* **2012**, *3*, 917.
- (314) Verma, M. P. In *Twenty-Eighth Workshop on Geothermal Reservoir Engineering* Stanford University, Stanford, California, 2003.
- (315) Ganesan, S.; Prabhu, G.; Popov, B. N. Electrodeposition and Characterization of Zn-Mn Coatings for Corrosion Protection. *Surf. Coat. Technol.* **2014**, *238*, 143-151.
- (316) Hoang, T. K.; Sun, K. E. K.; Chen, P. Corrosion Chemistry and Protection of Zinc & Zinc Alloys by Polymer-Containing Materials for Potential Use in Rechargeable Aqueous Batteries. *RSC Adv.* **2015**, *5*, 41677-41691.
- (317) Divakar, R.; Seshadri, S. G.; Srinivasan, M. Electrochemical Techniques for Corrosion Rate Determination in Ceramics. *J. Am. Ceram. Soc.* **1989**, *72*, 780-784.
- (318) Ismail, M.; Ohtsu, M. Corrosion Rate of Ordinary and High-Performance Concrete Subjected to Chloride Attack by AC Impedance Spectroscopy. *Constr. Build. Mater.* **2006**, *20*, 458-469.
- (319) Stern, M.; Geary, A. L. Electrochemical Polarization: I. A Theoretical Analysis of the Shape of Polarization Curves. *J. Electrochem. Soc.* **1957**, *104*, 56.
- (320) Gavrila, M.; Millet, J.; Mazille, H.; Marchandise, D.; Cuntz, J. Corrosion Behaviour of Zinc–Nickel Coatings, Electrodeposited on Steel. *Surf. Coat. Technol.* **2000**, *123*, 164-172.

- (321) Kou, T.; Chen, M.; Wu, F.; Smart, T. J.; Wang, S.; Wu, Y.; Zhang, Y.; Li, S.; Lall, S.; Zhang, Z.et al. Carbon Doping Switching on the Hydrogen Adsorption Activity of NiO for Hydrogen Evolution Reaction. *Nat. Commun.* **2020**, *11*, 590.
- (322) Liang, Q.; Jin, H.; Wang, Z.; Xiong, Y.; Yuan, S.; Zeng, X.; He, D.; Mu, S. Metal-Organic Frameworks Derived Reverse-Encapsulation Co-NC@Mo₂C Complex for Efficient Overall Water Splitting.

 Nano Energy 2019, 57, 746-752.
- (323) Sun, Y.; Yang, T.; Ji, H.; Zhou, J.; Wang, Z.; Qian, T.; Yan, C. Boosting the Optimization of Lithium Metal Batteries by Molecular Dynamics Simulations: A Perspective. *Adv. Energy Mater.* **2020,** *10*, 2002373.
- (324) He, Q.; Yu, B.; Li, Z.; Zhao, Y. Density Functional Theory for Battery Materials. *Energy Environ. Mater.* **2019**, *2*, 264-279.